

Nonlinear amplification by active sensory hair bundles

DISSERTATION

zur Erlangung des akademischen Grades

Doctor rerum naturalium
(Dr. rer. nat.)

vorgelegt

der Fakultät Mathematik und
Naturwissenschaften
der Technischen Universität Dresden

von

Kai Dierkes

geboren am 21.2.1977 in Essen

Eingereicht am 10. Juni 2010

Eingereicht am 10. Juni 2010
Verteidigt am 12. August 2010

1. Gutachter: Prof. Dr. Frank Jülicher
2. Gutachter: Prof. Dr. Alexander Neiman

Abstract

The human sense of hearing is characterized by its exquisite sensitivity, sharp frequency selectivity, and wide dynamic range. These features depend on an active process that in the inner ear boosts vibrations evoked by auditory stimuli. Spontaneous otoacoustic emissions constitute a demonstrative manifestation of this physiologically vulnerable mechanism. In the cochlea, sensory hair bundles transduce sound-induced vibrations into neural signals. Hair bundles can power mechanical movements of their tip, oscillate spontaneously, and operate as tuned nonlinear amplifiers of weak periodic stimuli. Active hair-bundle motility constitutes a promising candidate with respect to the biophysical implementation of the active process underlying human hearing.

The responsiveness of isolated hair bundles, however, is seriously hampered by intrinsic fluctuations. In this thesis, we present theoretical and experimental results concerning the noise-imposed limitations of nonlinear amplification by active sensory hair bundles. We analyze the effect of noise within the framework of a stochastic description of hair-bundle dynamics and relate our findings to generic aspects of the stochastic dynamics of oscillatory systems.

Hair bundles *in vivo* are often elastically coupled by overlying gelatinous membranes. In addition to theoretical results concerning the dynamics of elastically coupled hair bundles, we report on an experimental study. We have interfaced dynamic force clamp performed on a hair bundle from the sacculus of the bullfrog with real-time stochastic simulations of hair-bundle dynamics. By means of this setup, we could couple a hair bundle to two virtual neighbors, called cyber clones. Our theoretical and experimental work shows that elastic coupling leads to an effective noise reduction. Coupled hair bundles exhibit an increased coherence of spontaneous oscillations and an enhanced amplification gain. We therefore argue that elastic coupling by overlying membranes constitutes a morphological specialization for reducing the detrimental effect of intrinsic fluctuations.

Acknowledgments

Above all, I would like to thank Dr. Benjamin Lindner for the patient and intense supervision of my research. I greatly appreciate all the time and effort that he spent in helping me with my project.

Furthermore, I would like to thank Prof. Dr. Frank Jülicher for giving me the opportunity to join his group at the MPIPKS and for guiding my work during the last years.

Some of the results presented in this thesis were obtained in close collaboration with our colleagues at the Institut Curie in Paris. I would like to thank Dr. Pascal Martin for many stimulating discussions and for giving me the opportunity to spend several weeks of my PhD in his laboratory. A special thanks also goes to Jérémie Barral for spending numerous hours with me at the microscope and in front of the computer in order to perform the experiments discussed in chapter 5.

During my research, I have greatly profited from discussions with Johannes Baumgart, Dr. Nils Becker, Diana Claußnitzer, Christian Gnodtke, and Dr. Dhaibhid O'Maoileidigh. I thank them for their interest and enthusiasm.

Also, I would like to thank Dr. Thomas Bittig, Florian Fruth, and Dr. Abigail Klopper for proofreading and commenting on this manuscript.

Many more people in Dresden and Berlin had their share in making these last years what they have been, scientifically as well as non-scientifically. Not to run the risk of presenting an incomplete list: Thanks to all of you!

Last but not least, I would like to thank my parents and my sister for their loving support throughout all these past years.

Contents

1	Introduction	1
1.1	Hearing in vertebrates	2
1.2	From resonance theory to the cochlear amplifier	5
1.3	Amplification by critical oscillators	13
1.4	Active hair-bundle motility	16
1.4.1	Hair-bundle morphology	16
1.4.2	Hair-bundle oscillations in the sacculus of the bullfrog	18
1.4.3	Physical description of hair-bundle dynamics	21
1.4.4	Coupling of hair bundles <i>in vivo</i>	31
1.5	Coupled oscillators and synchronization	32
1.6	Outline of this thesis	33
2	Noise-imposed limits of hair-bundle performance	35
2.1	Quality of spontaneous oscillations	35
2.2	Amplification gain	40
2.3	Local exponents of nonlinear compression	45
2.4	Summary	46
3	Limit-cycle dynamics in the presence of fluctuations	49
3.1	Dynamics close to a Hopf bifurcation	49
3.2	Phase diffusion and partial entrainment	52
3.3	Amplitude growth vs. phase locking	58
3.4	Local exponents of nonlinear compression	61
3.5	Summary	66
4	Theory of coupled hair bundles	67
4.1	Physical description of coupled hair bundles	67
4.2	Spontaneous noisy oscillations and synchronization	71
4.3	Nonlinear amplification	73
4.4	Transient responses	75
4.5	Heterogeneities	79
4.6	A mean-field argument	81
4.7	Summary	89

5	The hair bundle and its cyber clones - A hybrid experiment	91
5.1	Dynamic force clamp	91
5.2	Cyber clones	95
5.3	Synchronization and increased phase coherence	97
5.4	Enhancement of mechanical amplification	99
5.5	Effects of gentamicin	101
5.6	Parameter mismatches	102
5.7	Summary	104
6	Conclusions and outlook	107
A	Discretization of cyber-clone dynamics	113
	Bibliography	116

Chapter 1

Introduction

Hearing has an impact on a multitude of human activities. Auditory cues, such as the sounding of a cyclist's bell, help us to generate an internal representation of the surrounding environment. In order for another individual's utterances to be intelligible as speech, our ear must be capable of resolving their frequency content, as well as their dynamic and temporal structure. The intellectual and emotional pleasures induced by a piece of music are likewise dependent on our ability to appropriately analyze auditory stimuli.

The human ear performs the task of hearing with remarkable acuity. With auditory frequencies stretching over a range from about 20 Hz up to 20 kHz, an untrained individual can readily discern two tones that differ in frequency by less than 0.5%. As for temporal resolution, humans can detect gaps on the order of only a few milliseconds separating two pure tones. At the same time, the ear operates over a vast dynamic range, covering about six orders of magnitude in sound pressure level (SPL). Being able to perceive the faintest sounds, such as the rustling of leaves in a tree at about 0 dB SPL, the human ear also copes with the roaring of a starting airplane's engine at about 120 dB SPL.

The last century has seen remarkable progress with regard to our understanding of the biophysical principles underlying hearing. Some fundamental issues, however, are left unresolved and continue to challenge researchers from various fields.

Within the inner ear, the transduction of sound-induced mechanical vibrations into neural signals is achieved by cells which are equipped with a specialized sensory organelle, the so-called hair bundle. The hair bundle is a tuft of interlinked stereocilia emanating from the hair cell's apical surface. Hair bundles constitute active elements, possessing the ability to oscillate spontaneously and to operate as nonlinear amplifiers of appropriate mechanical stimuli. Active hair-bundle motility has been proposed as a key element in understanding the origin of the inner ear's exquisite sensitivity, broad dynamic range and acute frequency resolution.

In this thesis, we present both theoretical and experimental results regarding the dynamics and signal detection properties of single and coupled hair bundles. In particular, we analyze the effects of intrinsic fluctuations on hair-bundle operation

and show that elastically coupled hair bundles are expected to outperform isolated ones due to a noise-reduction effect. We relate our findings to results dealing with generic aspects concerning the dynamics of noisy oscillators.

1.1 Hearing in vertebrates

In the inner ear of vertebrates, several sensory organs are dedicated to the transduction of mechanical stimuli into neural signals. In mammals, the utricle and sacculus are sensors of linear accelerations of the head. Together with the semicircular canals, which are detectors of rotational head movements, they constitute the vestibular system. The auditory system in mammals comprises a single inner ear organ, the cochlea. In all the other vertebrate classes, structurally similar inner ear organs have evolved for the detection of sound and head accelerations [68, 105, 88].

In humans, the pinna performs the function of a hearing horn (see fig. 1.1A). Incoming sound stimuli are funneled toward the tympanic membrane via the external auditory meatus. The outer ear constitutes a complex resonant cavity with a sound pressure gain of about 20dB at 2.5 kHz, measured at the ear drum [146].

The air-filled middle ear transmits vibrations of the tympanic membrane to the fluid-filled cochlea via three miniscule bones, the so-called ossicles. More specifically, the chain of ossicles comprises the malleus, the incus, and the stapes. The latter is embedded into the oval window, a membranous opening in the cochlea's boney wall. In order to minimize the reflection of acoustic energy at the interface between the low-impedance tympanic membrane and the high-impedance oval window, the middle-ear has evolved to perform an effective impedance matching [125].

The cochlea is a coiled cavity in the temporal bone, forming part of the inner ear. It is divided longitudinally, i.e. from base to apex, into three scalae (see fig. 1.1B and fig. 1.2A). The perilymph-filled scalae tympani and vestibuli are joined at the apical end of the cochlea by an opening known as the helicotrema. The scala media is filled with endolymph. It is separated from the scala vestibuli by Reissner's membrane and from the scala tympani by the basilar membrane, the latter being an elastic membrane with a length of about 35mm in humans [164]. The oval window opens onto the scala vestibuli. A movement of the stapes displaces cochlear fluids towards a second membranous window, the round window opening onto the scala tympani (see fig. 1.2B).

Oscillatory movements of the stapes induce pressure gradients across the three scalae, causing a wave-like displacement of the basilar membrane to travel from base to apex [170, 138]. After a gradual build up, the traveling waves' amplitude peaks at a location determined by its frequency, and rapidly decays thereafter. The cochlea therefore exhibits a tonotopic organization. For each location on the basilar membrane there is a characteristic frequency which elicits a maximal response. This characteristic frequency gradually varies along the cochlea, with high frequencies close to the base and low frequencies close to the apex [57].

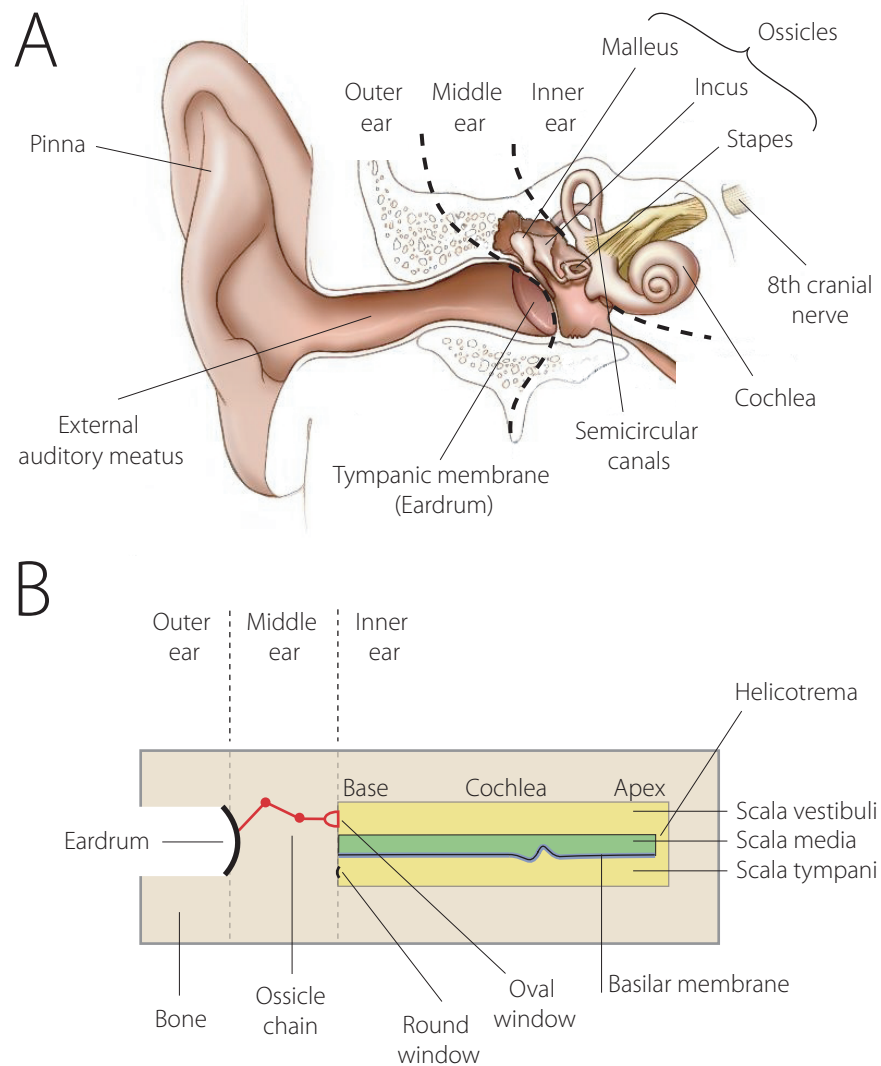


Figure 1.1: Morphology of the human ear. (A) The human ear is subdivided into the outer, middle and inner ear. Sound, i.e. waves of oscillating air pressure, are concentrated by the pinna and the external auditory meatus/ear canal onto the tympanic membrane/eardrum. Vibrations of the eardrum effect an oscillatory movement of the ossicles (malleus, incus, stapes). The stapes is attached like a piston to the oval window of the cochlea. The latter, a bone-enclosed spiral, is part of the osseous labyrinth, which comprises the semicircular canals and also the remaining organs of the vestibular system. Sensory information of the vestibular and auditory system is sent to the brain via the 8th cranial nerve. Adapted from ref. [1]. In (B), we present a sketch of the uncoiled cochlea. Three scalae can be distinguished, with the scala tympani and scala vestibuli connected at the apical end of the cochlea by the helicotrema. The oval window is located at the basal end of the scala vestibuli. Since cochlear fluids are effectively incompressible, movements of the stapes are paralleled by movements of a membrane overstretching the round window. Oscillatory movements of the stapes cause a wave of basilar membrane vibrations to travel from the base of the cochlea to its apex. The amplitude of the traveling wave peaks at a location determined by its frequency, with high frequencies being located near the base and low frequencies near the apex of the cochlea.

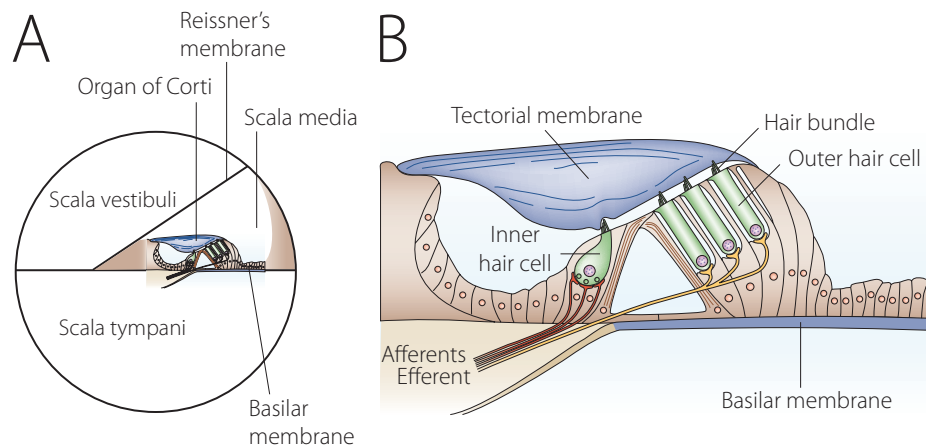


Figure 1.2: The organ of Corti. In (A) a sketch of a slice of the cochlea is shown, with the cut being made orthogonal to the cochlea's longitudinal axis. Note the three scalae, with Reissner's membrane and the basilar membrane separating the scala media from the scala vestibuli and the scala tympani, respectively. Located on the basilar membrane within the scala media is the organ of Corti. The latter is a complex morphological structure sketched in (B). Two types of sensory hair cells, namely the inner and outer hair cells can be distinguished. While the hair bundles of inner hair cells project into the surrounding endolymph, the tips of the outer hair-cell bundles are embedded in the overlying tectorial membrane. Most afferent nerve fibers end on inner hair cells. The predominant innervation of outer hair cells is by efferent nerve fibers. Adapted from ref. [43].

The basilar membrane supports the organ of Corti, a complex morphological structure consisting of sensory and supporting cells (see fig. 1.2B). Two types of sensory cells have evolved: the inner and outer hair cells. A single row of inner hair cells lines the cochlea from base to apex. There are three to five parallel rows of outer hair cells, with the number of rows increasing with distance from the base of the cochlea [125]. In total, the human cochlea contains approximately 15,000 hair cells [164]. Each hair cell is endowed with a specialized mechanosensitive organelle, the hair bundle ([110], see also fig. 1.7B). By means of mechanosensitive ion-channels, the hair bundle transduces tip-deflections into ionic currents entering the soma of the hair cell (see also section 1.4). The ensuing modulation of the membrane potential ultimately triggers a neural response via the release of neurotransmitters at the basal side of the cell. Inner hair-cell bundles project into the surrounding endolymph. In contrast, the tips of outer hair-cell bundles are embedded into the overlying tectorial membrane, an acellular gelatinous matrix composed of collagen fibrils and non-collageneous proteins [58, 135, 50].

Sound-induced vibrations of the basilar membrane prompt a shearing movement of the reticular lamina, i.e. of the outer hair cell's apical surface, with respect to the tectorial membrane. In this way, a deflection of the outer hair-cell bundles is elicited. At the same time, hydrodynamic flows within the subtectorial cleft, i.e. the endolymph-filled gap formed by the tectorial membrane and the reticular lamina, lead to a deflection of the inner hair-cell bundles.

Sensory information about auditory stimuli is relayed to the brain predominantly by the inner hair cells. The mammalian cochlea is innervated by approximately 30,000 afferent sensory neurons, about 90-95% of which connect directly with inner hair cells [151, 14]. Thus while being by far more numerous, outer hair cells receive only about 5–10% of the cochlea's afferent innervation. Of the approximately 1,800 efferent neurons, 800 connect to the region of outer hair cells, the remaining 1,000 fibers innervate the region of inner hair cells [173].

1.2 From resonance theory to the cochlear amplifier

One of the earliest modern theories for the human sense of hearing was put forward in 1863 by Hermann von Helmholtz [172]. Two important developments preceded his proposal. In mathematics, the first half of the 19th century had seen the advent of Fourier analysis [46]. Within this theoretical framework, temporal signals, such as intricate air pressure variations corresponding to complex sounds, could for the first time be conceptualized as being made up of simple sinusoids, i.e. pure tones. On the other hand, due to refined staining techniques, Alfonso Corti in 1851 had been able to give a description of the inner ear, which was unprecedented in terms of its morphological detail [24]. Most importantly, he had mapped out the organ of Corti and noted its serial arrangement along the cochlea. In the spirit of these two advancements, Helmholtz developed his resonance theory of hearing. He envisioned the individual rods of the arches of Corti passively resonating in response to auditory stimulation, subject to a gradual change of resonant frequency along the basilar membrane. According to this idea, a sound stimulus would elicit a complex pattern of resonant vibrations, which could be detected by neural innervation. In short, Helmholtz suggested that the human cochlea operated in a similar fashion to a linear Fourier analyzer. There was, however, a problem with this view. As cochlear fluids dampen passive resonances and significantly broaden their bandwidth, the behaviorally observed sharp frequency resolution of the human ear was not readily explained by Helmholtz's theory.

An important step toward our current understanding of cochlear mechanics was taken in the first half of the 20th century by Georg von Békésy [170]. He observed that the basilar membrane exhibits a morphological gradient along its length. While it is narrow and stiff at the base, it widens toward the apex and becomes more compliant. Constructing artificial cochlear ducts to scale from water tanks and elastic sheets with appropriate stiffness gradients, Békésy found that mechanical models of this kind could perform a rudimentary form of frequency analysis [167]. High frequency tones induced a broad peak of vibration close to the base of the artificial basilar membrane and low frequencies close to its apex. Békésy confirmed and refined these findings by means of measurements performed on actual cochleae, dissected from cadavers of various mammalian species and birds [168, 169]. Due to the limited sensitivity of his observation technique, he was restricted to intense

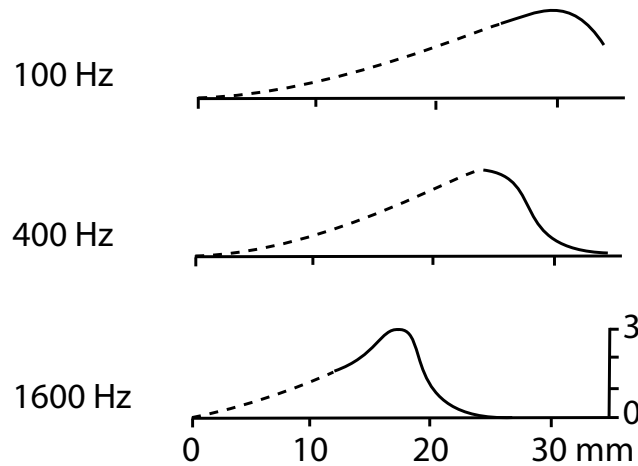


Figure 1.3: The envelope of the traveling wave as observed by Békésy. The maximal amplitude of the traveling wave, i.e. its envelope, is shown as a function of distance from the stapes for three different stimulation frequencies. Note that the peak of the envelope shifts from apex to base upon increase of the stimulus frequency, indicative of the cochlea's tonotopic organization. Reproduced from ref. [171].

stimulation at sound pressure levels of about 120-140 dB, which exceed the physiologically relevant range. Békésy showed that stimulation of the oval window with a pure tone elicits a wave of basilar membrane displacement traveling from base to apex. The maximal vibration amplitude as a function of distance along the basilar membrane determines the wave's envelope (see fig. 1.3). When measuring this amplitude, Békésy observed the following: on its path, the amplitude of the traveling wave gradually built up and peaked at a frequency-dependent location. Beyond this peak, the wave decayed rapidly. A few years later, Jozef Zwislocki presented a one-dimensional mathematical description of cochlear mechanics which closely matched Békésy's findings [180].

The work of Békésy and Zwislocki established the now classical paradigm of the traveling wave. Two problems with this view need mentioning. Békésy's data indicated that the response of the basilar membrane was only poorly frequency selective. This was in stark contrast with the observed frequency resolution of human hearing. Furthermore, Békésy had found a linear dependence of the basilar membrane's response amplitude on sound pressure level. Linear extrapolation to the full range of physiologically relevant sound intensities suggested that close to the threshold of hearing sound stimuli would elicit a response with an amplitude on the order of $1/500$ of the diameter of a hydrogen atom. A truly startling prediction!

By the end of the first half of the last century, however, the predominant view was that the main questions concerning cochlear mechanics by and large were resolved. Support for this view also came in the 1940s and 1950s, when the first studies on neural responses were performed on cochlear afferents [48, 160]. In agreement with

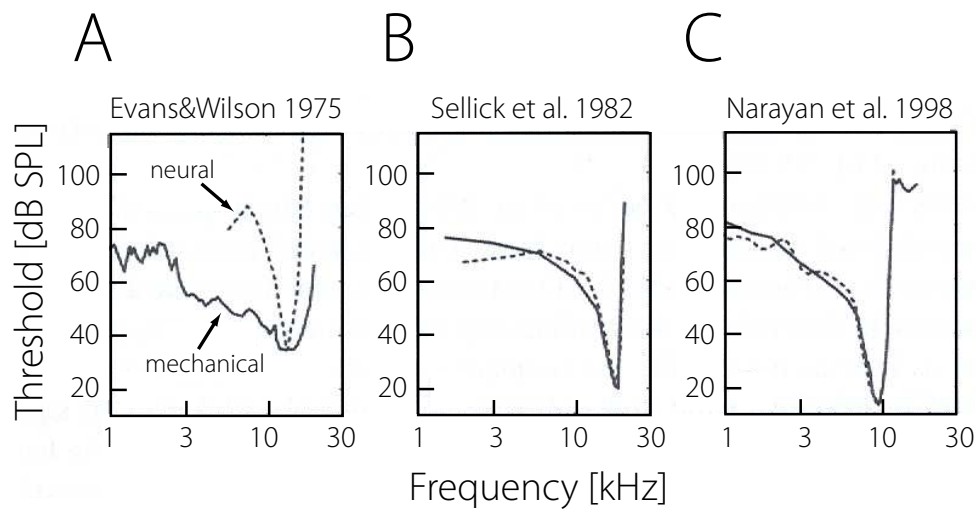


Figure 1.4: Mechanical and neural tuning curves. In order to probe the sharpness of mechanical frequency selectivity of a specific place along the basilar membrane, as well as the tuning of nerve fibers emanating from this very place, threshold tuning curves can be recorded as a function of frequency. To obtain a mechanical tuning curve, for each frequency, while monitoring basilar membrane vibrations, the minimal sound intensity needed to elicit a response exceeding a fixed threshold amplitude is recorded. More precisely, the threshold is set in terms of the vibration’s peak velocity (here $1\mu\text{m/s}$). For a given frequency, this peak velocity is proportional to the vibration amplitude. In the case of neural tuning curves, a similar threshold criterion is formulated in terms of the neuron’s spiking rate (for more details see e.g. ref. [125]). As shown in (A), by the mid-1970s the available data seemed to reveal a profound discrepancy between mechanical (solid lines) and neural (dashed lines) tuning curves, possibly attributable to the operation of a “second filter” [30]. Refined measurements as displayed in (B) and (C), however, showed that earlier measurements of basilar membrane responses were compromised, most likely due to the physiological vulnerability of the cochlea and the large sound intensities used. Adapted from ref. [22].

Békésy’s measurements, the data indicated that single nerve fibers, innervating a specific place along the basilar membrane, responded to auditory stimulation in a frequency selective manner. While the observed tuning was poor, it was consistent with the broad tuning curves observed by Békésy and predicted theoretically by Zwislocki.

The discussion was revived in the late 1960s and early 1970s, when the use of refined techniques for obtaining single nerve recordings seemed to reveal a discrepancy between neural and mechanical tuning curves. While the mechanical response of the basilar membrane still appeared only broadly tuned, nerve fibers emanating from the cochlea exhibited a profoundly sharper frequency selectivity (see fig. 1.4A). In order to explain this state of affairs, Ted Evans in 1972 proposed the existence of a “second filter” which prior to neural encoding would sharpen the poorly tuned mechanical output of the basilar membrane. Several theories as to the implementation of this additional filter were brought forward in subsequent years (for a review see ref. [30]).

A resolution of the issue, however, was reached in a different way. Making use of the Mössbauer effect and later of heterodyne laser interferometry, new measurement techniques introduced in the late 1960s, allowed for improved measurements of cochlear mechanics. As a consequence of the enhanced sensitivity of the experimental set-ups, the response of the basilar membrane could be probed for sound intensities much lower than those used by Békésy. At the same time, it became increasingly apparent that cochlear performance is strongly influenced by the integrity of the cochlear preparation, meaning that it is physiologically vulnerable. Ultimately, the response of the basilar membrane was shown to be just as sharply tuned as the response of single cochlear nerve fibers (see fig. 1.4B and C, [145, 119]). In particular it was found to be much more frequency selective than Békésy's experiments had suggested.

Around the same time, another highly influential finding was made. As mentioned earlier, Békésy regarded the cochlea as a linear system. In 1971 William Rhode reported on measurements which in contrast revealed clear signs of nonlinearity. Measuring at a fixed location of the squirrel monkey's cochlea, he observed that for stimulation at the characteristic frequency, the amplitude of basilar membrane vibrations increased sublinearly with sound pressure level. For pure tones with differing frequencies, however, he observed linear behavior. In other words, Rhode's data pointed toward the existence of a frequency dependent nonlinearity shaping cochlear mechanics. While this finding was considered of immense importance, it nevertheless took almost 10 years before Rhode's results could be reproduced by independent groups [145, 139] (for a more recent data set see fig. 1.5). These and later studies established that the basilar membrane responds most sensitive to weak stimuli at the characteristic frequency. Here, sensitivity is defined as the ratio of the input sound pressure level to the output vibration amplitude (or equivalently its peak velocity). For intermediate stimulus pressures, sensitivity decreases in a nonlinear fashion. The efficiency of the nonlinearity in boosting low-level responses in comparison to high-level responses can be quantified by means of the gain, which is defined as the ratio of sensitivities to weak and strong stimuli. A linear system, which is characterized by a constant sensitivity, has a gain of unity. The cochlea, in contrast, was shown to exhibit gains of 100-1000, i.e. of 40-60 dB [138]. Later studies also attested the fully reversible physiological vulnerability of the observed nonlinearity [140].

The proof of the existence of a frequency dependent nonlinearity had repercussions on several open questions. For one, since the degree of mechanical tuning of the basilar membrane depends on the sound pressure level of the applied stimuli (see fig. 1.5B), the apparent discrepancy between neural and mechanical tuning curves observed earlier could in part be explained by the large sound intensities used during mechanical measurements.

The observation of cochlear nonlinearity also offered a solution to the problem of the miniscule vibration amplitudes predicted by Békésy for sound pressure levels close to the threshold of hearing. For later reference, we will now discuss this aspect

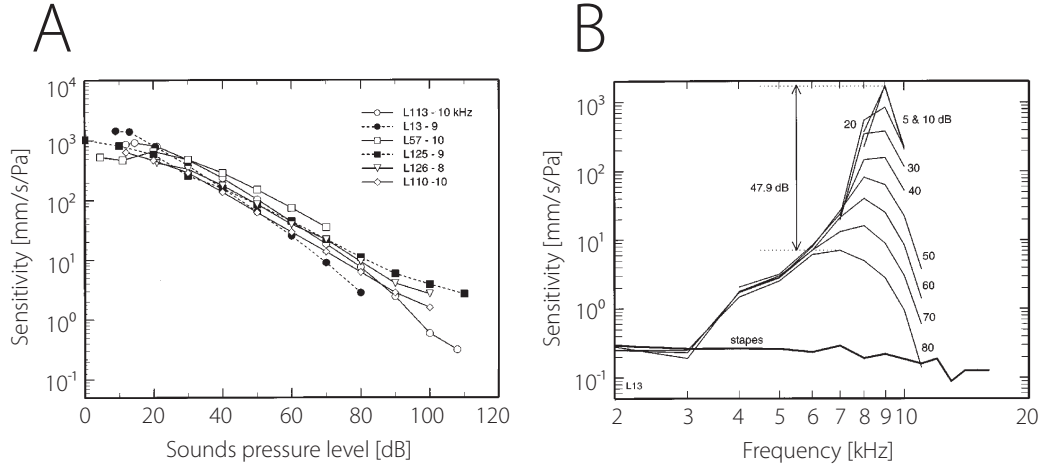


Figure 1.5: Nonlinearity of basilar membrane responses. One way to quantify basilar-membrane responses to pure-tone stimulation, is by means of the sensitivity. This is defined here as the ratio of the peak response velocity, as measured at a specific location on the basilar membrane, and the applied stimulus sound pressure level. Note that the peak velocity is proportional to the amplitude of the vibration. A linear system, for which the output is proportional to the input, would be characterized by a constant sensitivity. In (A), data obtained for several chinchilla cochlea is displayed. The stimulation frequency was adjusted to agree with the respective characteristic frequency of the monitored location. For weak stimulus intensities, sensitivity is almost constant, indicative of a linear response regime of the basilar membrane. For intermediate stimulus intensities, sensitivity decreases in a nonlinear fashion along with increasing sound pressure level. Note that the data is shown on a log-log-scale. For intense stimulation, sensitivity typically saturates, i.e. the response becomes linear again. In order to prevent damage to the cochlear preparation, stimulation with such high sound pressure levels is usually not performed. Also for the data shown, only the onset of the saturation can be discerned. In (B), sensitivity curves for various sound pressure levels are shown for a single location on the basilar membrane as a function of stimulus frequency. The characteristic frequency of the chosen location was about 9 kHz. Several observations can be made. When stimulating away from the characteristic frequency, sensitivity is almost constant. Note for example the data corresponding to a stimulation at 6 kHz. At the characteristic frequency, however, sensitivity decreases with increasing stimulus pressure. As a result, the basilar membrane for lower sound pressure levels seems more sharply tuned. Also, the peak of the sensitivity curves shifts to slightly lower frequencies with increasing sound pressure level. Adapted from ref. [141].

in slightly more technical detail. Given a fixed location along the cochlea, we assume a stimulus is presented with sound pressure p at the respective characteristic frequency. We denote with x_{BM} the Fourier amplitude of basilar membrane vibrations at the stimulus frequency. The experimentally measured growth of the vibration amplitude $|x_{\text{BM}}|$ as a function of sound pressure level can often be well described by a power law of the form

$$|x_{\text{BM}}| \sim p^{1+\alpha_0}, \quad (1.1)$$

where values of α_0 in the range $-0.88 < \alpha_0 < -0.5$ have been reported ([138], see also fig. 1.6A). While for a linear system $\alpha_0 = 0$, negative values of α_0 reflect the sublinear growth of $|x_{\text{BM}}|$. As a consequence, the cochlea compresses a large range

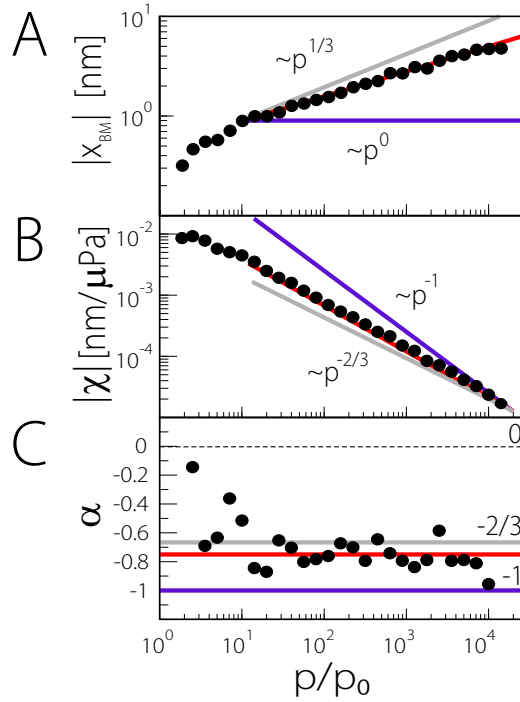


Figure 1.6: Local exponents of nonlinear compression. We present experimental data from ref. [123]. Basilar membrane responses were recorded in the guinea-pig close to the 18kHz location along the basilar membrane. All data are shown as a function of normalized sound pressure p/p_0 ($p_0 = 20\mu\text{Pa}$). In (A) the vibration amplitude $|x_{\text{BM}}|$ is displayed. Note its sublinear growth with increasing sound pressure. For comparison, we show power laws $|x_{\text{BM}}| \sim p^{1+\alpha_0}$ with exponents $\alpha_0 = -2/3$ (grey), $-3/4$ (red), -1 (purple). As we will show in section 1.3, $\alpha_0 = -2/3$ characterizes the response of a critical oscillator operating at a supercritical Hopf bifurcation. For the data shown, the growth of the response is well described by $\alpha_0 = -3/4$. (B) The same data as in (A) is shown in terms of the basilar membrane's sensitivity $\chi = |x_{\text{BM}}|/p$. We also indicate power laws of the form $|\chi| \sim p^{\alpha_0}$ for the same choices of α_0 as in (B). In (C) we plot the local exponent of nonlinear compression α as defined in eq. (1.3). The latter was determined by numerical differentiation of the data shown in (B). Note the crossover from values near 0 (linear response) for weak driving amplitudes, to a regime of nonlinear compression characterized by $\alpha \approx -0.75$. The exponents α_0 corresponding to the respective power laws shown in (B) are indicated as solid lines.

of input amplitudes into a smaller range of output amplitudes, a property referred to as nonlinear compression. In case of the cochlea, approximately six orders of magnitude in sound pressure level are compressed into as little as three orders of magnitude in basilar membrane vibrations. Given a vibration amplitude of about 10 nm in response to intense stimulation at about 120 dB [70], this implies that vibration amplitudes at threshold, i.e. at about 0 dB, are on the order of 0.1 nm [70]. Note that the latter value is about three orders of magnitude larger than that suggested by Békésy.

For weak sound intensities, the basilar membrane is often found to respond linearly to pure-tone stimulation, even at the characteristic frequency. In other words, the

degree of compression observed in basilar membrane response depends on sound pressure level. In terms of the sensitivity, defined as $|\chi| = |x_{\text{BM}}|/p$, eq. (1.1) yields

$$|\chi| \sim p^{\alpha_0}. \quad (1.2)$$

We propose a quantification of the sound pressure dependent degree of compression by means of the local exponent of nonlinear compression [99], defined as

$$\alpha = \frac{d \ln(|\chi|)}{d \ln(p)}. \quad (1.3)$$

For a power law of the form given in eq. (1.2), one finds that

$$\alpha \equiv \alpha_0.$$

Deviations of experimental data from a power law are thus reflected in the behavior of the local exponent α . Plotting α for the data shown in fig. 1.6B, the transition from linear response ($\alpha \approx 0$) to the regime of nonlinear compression ($\alpha \approx -0.75$) becomes apparent (see fig. 1.6C).

In 1977, David Kemp made another astonishing observation. The healthy human ear not only functions as a detector of auditory stimuli; it can also operate as an emitter of acoustic energy [83]. These so-called otoacoustic emissions can occur spontaneously and are amenable to recording by means of sensitive microphones introduced into the outer ear canal. Alternatively, they can be evoked by appropriate auditory stimulation. To this day, otoacoustic emissions have been recorded for a multitude of mammalian and non-mammalian vertebrate species [165, 128, 89, 103, 161]. As to evoked otoacoustic emissions, Kemp showed that upon simultaneous presentation of two pure tones with similar frequencies $f_1 > f_2$, the ear emits a tone at the distortion product frequency $2f_1 - f_2$ [85]. Distortion products are a sign of nonlinearity, since the output of a linear system contains only frequencies which are present in its input. At a time when Rhode's observations had not yet been reproduced, distortion product otoacoustic emissions therefore constituted a further clue toward cochlear nonlinearity [84]. Moreover, the phenomenon of spontaneous otoacoustic emissions was interpreted as a clear indication that the cochlea is in fact mechanically active, rather than being a passive detector.

By the 1950s, understanding of cochlear mechanics was thought to be essentially complete. By the beginning of the 1980s, however, the situation had changed fundamentally. Békésy's data had been recognized as reflecting passive cochlear mechanics only. When less compromised by dissection procedures and probed with sound pressure levels reaching well into the physiologically relevant range, the cochlea had been shown to exhibit a frequency dependent nonlinearity of unknown origin, boosting the response to low-amplitude sounds with gains on the order of 40-60 dB. At the same time, said nonlinearity had been found to sharpen the frequency selectivity of the ear for weak stimuli. Furthermore, based on the discovery of otoacoustic

emissions, the cochlea had been identified as mechanically active, with its operation being physiologically vulnerable.

The proposal of an active process being involved in human hearing, was not entirely new. As early as 1948, Thomas Gold had suggested that the observed frequency resolution of the human ear was linked to an amplificatory process [54, 53]. Presenting his arguments within the framework of Helmholtz’s resonance theory, Gold argued for an active mechanism, which on a cycle-by-cycle basis would be feeding energy into the cochlear partition in order to counter resistive losses. Furthermore, he envisioned that such a feedback mechanism, if exceeding a critical feedback strength, could generate oscillatory instabilities that in principle could be detected in the form of sound emissions radiating from the ear canal. At the time of his writing, Gold’s ideas were rejected by the majority of researchers. Today, in contrast, there is wide agreement that even though his arguments were based on a misguided interpretation of certain experimental data [56], many of Gold’s conclusions were remarkably insightful.

In 1983, many years after Gold’s proposal, Hallowall Davis attributed the newly discovered features of cochlear mechanics to the operation of a “cochlear amplifier” [32]. While leaving the physical principles underlying this “active process” unspecified, this term neatly summarizes the current paradigm of hearing research, as have before Helmholtz’s “resonance theory”, Békésy’s “traveling wave”, and Evans’ “second filter”. In short, the cochlea’s exquisite sensitivity and sharp frequency selectivity, the phenomenon of nonlinear compression, and the generation of spontaneous otoacoustic emissions are all thought to emerge from the operation of an active amplification mechanism.

During the course of the 1980s, two cellular processes were identified as potential candidates for the cochlea’s active process: membrane-based outer hair-cell electromotility [5] and active hair-bundle motility [110].

In 1983 William Brownell and colleagues discovered that outer hair cells can undergo changes of their length as a response to the modulation of their membrane potential, reminiscent of piezo-electric elements [15, 16]. These length changes, also referred to as electromotility, were shown to be linked to conformational transitions of the voltage-sensing membrane protein prestin [179]. The hypothesis of a concerted shortening and elongation of outer hair cells boosting basilar membrane vibrations is supported by at least two observations. On the one hand, in voltage-clamp experiments oscillatory shape-changes of isolated outer hair cells can be induced at auditory frequencies [31]. On the other hand, the ability of outer hair cells to cause movements of the basilar membrane was attested in experiments involving the application of transepithelial currents to intact cochlear preparations [100].

Another form of motility was found to reside within the sensory hair bundle itself. To this end, note that while electromotility is an evolutionary specialization of cochlear outer hair cells [106], hair bundles constitute the universal mechano-transducers in the auditory and vestibular system of all vertebrates. In 1985 Andrew Crawford and Robert Fettiplace showed that hair bundles in the cochlea of the

turtle are able to generate forces and even display spontaneous oscillations of their tip [27]. In subsequent years, various manifestations of active hair bundle motility have been observed *in vitro* in the eel [142], the frog [111], and the chicken [71]. Recently, signs of active force generation by hair bundles has also been reported for a mammalian species, namely the rat [86]. Activity of the hair bundle has been linked to myosin motors operating within the hair bundle [63, 152, 94]. As will be detailed in section 1.4, experiments performed on hair bundles from the sacculus of the bullfrog sacculus hint at the possibly active role of hair bundles in the process of mechanotransduction. Indeed, when driven with sinusoidal stimuli, hair bundles have been shown to be able to operate as tuned nonlinear amplifiers [112, 114].

Following the realization that the mammalian cochlea is mechanically active, signs of active amplification were also found in other mechanosensory organs of vertebrate and non-vertebrate species, such as the auditory papilla of the lizard [104], the antennal hearing organs of the fruitfly [55], and the semicircular canals of the toadfish [129]. The formation of a complete understanding of the biophysical principles underlying the various forms of active amplification at work within auditory and vestibular organs, is one of the central challenges for current hearing research [6].

1.3 Amplification by critical oscillators

The issue concerning the relative importance of electromotility versus hair-bundle motility for cochlear amplification remains unresolved [6]. Evidence for a hair-bundle-based mechanism, however, comes from the insight that the central features of cochlear amplification can be understood quite generically within the theoretical framework of driven oscillators [17, 39].

To this end, we consider a noiseless, nonlinear oscillator x , subject to an external periodic driving force

$$f = \sum_{n=-\infty}^{\infty} f_n e^{in\omega t}$$

with period $2\pi/\omega$ and complex Fourier modes f_n , obeying $f_n = f_{-n}^*$. Here, the asterisk denotes complex conjugation. We will assume that transients have decayed, as well as a 1:1 phase-locked response of the system under consideration [126]. Since it thus has the same period as the external driving, the time evolution of x can be written as a Fourier series of the form

$$x(t) = \sum_{n=-\infty}^{\infty} x_n e^{in\omega t},$$

where $x_n = x_{-n}^*$. For a suitably general class of dynamical systems [17], the Fourier modes f_n can be expressed as an expansion in the Fourier modes x_n [36]:

$$f_n = F_n^{(1)} x_n + \sum_k F_{nk}^{(2)} x_{n-k} x_k + \sum_{kl} F_{nkl}^{(3)} x_{n-k-l} x_k x_l + O(x^4). \quad (1.4)$$

Considering a simple sinusoidal stimulus, i.e. $f_n = 0$ for $n > 1$, eq. (1.4) gives rise to an approximate equation which captures the co-dependence of f_1 and the dominant Fourier mode of x , i.e. x_1 . It reads

$$f_1 = \mathcal{A}x_1 + \mathcal{B}|x_1|^2x_1. \quad (1.5)$$

Here \mathcal{A} and \mathcal{B} are complex coefficients which depend on the driving frequency, as well as on a control parameter r . The control parameter could for instance set the strength of an internal feedback mechanism or possibly shape the extent or form of a nonlinearity in the passive stiffness of the oscillator. Here, we will not specify the nature of r ; instructive examples can, however, be found in ref. [36]. The oscillator is said to be critical, if a frequency ω_c and a value r_c of the control parameter exist, such that $\mathcal{A}(\omega_c, r_c) = 0$.

Before discussing the response of a critical oscillator on the basis of eq. (1.5), we will show that criticality corresponds to the oscillator operating at an oscillatory instability, namely a supercritical Hopf bifurcation [156, 175]. This is characterized by a stable fixed point turning into a growing limit cycle upon the control parameter traversing a critical value (also see section 3.1). According to eq. (1.5), x allows for spontaneous limit-cycle oscillations in the absence of an external force if there exists a solution to the equation

$$|x_1|^2 = -\frac{\mathcal{A}}{\mathcal{B}}, \quad (1.6)$$

i.e. if there exists a frequency ω_s such that $-\mathcal{A}/\mathcal{B}$ is real and positive. Note that this is fulfilled for a critical oscillator with $r = r_c$, as in this case $\mathcal{A}(\omega_c, r_c) = 0$. The oscillator in this case performs oscillations of frequency ω_c , albeit with a vanishing amplitude. In order to discuss the behavior of the system for values of ω and r differing slightly from ω_c and r_c , respectively, we expand \mathcal{A} to first order as

$$\mathcal{A}(\omega, r) \approx A_1(\omega - \omega_c) + A_2(r - r_c),$$

where A_1 and A_2 are complex coefficients. The imaginary part of $-\mathcal{A}/\mathcal{B}$ vanishes for $\omega = \omega_s$, where

$$\omega_s = \omega_c + \frac{\text{Im}(A_2/\mathcal{B})}{\text{Im}(A_1/\mathcal{B})}(r_c - r).$$

Furthermore, in this case we find $-\mathcal{A}(\omega_s, r)/\mathcal{B}(\omega_s, r) \sim r - r_c$, such that the ratio changes its sign at the critical value r_c . We will assume without loss of generality that $-\mathcal{A}/\mathcal{B} > 0$ whenever $\omega = \omega_s$ and $r < r_c$. In this case, x performs spontaneous oscillations with an amplitude, which according to eq. (1.6) is determined by $|x_1|^2 = \Delta^2(r_c - r)/r_c$, where

$$\Delta^2 = r_c \left(\text{Re}(A_2/\mathcal{B}) - \text{Re}(A_1/\mathcal{B}) \frac{\text{Im}(A_2/\mathcal{B})}{\text{Im}(A_1/\mathcal{B})} \right).$$

For $r > r_c$ the system is quiescent. Hence, at the critical value r_c the system undergoes a supercritical Hopf bifurcation.

According to eq. (1.5), the response of a critical oscillator with $r = r_c$ to a driving force at the critical frequency ω_c , is given in terms of its fundamental Fourier mode by

$$|x_1| = |f_1|^{1/3} |\mathcal{B}|^{-1/3}. \quad (1.7)$$

Its response amplitude therefore grows sublinearly with the input amplitude. In terms of the sensitivity, here defined as $|\chi| = |x_1|/|f_1|$, eq. (1.7) can be rewritten as

$$|\chi| = |\mathcal{B}|^{-1/3} |f_1|^{-2/3}.$$

Sensitivity therefore decays according to a power law with exponent $-2/3$. In particular, the oscillator responds more and more sensitively for decreasing stimulus amplitudes. When driven with frequencies differing from ω_c , the nonlinear response of the system can be lost. Since for $\omega \neq \omega_c$ we have $\mathcal{A}(\omega, r_c) = A_1(\omega - \omega_c)$, the nonlinear term in eq. (1.5) will only dominate as long as

$$|x_1|^2 \gg |A_1(\omega - \omega_c)|/|\mathcal{B}|.$$

Using eq. (1.7), this implies that

$$|\omega - \omega_c| \ll |f_1|^{2/3} |\mathcal{B}|^{1/3} / |A_1|$$

must be fulfilled. In terms of the amplitude of driving, this inequality reads

$$|f_1| \gg |A_1(\omega - \omega_c)|^{3/2} |\mathcal{B}|^{-1/2}.$$

This shows that the response of the system is linear, in the case for which ω differs sufficiently from ω_c , or where the driving amplitude $|f_1|$ is small enough. In this linear regime, the sensitivity is constant and is given by

$$|\chi| = 1/|A_1(\omega - \omega_c)|.$$

In summary, the above arguments show that critical oscillators share many features observed for the cochlear amplifier. In particular, their response exhibits a frequency-dependent nonlinearity. Being most sensitive for low amplitude stimuli, sensitivity decays according to a power law with exponent $-2/3$. The latter compares favorably with exponents reported for the mammalian cochlea (see section 1.2). Furthermore, critical oscillators operating in the oscillatory regime might provide an explanation as to the origin of otoacoustic emissions. Important features characterizing the active traveling wave in the cochlea could indeed be reproduced in a cochlear description incorporating critical oscillators distributed along the basilar membrane [35].

Note that here we have considered a critical oscillator's response for $r = r_c$ and in the absence of fluctuations only. As we will show in the next section, oscillatory hair bundles from the sacculus of the bullfrog exhibit similar features as those discussed above. These hair bundles, however, operate in the oscillatory regime and are subject to intrinsic fluctuations. In chapter 3, we will therefore discuss the response of noisy oscillatory systems, operating on the oscillating side of a Hopf bifurcation.

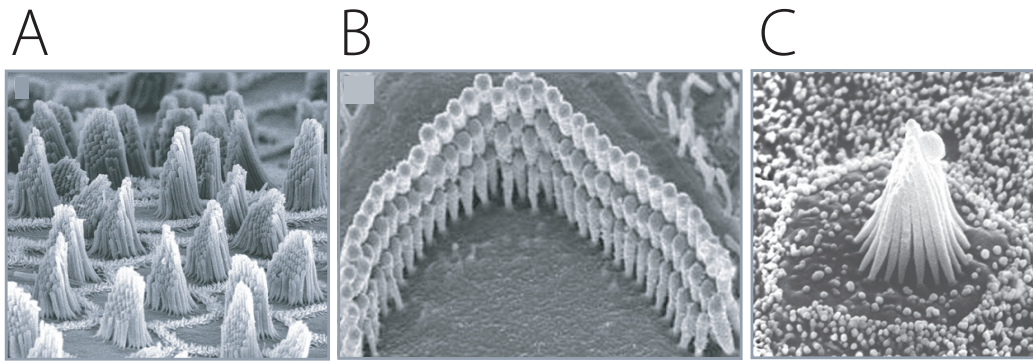


Figure 1.7: Hair-bundle morphology in various inner ear organs. While the arrangement of stereocilia is always regular, the actual shape of hair bundles can vary greatly from one inner ear organ to the next. We show in (A) hair bundles as found in the cochlea of the chicken (taken from ref. [70]), in (B) a V-shaped hair bundle of an outer hair cell from the cochlea of the rat (taken from ref. [96]), and in (C) a hair bundle from the sacculus of the bullfrog (taken from ref. [67]).

1.4 Active hair-bundle motility

In this section, we will discuss the biophysics of mechanosensory hair bundles in more detail. After a short excursion into hair-bundle morphology, some of the central experimental findings regarding active hair-bundle motility will be introduced. Following a review of a specific biophysical description of stochastic hair-bundle dynamics [118], this section will close with a discussion of hair-bundle coupling as realized *in vivo*.

1.4.1 Hair-bundle morphology

Hair bundles constitute the universal mechanotransducer in the auditory and vestibular system of all vertebrates. Note, however, hair bundles are also found in other sensory organs, as for instance in the electroreceptor organs of the paddlefish [78, 121]. Here, we will restrict our attention to the morphology of the hair bundle as observed in the inner ear. Despite their consistent role as mechano-electrical transducers, the actual shape of hair bundles can vary greatly from one inner ear organ to the next (see fig. 1.7), even within a single species. For example in the inner ear of the bullfrog, six hair-bundle types can be distinguished [98]. Some aspects of hair-bundle morphology, however, are preserved.

The hair bundle is a tuft of a few tens to a few hundreds stiff finger-like protrusions, termed stereocilia, emanating from the hair cell's so-called apical surface (see fig. 1.8A). The lengths of stereocilia typically vary between one to ten microns, while diameters ranging from a hundred to several hundred nanometers can be found [163]. The hair cell's plasma membrane encloses each stereocilium like a finger in a glove. Several hundred crosslinked actin fibers form the core of each stereocilium,

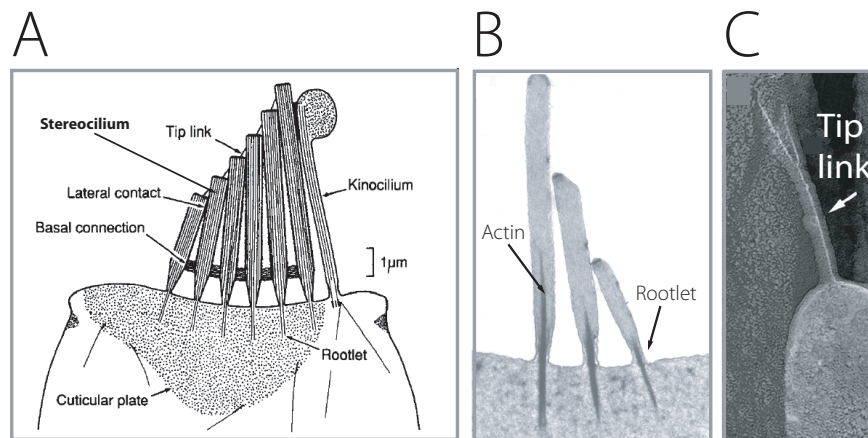


Figure 1.8: Important aspects of hair-bundle morphology. The structure of a hair bundle from the bullfrog's sacculus in (A) is illustrated by means of a sketch (adapted from ref. [137]). In particular, note the regular arrangement of stereocilia in rows of increasing height. As can also be seen in the microscopic image in (B), stereocilia taper near their base (adapted from ref. [43]). A few actin fibers form rootlets that anchor stereocilia to the cuticular plate. In (C) a microscopic image of a tip link connecting two stereocilia is shown (adapted from ref. [96]).

arranged in parallel to the long axis [162]. Stereocilia are of constant diameter for most of their length, but taper near their base (see fig. 1.8A and B). Only a few tens of the core's actin fibers extend beyond the insertion point of the stereocilium in the hair cell's apical surface. By forming rootlets, these few fibers effectively anchor each stereocilium to the so-called cuticular plate, an actin-rich structure that serves as a stable platform for the hair bundle. Within a hair bundle, stereocilia of different heights are arranged in form of an increasing staircase. Hair bundles typically exhibit a mirror symmetry with respect to a vertical plane that bisects the hair bundle parallel to the direction of increasing stereocilial heights.

Various lateral links establish connections between individual stereocilia. Among them the so-called tip links are of particular interest (see fig. 1.8A and C), as they are believed to play a central role in mechanotransduction. Tip links form interciliary bridges by attaching the tip of a stereocilium to the flank of a larger neighbor. In recent years, great efforts have been undertaken to understand the tip link's molecular structure [117]. According to the most promising theory to date, it is composed of two interacting homodimers of cadherin 23 (CDH23) and protocadherin 15 (PCDH15), respectively [82].

Some hair bundles also comprise a so-called kinocilium that is attached to the largest row of stereocilia (see fig. 1.8A and fig. 1.7C). It is a true cilium, as it contains an axoneme, i.e. nine doublets of microtubules arranged in a circular fashion around a central doublet [122]. Kinocilia often are present in immature hair bundles and recede after development is essentially complete [120]. In the sacculus of the bullfrog and various vestibular organs of other species, hair bundles are always

equipped with a kinocilium. While the kinocilium is known to be inessential for mechanotransduction [75], its contribution to hair-bundle functionality is still poorly understood.

Due to the reduced number of actin fibers in stereocilial rootlets, stereocilia are most flexible at their base. Hence, upon deflecting a hair bundle's tip, no buckling of stereocilia is observed. Responding essentially as stiff rods, stereocilia instead pivot about their points of insertion in the cuticular plate. The resulting combined pivotal stiffness K_{SP} of the hair bundle in the sacculus of the bullfrog is about 200 pN/nm [77, 109]. Recent dual-beam interferometry measurements reveal a very high coherence between the deflections of individual stereocilia [93]. No splaying or other internal modes of stereocilial movement can be detected. During deflection the hair bundle thus moves as a unit, with neighboring stereocilia performing a shearing motion relative to one another. Hair bundle tip movements along the direction of bilateral symmetry can thus be described by a single variable X . Deflections in the direction of the row of largest stereocilia are defined as positive by convention.

1.4.2 Hair-bundle oscillations in the sacculus of the bullfrog

Hair bundles from the sacculus of the bullfrog have been studied experimentally for many years [111]. In the bullfrog, the sacculus is an inner ear organ designed for the detection of low-frequency seismic vibrations and airborne sounds [97, 92]. In experiments, the sensory epithelium, the so-called saccular macula, is dissected and then mounted on a two-compartment cover slide. In this way, the basal and apical aspects of hair cells embedded in the saccular macula can be exposed to solutions of different ionic composition, as also realized *in vivo*. The basal side of the hair bundles is in contact with endolymph, which is similar to typical intracellular fluids. Compared to perilymph, i.e. typical extracellular fluids, it is characterized by a high concentration of potassium and low concentrations of calcium and sodium, respectively. The apical aspect of saccular hair cells, in contrast, is exposed to perilymph. The ionic composition of perilymph is marked by a low concentration of potassium and high concentrations of calcium and sodium, respectively. By means of projecting a hair bundle's tip onto a pair of photodiodes, its deflection X as a function of time can be recorded with subnanometer precision (for further details see ref. [111] and section 5.1).

Under these circumstances, hair bundles from the bullfrog's sacculus are routinely found to oscillate spontaneously, with oscillatory movements occurring along the X -axis (see fig. 1.9A). Hair-bundle oscillations resemble those of a relaxation oscillator. While spending most of the time in the vicinity of two extreme positions, the tip of the hair bundle undergoes fast switching events at stochastically distributed times. In the oscillation's histogram, two peaks, corresponding to the two extreme positions, can be discerned (see fig. 1.9B). Hair-bundle oscillations are not perfectly regular, but are inherently noisy (see fig. 1.9A). Typically, a peak is found in the power spectral density corresponding to a given oscillation, centered around a characteristic

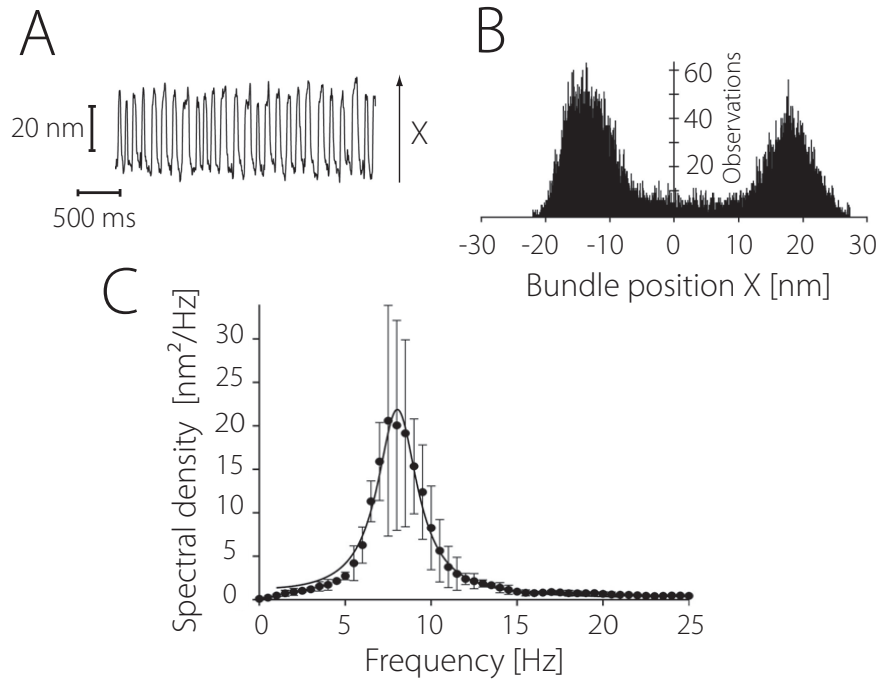


Figure 1.9: Spontaneous oscillations of hair bundles from the sacculus of the bullfrog. Under appropriate experimental conditions, hair bundles often perform spontaneous oscillations of their tip along the X -axis. In (A) a representative trajectory is shown with the X -axis indicated on the right. Note the fast switching events, reminiscent of a relaxation oscillator. (B) When plotting the oscillation's histogram of deflections, a bimodal shape is found. The two peaks correspond to the two extreme deflections. (C) The corresponding power spectrum displays a clearly defined peak at a characteristic frequency f_0 , here about 9 Hz. Due to the noisy character of the oscillation, the peak is smeared out. The black solid line corresponds to a fit with a generic Lorentzian line shape (see eq. (2.4) in chapter 2). Adapted from ref. [114]

frequency f_0 (see fig. 1.9C). In the sacculus of the bullfrog, frequencies in the range of about 5-50 Hz are observed [111]. The spectral peak, however, is smeared out, indicative of the noisy character of the oscillation. Note that a perfectly regular oscillation is characterized by a series of delta peaks in its power spectrum at the frequency of oscillation and possibly its higher harmonics.

The hair bundle's response to external stimulation can be probed by attaching a flexible glass fiber to its tip. By controlling the position of the fiber's base by means of a piezo-electric actuator, well-defined forces can be exerted (for further details see ref. [112] and section 5.1).

By comparing the hair bundle's linear response function to its autocorrelation function, it was shown that the hair bundle violates the fluctuation-dissipation theorem [113]. For a system in thermodynamic equilibrium, the fluctuation-dissipation theorem formulates a specific relation between the system's fluctuations and its linear response to weak amplitude stimuli. The hair bundle hence operates out of

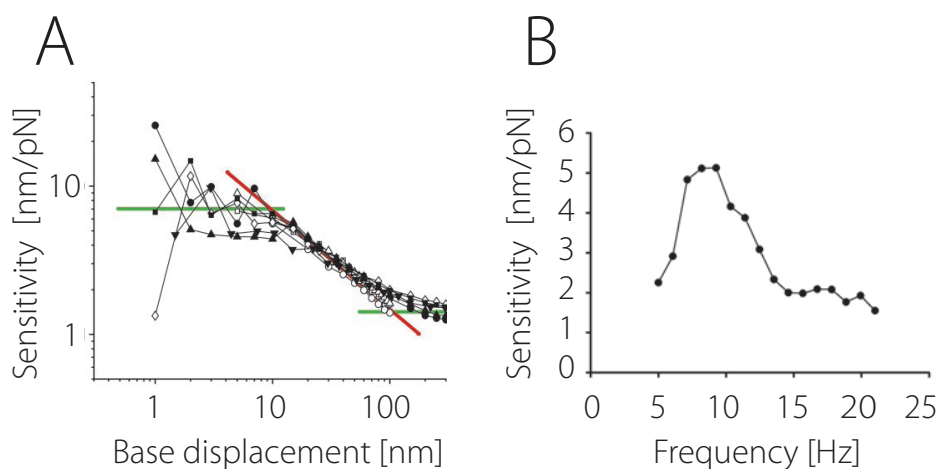


Figure 1.10: Response of an oscillatory hair bundle to a periodic driving. (A) When driven with a sinusoidal force at the characteristic frequency, the hair bundle's sensitivity exhibits three regimes. For weak driving amplitudes (equivalent to small displacements of the fiber's base), sensitivity plateaus at a maximal value. For intermediate forcing amplitudes, sensitivity drops in a nonlinear fashion. Its decay over one order of magnitude in driving amplitude is well-described by a power law with exponent $-2/3$ (red line). In the limit of strong stimuli, the sensitivity saturates. The two plateaus for weak and strong forcing are marked by green lines. (B) When driven in the linear response regime for weak stimuli, hair-bundle sensitivity as a function of driving frequency peaks at about the characteristic frequency. The hair bundle thus appears as a tuned element. Adapted from ref. [113].

thermodynamic equilibrium, such that the observed spontaneous oscillations are due to an energy-consuming mechanism at work within the hair bundle.

The response of an oscillating hair bundle exhibits features reminiscent of the response of critical oscillators discussed in the last section. When driven with a sinusoidal force at the characteristic frequency of spontaneous oscillation, the hair bundle responds most sensitively for weak driving amplitudes (see fig. 1.10A). In this weak-driving regime, sensitivity is found to be approximately constant, i.e. the hair bundle behaves linearly. For intermediate driving amplitudes, sensitivity decreases in a nonlinear fashion. The observed decay is well-described by a power law with an exponent of about $-2/3$. Note that this value agrees with the exponent describing the nonlinear decay of a critical oscillator's response, as well as values reported for the mammalian cochlea [138]. For strong stimuli, hair-bundle sensitivity saturates and the response is linear again.

The linear response level for weak stimuli depends on the frequency of driving (see fig. 1.10B). When driven at frequencies differing from the characteristic frequency, sensitivity is attenuated. The hair bundle hence constitutes a tuned element. When driven with high-level stimuli, sensitivity as a function of driving frequency, however, is almost constant (not shown).

In summary, the dynamics and response of an oscillatory hair bundle exhibit many features analogous to the cochlear amplifier. In particular, the hair bundle boosts

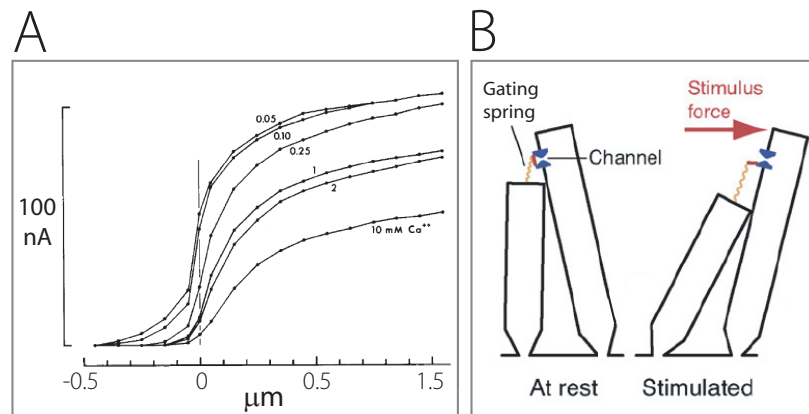


Figure 1.11: Mechanoelectrical transduction by hair cells. In (A), several current displacement curves are shown (adapted from ref. [23]). These reflect the total transepithelial current elicited by simultaneously stimulating several hundred hair bundles in the sacculus of the bullfrog. Recordings were performed for various Ca^{2+} concentrations in the endolymph bathing the apical side of the hair cells as indicated. Note the asymmetric sigmoidal shape and the dependence on the Ca^{2+} concentration. In (B), a sketch illustrates the gating-spring model of transduction (adapted from ref. [70]). A deflection of the hair bundle effects a shear of neighboring stereocilia. The increased tension in the gating springs leads to an opening of mechanosensitive channels.

its response to weak stimuli. As for the basilar membrane, the efficiency of this amplification process can be quantified by means of the amplification gain. A single hair bundle is found to have a gain of about 10, i.e. up to two orders of magnitude less than that observed for the mammalian cochlea.

In chapter 2 of this thesis, we will present results detailing the limitations of the hair bundle's gain due to the effect of intrinsic fluctuations.

1.4.3 Physical description of hair-bundle dynamics

In this section we will review a specific biophysical description of hair-bundle dynamics as presented in ref. [118]. In the course of the presentation, we will comment on further experimental findings concerning hair-bundle operation.

At rest, a constant current of K^+ and Ca^{2+} enters the hair bundle through ion channels located at the tips of the stereocilia. Upon a positive displacement of the hair bundle's tip, an increase in this so-called receptor or transduction current is observed. In contrast, a deflection in the opposite direction leads to a diminished influx. The dependence of the receptor current on applied deflection is sigmoidal in shape (see fig. 1.11). The X -axis coincides with the hair bundle's direction of maximal mechanosensitivity, i.e. deflections along this axis elicit maximal responses of the receptor current [148]. The onset of the receptor current at room temperature is characterized by fast time constants on the order of only a few tens of microseconds [23, 134]. This renders the involvement of a chemical messenger system in the

process of mechanotransduction very unlikely. Instead, the existence of a more direct mechanical gating mechanism is widely accepted, commonly described by the gating-spring model [108].

According to this model, one or two mechanically gated ion channels are attached, possibly by means of additional elastic elements in series with it, to the lower and/or upper end of each tip link, respectively (see fig. 1.11B). The molecular nature of these transduction channels, as well as their exact localization have not yet been established with certainty (for reviews see refs. [52, 47]). Recent experiments, however, suggest that mechanosensitive ion channels can only be found at the lower end of each tip link [11]. The complex consisting of a tip link and putative additional elastic connectors is referred to as gating spring. A deflection of the hair bundle in the positive direction induces stereocilial shearing movements and thus augments the mechanical energy stored in the gating springs (see fig. 1.11B). As a consequence, these exert a stronger pull on the transduction channels and thus increase the probability P_o for the channels to be in the open state. As the hair cell's soma at rest is held at a negative potential with respect to the perilymph bathing its apical side [72], the opening of transduction channels leads to an increased receptor current.

Upon the opening of a channel, some of the tension stored in the attached gating spring is released, which leads to a shortening of the gating spring by a distance d , also known as the gating swing. In the case of hair bundles from the sacculus of the bullfrog, d was estimated to be about 8.05-8.35 nm [115].

Concerning the molecular identity of the gating spring, note that given their orientation parallel to the X -axis, tip links are well-positioned to transfer shearing movements of adjacent stereocilia into mechanical stresses acting on the transduction channels. Furthermore, their pharmacological disruption leads to a loss of mechanosensitivity of the hair bundle [8]. The tip link is thus clearly implicated in the process of mechanotransduction and also as an integral part of the gating spring. However, recent studies suggest that a solitary tip link consisting of CDH23 and PCDH15 would be too stiff to confer the necessary elasticity to the gating spring [150, 81]. It is therefore likely that it operates in series with additional elastic elements. The combined gating-spring stiffness K_{GS} as measured along the X -axis in the case of hair bundles from the bullfrog's sacculus can be estimated to be about 0.3-0.8 pN/nm [115].

Tension in the gating spring is not only determined by the deflection of the hair bundle. In the framework of the active motor model of adaptation [70] (see also below), it is also modulated by the activity of a group of molecular motors. This motor assembly is usually pictured as being concentrated on an insertional plaque which is attached to a transduction channel situated at the upper end of each tip link (see fig. 1.12)¹. These motors actively walk along actin filaments towards the stereocilium's tip consuming chemical energy in the form of ATP. In this way, the motor assembly stretches the attached gating spring. The motors come to a halt

¹Given recent results concerning the localization of transduction channels [11], molecular motors might, however, be attached in a different fashion to the upper end of the tip link [52].

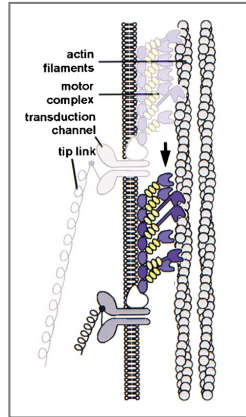


Figure 1.12: The adaption motor. An assembly of molecular motors is believed to modulate gating-spring tension. Being directly or indirectly attached to the gating spring, by actively walking toward the stereocilia's tip or passively sliding towards its base, these motors influence the open probability of the transduction channel(s). Image taken from ref. [63].

when the pull exerted by the gating spring equals their stall force. If tension in the gating spring exceeds this level, motors passively slip down towards the base of the stereocilium. The extent of gating spring tension accordingly depends on hair bundle deflection X , as well as on the motor assemblies' positions within the stereocilia. As stereocilia move in unison, it is natural to make the approximation that the activity of motor complexes within different stereocilia also occurs in parallel. Under this assumption, we can define a single variable X_a , corresponding to an effective motor position. Here, X_a is a projection of the motors' position along the long axis of stereocilia onto the axis of hair-bundle deflection. Note that an upward motion of the motors by convention corresponds to a movement in the negative direction along the X_a -axis.

In the case of the sacculus of the bullfrog, as well as the vestibular system of the rat, myosin 1c is the most likely candidate to power active regulation of gating-spring tension [63, 152]. In the case of the mouse cochlea, myosin VIIa has also been implicated in this process [94].

In the following, we will assume the transduction channel has two conformational states, corresponding to a single open and closed conformation, respectively. The equilibrium probability P_o to be in the open state, for a transduction complex consisting of an ion channel and an attached gating spring can be calculated as a function of X and X_a . In the absence of the gating spring, the closed state of the transduction channel is energetically favored and separated from the open state by an intrinsic energy difference of about $\Delta\mu \approx 10k_B T$ [69]. In order to calculate the energy difference $\Delta U = U_{\text{open}} - U_{\text{closed}}$ between the open and closed conformation of a single transduction complex (gating spring+channel), we note that due to the gating swing there is less energy stored in the gating spring when the channel is

open. More specifically, assuming the gating spring to be linear, one finds

$$U_{\text{open}} = \frac{K_{\text{GS}}}{2N}(X - X_a - D)^2 + \Delta\mu \quad \text{and} \quad U_{\text{closed}} = \frac{K_{\text{GS}}}{2N}(X - X_a)^2.$$

Here N is the number of parallel transduction complexes in the hair bundle. Note that the stiffness of a single gating spring is therefore given by K_{GS}/N . Furthermore, $D = d/\gamma$, where γ is a projection factor relating movements along the stereocilial axis to movements along the X -axis. In the case of the bullfrog's sacculus it was estimated that $\gamma = 0.14$ [75]. The origins of X and X_a have been chosen so as to ensure that (i) the stereocilial pivots do not exert forces for $X = 0$ and (ii) gating springs are at rest when the channel is closed and $X - X_a = 0$. One finds

$$\Delta U = \Delta\mu + \frac{K_{\text{GS}}D}{N} \left(\frac{D}{2} - (X - X_a) \right).$$

The open probability P_o in equilibrium is given by the Boltzmann distribution as

$$P_o(X, X_a) = \frac{1}{1 + Ae^{\frac{-K_{\text{GS}}D(X - X_a)}{Nk_B T}}},$$

where $A = \exp[\frac{N\Delta\mu + \frac{1}{2}K_{\text{GS}}D^2}{Nk_B T}]$, k_B is the Boltzmann constant, and T denotes temperature. For a fixed motor position, X_a , the dependence of the channels' open probability P_o on the deflection X is sigmoidal in shape (see fig. 1.13A). As the receptor current entering the hair bundle is proportional to P_o , this compares favorably with the shape of observed current-displacement curves (cf. fig. 1.11). These curves, however, are not symmetric. Incorporating a second closed state of the transduction channel has been shown to be sufficient to reproduce this aspect of the transduction process [23]. We will not consider this detail here and retain the two-state model of channel gating.

For a given deflection, X , and motor position, X_a , the average force acting on the hair bundle along the X -axis, $\langle F_X \rangle$, is the sum of the force exerted by the stereocilial pivots and of all the gating springs within the hair bundle, i.e.

$$\begin{aligned} \langle F_X \rangle &= -N \left(\frac{\partial U_{\text{open}}}{\partial X} P_o + \frac{\partial U_{\text{closed}}}{\partial X} (1 - P_o) \right) - K_{\text{SP}} X \\ &= -K_{\text{GS}}(X - X_a - DP_o) - K_{\text{SP}} X. \end{aligned}$$

Assuming the hair bundle operates in an overdamped regime, and neglecting the influence of noise, the dynamics of X can be written as

$$\lambda \dot{X} = -K_{\text{GS}}(X - X_a - DP_o) - K_{\text{SP}} X, \quad (1.8)$$

where λ is a friction coefficient.

For a fixed motor position X_a , the force $\langle F_X \rangle$ does not depend linearly on the displacement X (see fig. 1.13B). Indeed, so-called nonlinear stiffness has been measured

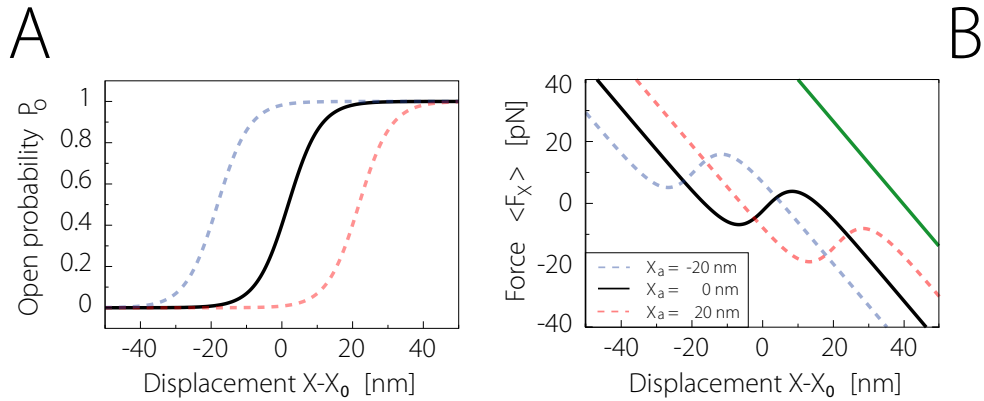


Figure 1.13: Open probability and force-displacement curve. (A) For three different values of X_a as indicated (legend in (B)), the open probability $P_o(X, X_a)$ is shown as a function of displacement X . A change of the motor position effects a shift of P_o along the X -axis. (B) For the same X_a as in (A), we show the force-displacement curve as given by $\langle F_X \rangle|_{X_a}$. The green line indicates a slope of $K_{SP} + K_{GS}$, corresponding to the stiffness of the hair bundle for large displacements. Note the region of negative stiffness for small displacements. A change of X_a , by shifting the open probability of the transduction channels, also effects a corresponding shift of the force-displacement curve. Note that tip displacement for this plot is measured with respect to a reference position, X_0 , which is defined by the condition $P_o(X_0, 0) = 0.5$.

in vitro for hair bundles in various species [66, 115, 132, 86]. In these experiments, after abruptly deflecting its tip, the necessary force to clamp the hair bundle at the prescribed position is recorded. In particular, for small deflections that induce only a fraction of the transduction channels to open or close, the hair bundle appears softer than for large deflections. Here, the hair bundle essentially behaves like a linear spring with stiffness $K_{SP} + K_{GS}$ (see fig. 1.13B). As the reduced stiffness for small deflections is ultimately due to the gating swing associated with channel opening, it is also termed "gating compliance" [66]. Under ionic conditions mimicking the situation *in vivo*, gating compliance can be so strong as to render hair bundle stiffness negative for small displacements [115].

The hair bundle is thought to benefit from the motor-based regulation mechanism of gating-spring tension in form of its ability to adapt to persistent stimuli. Large deflections saturate the transduction apparatus by opening or closing a large fraction of the mechanosensitive channels. In order to retain its responsiveness to small deflections in the presence of an ongoing static stimulus, the hair bundle thus needs to reset tension in the gating springs and effectively shift the current-displacement curve. As sketched in fig. 1.14B, after an initial sharp increase of the transduction current in response to a positive deflection of the hair bundle a decay of the ionic influx is observed. This decrease is usually described as the linear superposition of a fast and a slow exponentially decaying component [177]. The fast component, with time constants as fast as $40 \mu\text{s}$ in the rat's cochlea [134], reflects the rapid reclosure of transduction channels immediately after their initial opening. Several possible

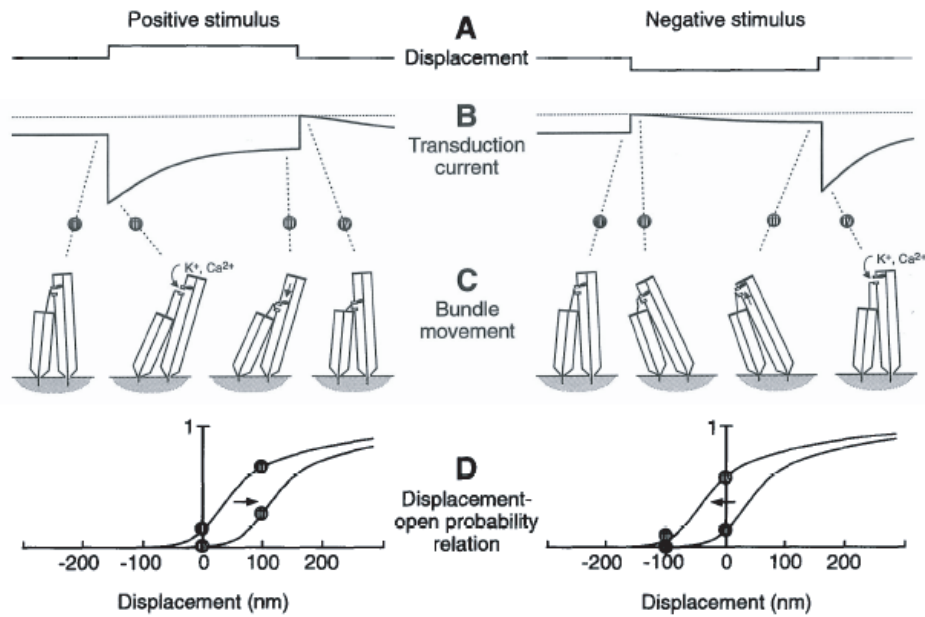


Figure 1.14: Motor-mediated adaptation. A static deflection, applied to the hair bundle in the positive X -direction (sketched in A, left panel), elicits an increase of the transduction current (sketched in B, left panel, time point (i)). According to the gating-spring model of transduction, the open probability of mechano-sensitive ion channels (sketched in D, left panel) is increased by the augmented tension in the gating-springs (see C, left panel). Gating-spring tension is thought to be subsequently released by the passive slippage of molecular motors, which are exerting a pull on the gating-springs from within the individual stereocilia (time points (ii) to (iii)). After the end of the stimulus, gating-springs slacken and ion-channels close (time point (iv)). As the motors over the course of the stimulus have slid down on the actin filaments, gating-spring tension is reduced as compared to before the onset of the stimulus. The transduction current is therefore reduced. Movements of the adaptation motors, in other words, effect a shift of the relation between the displacement of the hair bundle, X , and the open probability of the ion channels, P_o . Adaptation can also be observed for stimuli in the negative direction (right panels). Upon an initial closure of the ion-channels, active motor movements in direction of the stereocilia's tips reset gating-spring tension, resulting in the reopening of some of the ion channels. After the end of the stimulus, as motors have moved upwards, the transduction current compared to before the onset of the stimulus is transiently increased. Taken from ref. [73].

mechanisms have been suggested to be responsible for fast adaptation (for a concise review see ref. [110]). For example, it was hypothesized that a change in the local Ca^{2+} concentration on the inside of the stereocilia could alter the transduction channel's free energy landscape and render its closed state energetically more favorable, i.e. effectively increase $\Delta\mu$ [66, 19].

Slow adaptation is most pronounced for large deflections and is marked by longer time constants, e.g. in the sacculus of the bullfrog on the order of 10-1,000 milliseconds [65, 59, 177]. This second component of adaptation can readily be accounted for within the framework of the active motor model (see fig. 1.14). Deflecting the hair bundle in the positive direction stretches gating-springs. By causing mechanosensi-

tive channels to open, this in turn leads to a sudden increase in the receptor current. Unable to maintain the large tension in the gating spring, the adaptation motors slide toward the base of the stereocilium. Due to the resulting reduced tension in the gating springs, ion channels gradually close, corresponding to the decrease registered in the transduction current. Similarly, a stimulus acting in the negative direction instead decreases tension in the gating spring. The induced closing of transduction channels leads to an attenuation of the receptor current. The motor assembly subsequently moves toward the tips of stereocilia and restores gating-spring tension, thereby effectively causing the transduction current to rise again. In both cases, adaptation leads to a shift of the current-displacement curve (see fig. 1.14D, and compare fig. 1.13A). A stimulus of same polarity superimposed over the first, will lead to the same increase or decrease of the receptor current as the initial one. Note, however, that adaptation is not complete. Gating-spring tension cannot be entirely released by a passive slippage of the adaptation motors. The receptor current after adaptation has reached its steady state, accordingly is slightly higher than before application of the stimulus. Likewise, a negative deflection cannot be fully adapted by the active movement of the motors. We will in the following, however, ignore the effect of incomplete adaptation.

Various experimental findings have established that the extent, as well as the kinetics, of the adaptation process are linked to the Ca^{2+} component of the receptor current [23, 37, 62, 7, 26]. In particular, a reduction of the extracellular calcium concentration slows the adaptive process to positive deflections. One way to account for this observation is to describe the total stall force F_a along the X -axis corresponding to N adaptation motors as depending on the local calcium concentration $[\text{Ca}^{2+}]$ at the motors' sites of attachment. As calcium dynamics are fast compared with hair-bundle movements and thus can be viewed as equilibrating instantaneously, the dependence of $[\text{Ca}^{2+}]$ on the channels' open probability P_o can be approximated to linear order as

$$[\text{Ca}^{2+}] \approx [\text{Ca}^{2+}]_0 + [\text{Ca}^{2+}]_m P_o.$$

The experimental data suggest that the maximal stall force of the adaptation motors, denoted by F_{\max} , is realized when the local calcium concentration is lowest, i.e. in the case of closed ion channels. A linear expansion of the calcium dependence of F_a around this reference state then leads to

$$\begin{aligned} F_a &\approx F_{\max} + \left. \frac{dF_a}{d[\text{Ca}^{2+}]} \right|_{P_o=0} [\text{Ca}^{2+}]_m P_o \\ &= F_{\max}(1 - SP_o). \end{aligned}$$

The dimensionless parameter

$$S = - \left. \frac{dF_a}{d[\text{Ca}^{2+}]} \right|_{P_o=0} \frac{[\text{Ca}^{2+}]_m}{F_{\max}}$$

captures the nature and strength of the calcium feedback on motor activity. In line with observations [44], this feedback will be assumed to be negative, i.e. $S > 0$. In

other words, Ca^{2+} is assumed to downregulate the motors' force production. This could be realized by calcium modulating the motor's attachment probability to the actin filaments.

Based on the assumption of a simple linear force-velocity relationship and taking active motor forces as well as passive elastic forces due to the N gating springs into account, the dynamics of the motor variable X_a can be written as

$$\begin{aligned}\lambda_a \dot{X}_a &= -N \left(\frac{\partial U_{\text{open}}}{\partial X_a} P_o + \frac{\partial U_{\text{closed}}}{\partial X_a} (1 - P_o) \right) - F_a \\ &= K_{\text{GS}}(X - X_a - DP_o) - F_{\text{max}}(1 - SP_o),\end{aligned}\tag{1.9}$$

where λ_a is a friction coefficient.

The dynamic eqs. (1.8) and (1.9) constitute a deterministic description of hair-bundle dynamics in the form of two coupled differential equations. Note that due to the sigmoidal shape of P_o , the resulting system is nonlinear.

Most parameters appearing in eq. (1.10) and eq. (1.11) can be estimated on the basis of experimental observations (see table 1.1), except for the maximal motor force F_{max} and the feedback strength S . The system's state diagram can be calculated as a function of these two free parameters by means of linear stability analysis of the system's fixed points [118]. Four different regimes can be distinguished (see fig. 1.15). When adaptation motors are weak, they are unable to sufficiently increase gating-spring tension in order for it to cause an opening of the transduction channels. In this regime the system is monostable, with its single stable fixed point corresponding to a state of the hair bundle with most transduction channels being closed. Also in the case of large maximal motor forces, only one stable fixed point exists. In this parameter regime, however, the motors maintain sufficient gating spring tension in order to render transduction channels mostly open. For intermediate maximal motor forces and mild feedback strengths, the system is bistable. Within a bounded region of parameter space, corresponding to large motor forces and large feedback strengths, the system's only attractor is a stable limit cycle, and the system is thus oscillatory. The corresponding bifurcation lines in the state diagram correspond to supercritical and subcritical Hopf bifurcations, respectively, depending on the exact choice of parameters.

As discussed in section 1.4.2, hair bundle dynamics are inherently noisy. Indeed, it has been shown that in order to describe hair-bundle dynamics faithfully, the effects of various noise sources have to be taken into account [118]. Noise acting on the hair bundle's deflection X is due to thermal interactions with the surrounding fluid, as well as so-called channel clatter. This term refers to fluctuating forces corresponding to a change in gating spring tension caused by stochastic transitions of the transducer channels. Fluctuations influencing the motor variable X_a are related to the probabilistic binding and unbinding of individual motor molecules to the actin filaments. Fluctuations can be incorporated into this description by means of additional noise terms. We will thus deal with the following system of coupled

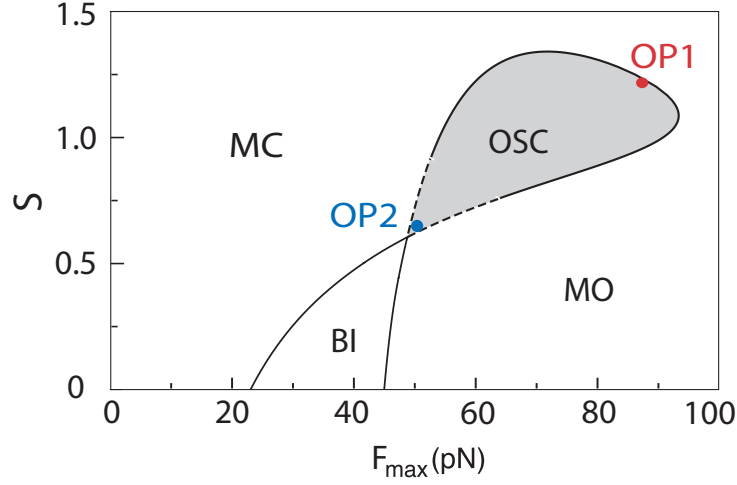


Figure 1.15: Phase diagram of the deterministic hair-bundle description eq. (1.8) and eq. (1.9) in terms of the maximal motor force F_{\max} and the calcium feedback strength S . Four dynamical regimes can be distinguished. Apart from a region of bistability (BI), two regions of monostability are found (MC+MO). For low maximal motor force and strong calcium feedback, transduction channels are mostly closed (MC). In the case of strong motors and weak calcium feedback, channels are mostly open (MO). Within a bounded region in parameter space (gray area) the system becomes oscillatory (OSC). The transition into the oscillator regime occurs via a supercritical (solid line) or subcritical (dashed) Hopf bifurcation. We indicate two operation points, namely OP1, close to the supercritical and OP2, close to the subcritical bifurcation. OP2 corresponds to a parameter set studied earlier [118]. The parameters of OP1 and OP2 are given in table 1.1. Modified from ref. [118].

stochastic differential equations,

$$\lambda \dot{X} = -K_{\text{GS}}(X - X_a - DP_o) - K_{\text{SP}}X + F_{\text{ext}}(t) + \xi(t) \quad (1.10)$$

$$\lambda_a \dot{X}_a = K_{\text{GS}}(X - X_a - DP_o) - F_{\max}(1 - SP_o) + \xi_a(t), \quad (1.11)$$

where $\xi(t)$ and $\xi_a(t)$ are assumed to be independent Gaussian white noise terms whose noise strengths are given in terms of autocorrelation functions as

$$\langle \xi(t)\xi(t') \rangle = 2k_B T \lambda \delta(t - t') \quad \text{and} \quad \langle \xi_a(t)\xi_a(t') \rangle = 2k_B T_a \lambda_a \delta(t - t'), \quad (1.12)$$

respectively. Here, $T_a = 1.5T$ denotes an effective temperature. In addition to thermal excitations, the motor variable X_a was argued to be subject to non-equilibrium fluctuations, originating in the active force production of adaptation motors [118]. In the above description, this is reflected by a choice of $T_a > T$. The friction coefficient $\lambda_a \approx 10 \mu\text{Ns/m}$ for hair bundles from the bullfrog's sacculus can be estimated from the initial adaptation rate of the receptor current following the onset of step stimuli of varying magnitude [59]. The hair bundle's deflection X , in contrast, is assumed to be subject to thermal fluctuations only, captured by an effective friction coefficient λ . More specifically, $\lambda = \lambda_h + \lambda_c$, where λ_h reflects hydrodynamic friction and λ_c is related to channel clatter. The friction coefficient λ_h can be estimated by

Parameter	Definition	Value
λ	Friction coefficient of the hair bundle	$2.8 \mu\text{N}\cdot\text{s}\cdot\text{m}^{-1}$
λ_a	Friction coefficient of adaptation motors	$10.0 \mu\text{N}\cdot\text{s}\cdot\text{m}^{-1}$
K_{GS}	Combined gating-spring stiffness	$0.75 \text{mN}\cdot\text{m}^{-1}$
K_{SP}	Combined stiffness of stereociliary pivots	$0.6 \text{mN}\cdot\text{m}^{-1}$
D	Gating-swing of a transduction channel	60.9 nm
N	Number of stereocilia	50
T	Ambient temperature	300K
T_a	Effective temperature	1.5T
ΔG	Intrinsic energy change on channel opening	$10k_B T$
<hr/>		
F_{max}	Maximal motor force	OP1 : 87.571 pN OP2 : 50.243 pN
S	Feedback strength	OP1 : 1.22 OP2 : 0.65

Table 1.1: Table of parameters corresponding to OP1 (red disc in fig. 1.15) and OP2 (blue disc in fig. 1.15). Note that OP1 corresponds to a parameter set studied earlier [118]. The two operation points differ in the choice of the maximal motor force, F_{max} , and the feedback strength, S .

taking into account hair-bundle geometry and the viscosity of the solution bathing the hair bundle. In case of the bullfrog's sacculus, this yields $\lambda_h \approx 0.13\mu\text{Ns}/\text{m}$ [66, 33]. In the framework of a two-state description of transduction-channel gating, the effect of channel clatter for hair bundles from the same sensory organ was estimated to be $\lambda_c \approx 3\mu\text{Ns}/\text{m}$ [118]. In other words, channel clatter is believed to dominate hair-bundle friction.

The response to an external driving force applied at the hair bundle's tip can be studied by adding an appropriate nonzero driving term, $F_{\text{ext}}(t)$, to the dynamic equation for X , i.e. eq. (1.10).

When noise is taken into account, for choices of F_{max} and S in the oscillatory region, numerical simulations of eq. (1.10) and eq. (1.11) generate noisy oscillations, reminiscent of observed oscillations for hair bundles from the bullfrog's sacculus (see next chapter). As shown in ref. [118], for an operation point corresponding to the blue disc in fig. 1.15, the overall shape of the oscillation and its spectral statistics quantitatively match those of a specific hair bundle observed *in vitro* (cf. fig. 1.9A,C and fig. 2.1A,B). In addition, this hair bundle's nonlinear response function is faithfully reproduced (cf. fig. 1.10A and fig. 2.5B). We will refer to this choice of parameters (see table 1.1) as standard parameters or as operation point two (OP2). Note that OP2 is close to a subcritical Hopf bifurcation. In the next chapter we will also present numerical results for a choice of parameters correspond-

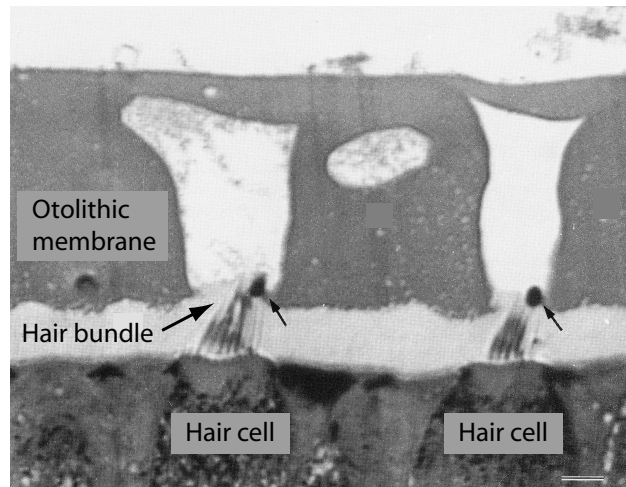


Figure 1.16: Coupled hair bundles in the sacculus of the bullfrog. The otolithic membrane in the sacculus of the bullfrog lies over the saccular macula. Over each hair bundle, a large cavity is found. Hair bundles are attached via their kinocilium to the cavity's wall. Modified from ref. [80].

ing to the red disc in fig. 1.15 (see table 1.1). This operation point will be referred to as operation point one (OP1). Residing within the oscillatory regime, OP1 is in the immediate vicinity of a supercritical Hopf bifurcation.

1.4.4 Coupling of hair bundles *in vivo*

As pointed out earlier, in the mammalian cochlea the tips of outer hair-cell bundles are embedded into the overlying tectorial membrane (see fig. 1.2B). Similar accessory structures are realized in a multitude of other inner ear organs. In the sacculus of the bullfrog, hair bundles are attached via their kinocilium to the overlying otolithic membrane (see fig. 1.16). In the auditory epithelia of lizards a great variety of morphological structures interconnecting sensory hair bundles has evolved [102]. In addition to continuous tectorial membranes, in some species so-called chains of tectorial sallets are observed. These constitute discrete membranous units, connecting to only a small group of neighboring hair bundles.

In all cases, the membranous material overlying hair bundles is of a visco-elastic nature [80, 10, 58, 135, 50]. Hence, most hair-bundles *in vivo* do not operate in isolation. Instead, hair-bundle coupling appears to be a widespread morphological specialization implemented in the inner ear of vertebrates. Several findings suggest a beneficial role of hair-bundle coupling for the process of mechanotransduction.

One indication comes from the comparison of two lizard species, the alligator lizard (*Gerrhonotus multicarinatus*) and the Australian bobtail skink (*Tiliqua rugosa*) [101]. While the alligator lizard in its auditory papilla exhibits free standing hair bundles, for the bobtail skink a chain of about 80 tectorial sallets is observed to

cover the papilla's high-frequency region. Based on neural threshold-tuning curves obtained for these two lizard species, the bobtail skink was found to exhibit lower thresholds on average, i.e. a higher sensitivity. Also, the degree of frequency selectivity of single nerve fibers in the bobtail skink was found to be about twice as good as in the alligator lizard.

The sense of echo-location as observed in bats constitutes another indication of coupling-induced enhancement of mechano-sensation. A specialized region, the so-called acoustic fovea, in the cochlea of bats is devoted to the detection of echo-signals in a very narrow frequency band. In the mustached bat (*Pteronotus parnelli*), the acoustic fovea represents about 50% (7 mm) of cochlear length and thus recruits nearly half of the available hair cells [91]. In total, approximately 2000 coupled outer hair cells operate in the acoustic fovea. Extremely sharp mechanical resonances have been measured on the basilar membrane [90]. Also, the tuning of auditory nerve fibers is much sharper than in other species.

1.5 Coupled oscillators and synchronization

Ensembles of coupled oscillatory systems are encountered in a multitude of contexts. Swarms of flashing fireflies [159] and networks of spiking neurons [40] constitute examples from the biological realm. Coupled oscillators, however, also play a prominent role in various fields of physics [174] and chemistry [95]. A universal feature observed in all these systems is a tendency of the oscillators to synchronize to a common oscillation frequency. For instance, cardiac pacemaker cells in the sino-atrial node synchronize their rhythmic firing and in this way trigger contractions of the heart muscle [76].

Analogous to the emergence of spatial order in magnetic spin systems as for instance the Ising model, synchronization can be interpreted as the emergence of order in time. A first theoretical treatment of synchronization was presented in 1967 by Arthur Winfree [176]. Effectively restricting his attention to systems of coupled phase oscillators (see section 3), he argued that synchronization occurs if coupling exceeds a certain threshold strength. Refining Winfree's arguments, Yoshiki Kuramoto could show analytically that the onset of synchronization in systems of globally coupled phase oscillators, indeed, bears similarities with a phase transition [95].

Over the last decades, many variants of the by now classical Kuramoto model have been studied (for a review see ref. [4]). Next to more general coupling functions [28, 29], also various coupling topologies [144] have been considered. Generalizing in a different direction, instead of dealing with phase oscillators of fixed amplitudes, ensembles of more general nonlinear oscillators, often Hopf oscillators (see chapter 3), have been investigated [116, 136, 166]. For instance, it was shown that with the oscillation amplitude also being variable, coupling of very heterogeneous ensembles of oscillators can lead to so-called "amplitude death", i.e. loss of the oscillatory behavior [41, 124].

In the context of this thesis, the incorporation of fluctuations is of particular interest [158, 131, 126, 178, 4]. Noise in most cases at least partially counteracts the ordering effect of coupling. Synchronization, however, can also be observed in systems of coupled noisy oscillators [126]. Most importantly, coupling-induced synchronization was shown in certain settings to bring about an effective noise reduction, with the noise strength of each individual oscillator being reduced in proportion to the system size [18].

Several biological examples of such coupling-induced noise reduction have been reported. For one, the coherence of genetic oscillations in cells forming the segmentation clock in zebrafish was shown to be enhanced by intercell coupling [64]. Similarly, the coefficient of variation characterizing the interbeat intervals of groups of ventricular cells from the chick heart was found to decrease in proportion to the number of cells within a given cluster [21].

Given the observations discussed in the last section, we conclude that elastic coupling of active oscillatory hair bundles might enhance the sensitivity and frequency selectivity of mechanotransduction by inner ear organs. In chapters 4 and 5 of this thesis, we will investigate this possibility from a theoretical as well as experimental point of view.

1.6 Outline of this thesis

In this thesis, we will study the signal detection properties of single and coupled hair bundles as well as those of generic noisy oscillators.

In chapter 2, the dynamics of a single hair bundle will be considered. In the framework of the biophysical description presented above, we will show that the phase coherence as well as the amplification gain of an isolated hair bundle is ultimately limited by intrinsic fluctuations. In particular, noise reduction leads to a profound enhancement of the hair bundle's frequency tuning and sensitivity to weak amplitude stimuli. We will extend our discussion of the local exponent of nonlinear compression, as presented for the mammalian cochlea, to the response of a periodically driven hair bundle.

In order to gain a better understanding as to the observed effects of noise reduction on hair-bundle performance, in chapter 3 we will study the dynamics of the noisy phase and Hopf oscillator. The latter constitutes a generic description for oscillations close to a Hopf bifurcation. We will analyze how phase diffusion and amplitude fluctuations shape the oscillator's spontaneous dynamics as well as its response to periodic stimulation. In particular, an analytical expression for the full nonlinear response function of the noisy Hopf oscillator will be derived. Several regimes of nonlinear compression will be discussed and analyzed in terms of the local exponent of nonlinear compression.

Chapter 4 is devoted to a theoretical investigation of the dynamics of elastically coupled hair bundles. We will present results of a computational study, attesting to

the beneficial effect of coupling on a hair bundle's signal detection and amplification properties. In addition to homogeneous systems, we will also discuss systems with inherent frequency gradients as realized in the mammalian cochlea. In the framework of a mean-field argument, we will show that the observed effects are due to an effective noise reduction induced by elastic coupling.

Finally, the results of an *in vitro* study will be presented in chapter 5. In order to experimentally investigate the dynamics of a hair bundle upon coupling to neighbors of similar characteristics, we combined micromanipulation experiments with real-time computer simulations. By means of a dynamic force-clamp procedure we coupled a hair bundle from the sacculus of the bullfrog to two independent stochastic simulations of hair-bundle dynamics, in this experiment also referred to as cyber clones. Our experimental results parallel the findings discussed in chapter 4. In particular, they attest the hair bundle's ability to constructively integrate into groups of elastically coupled hair bundles.

Chapter 2

Noise-imposed limits of hair-bundle performance

In this chapter, the effects of intrinsic fluctuations on hair-bundle dynamics will be discussed and illustrated. To this end, we will present numerical results obtained within the framework of stochastic hair-bundle motility that was reviewed in the last chapter. Fluctuations will be shown not only to limit the phase coherence of spontaneous oscillations, but also to constrain the sensitivity of the hair bundle to external periodic stimulation. Most importantly, it will become apparent that by reducing the level of intrinsic fluctuations the performance of the hair bundle as a tuned nonlinear amplifier can be greatly enhanced.

2.1 Quality of spontaneous oscillations

Throughout this section, we will assume $F_{\text{ext}} = 0$, i.e. only spontaneous hair-bundle activity will be considered. When choosing parameters corresponding to OP1 and OP2 introduced above (see fig. 1.15 and table 1.1), numerical simulations of eqs. (1.10) and (1.11) result in an oscillatory behavior of the deflection variable X (see fig. 2.1A) and the effective motor variable X_a (not shown). Since in experiments only hair-bundle deflection is amenable to direct observation, we will in the following discuss hair-bundle dynamics exclusively in terms of X . The oscillations at OP2 resemble those of a relaxation oscillator [156]. Spending most of its time in the vicinity of one of two extreme positions, the tip of the hair bundle at stochastically distributed times undergoes rapid transitions between these two states [20]. In the trajectory corresponding to OP1, in contrast, no separation of different time scales can be discerned. At OP1, movements have a root-mean-squared amplitude A_{RMS} of about 8nm, in case of OP2 one finds a slightly larger value of 15nm. Hair-bundle oscillations are noisy. Questions as to their spectral statistics are best discussed in terms of their power spectral density and autocorrelation function.

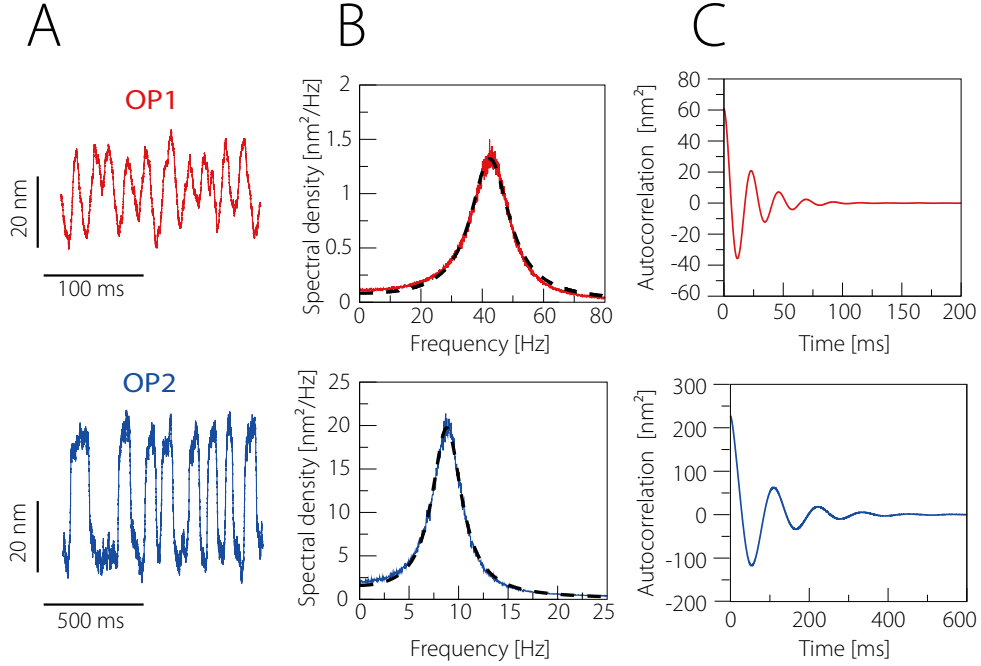


Figure 2.1: Noisy hair-bundle oscillations. (A) Sample trajectories of the deflection X for OP1 (top, red trace) and OP2 (bottom, blue trace). (B) Power spectral densities S_X (OP1: red trace, top; OP2: blue trace, bottom) corresponding to the dynamics shown in (A). In both cases a fit with eq. (2.4) is shown as a dashed black line. (C) Autocorrelation functions corresponding to the power spectral densities shown in (B) (OP1: red trace, top; OP2: blue trace, bottom). Note the decay of correlations within about three oscillation cycles.

In general, for a stationary stochastic process $z(t)$, where $z(t)$ can be either complex or real, the autocorrelation function $C_z(\tau)$ at time τ is defined as

$$C_z(\tau) = \langle z(t)z^*(t + \tau) \rangle - \langle z(t) \rangle \langle z^*(t + \tau) \rangle, \quad (2.1)$$

where $\langle \dots \rangle$ denotes an ensemble average and the asterisk $*$ denotes complex conjugation. The power spectrum or power spectral density $S_z(f)$ as a function of frequency is given by

$$S_z(f) = \lim_{T \rightarrow \infty} \frac{\langle \tilde{z} \tilde{z}^* \rangle}{T}, \quad (2.2)$$

where \tilde{z} denotes the Fourier transform of z over the finite time window T , i.e.

$$\tilde{z}(f) = \int_0^T z(t) e^{i2\pi f t} dt. \quad (2.3)$$

The autocorrelation function and the power spectral density are related by means of the Fourier transform. The Wiener-Kinchine-theorem [49] states

$$S_z(f) = \int_{-\infty}^{\infty} C_z(\tau) e^{i2\pi f \tau} d\tau,$$

where without loss of generality we have assumed that $\langle z \rangle = 0$. A non-zero stationary average of z gives rise to additional delta peaks at zero frequency.

In fig. 2.1B, power spectra S_X are shown, corresponding to the X -dynamics at OP1 and OP2, respectively. For both operation points a well-defined peak centered at a characteristic frequency f_0 marks the typical frequency content of hair-bundle movements. Oscillations at OP1 ($f_0 \approx 42.5\text{Hz}$) are considerably faster than at OP2 ($f_0 \approx 8.9\text{Hz}$). The finite width of the spectral peaks is a consequence of fluctuations destroying the phase coherence of the hair bundles' limit cycle oscillations. Note that the power spectrum of a noiseless oscillatory system would consist of discrete delta peaks at multiples of the oscillation period. Power spectra of noisy oscillatory hair bundles are instead well described by the sum of two shifted Lorentzians [118, 79]

$$S_X(f) \approx \frac{D}{K^2 + \Lambda^2(f - f_0)^2} + \frac{D}{K^2 + \Lambda^2(f + f_0)^2}, \quad (2.4)$$

where $D, K, \Lambda > 0$ (see fig. 2.1B).

The finite phase coherence of hair-bundle oscillations becomes even more tangible in terms of the deflections' autocorrelation function C_X . For an oscillatory hair bundle C_X corresponds to a damped oscillation with frequency f_0 (see fig. 2.1C). Indeed, making use of eq. (2.4) an application of the Wiener-Kinchine-theorem shows

$$C_X(f) = \frac{2\pi D}{K\Lambda} e^{-\frac{2\pi K|\tau|}{\Lambda}} \cos(2\pi f_0 \tau). \quad (2.5)$$

Due to fluctuations, correlations in the deflection of a hair bundle thus decay with a characteristic time scale

$$\tau_{\text{corr}} = \frac{\Lambda}{2\pi K}.$$

The degree of phase coherence can be quantified by means of the quality factor Q , which roughly spoken measures the number of oscillation cycles in the autocorrelation function before correlations have died out. It is formally defined as

$$Q = \pi f_0 \tau_{\text{corr}},$$

but can also be calculated from the spectrum as

$$Q = \frac{f_0}{f_r - f_l}, \quad (2.6)$$

where f_r and f_l are chosen such that $S(f_r) = S(f_l) = S(f_0)/2$ and $f_r > f_l$. The magnitude $f_r - f_l$ is also referred to as the half-width of the spectrum. Neglecting the second summand in eq. (2.4), for given S_X the corresponding quality Q is given by

$$Q = \frac{\Lambda f_0}{2K}.$$

A fit with eq. (2.4) shows that oscillations at OP1 have a quality factor $Q \approx 2.7$. For OP2 one finds $Q \approx 2.4$.

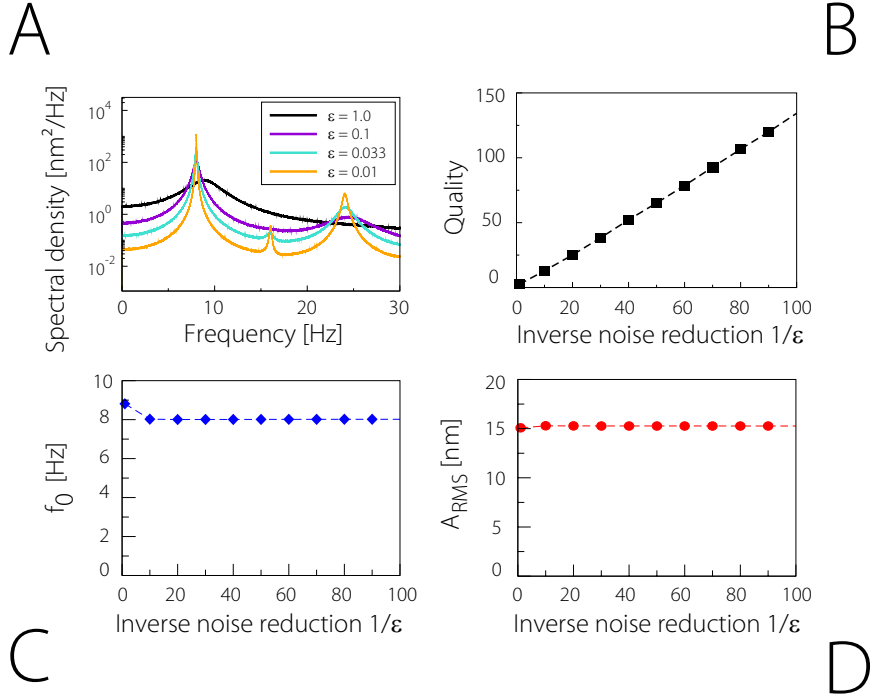


Figure 2.2: The effect of noise reduction on spontaneous oscillations at OP2. (A) Several power spectra of the X -dynamics are shown for four different values of the noise reduction factor ε as indicated. Note the sharpening of the spectral peak at the characteristic frequency. With decreasing noise strengths, higher harmonics at multiples of the characteristic frequency appear. (B) The quality of spontaneous oscillations as estimated by a fit with eq. (2.4) is shown as a function of inverse noise reduction factor. A linear increase is found. In (C), the characteristic frequency f_0 and in (D), the root-mean-squared amplitude A_{RMS} of the deflection X are shown as a function of inverse noise reduction factor. Both change only mildly upon a reduction of the noise strength.

In order to study hair-bundle dynamics for varying noise strengths, we introduce the noise-reduction factor ε . The latter is used to uniformly scale the autocorrelation functions of both $\xi(t)$ and $\xi_a(t)$, i.e. in the remainder of this chapter for given ε we consider their noise strengths to be given by

$$\langle \xi(t)\xi(t') \rangle = \varepsilon 2k_B T \lambda \delta(t - t') \quad \text{and} \quad \langle \xi_a(t)\xi_a(t') \rangle = \varepsilon 2k_B T_a \lambda_a \delta(t - t'),$$

respectively. The choice $\varepsilon = 1$ conforms with the original estimates of noise intensities presented in the last chapter. Setting $\varepsilon < 1$ corresponds to an effective noise reduction. The case of an increased level of fluctuations, i.e. $\varepsilon > 1$, will not be considered.

For OP2, in fig. 2.2A we plot power spectral densities S_X for various noise reduction factors ε in the range 0.01 – 1.0. With decreasing ε , the spectral peak considerably sharpens and higher harmonics are clearly distinguishable. By means

of a fit with eq. (2.4) the quality of oscillation Q was estimated. Note, however, the presence of higher harmonics is not reflected by the generic eq. (2.4). The quality factor Q as a function of inverse noise reduction factor $1/\varepsilon$ increases almost linearly (see fig. 2.2B). The characteristic frequency f_0 as well as the root-mean-squared amplitude A_{RMS} of the oscillations, in contrast, upon a reduction of the noise level change only mildly (less than 10%) (see fig. 2.2C and D).

We have further investigated whether the effect of noise reduction on the quality of spontaneous oscillations crucially depends on the hair bundle's operation point (see fig. 2.3). For $\varepsilon = 0.01, 0.1, 1.0$ we have performed simulations for all choices $F_{\text{max}} = i \cdot \Delta F_{\text{max}}$ and $S = j \cdot \Delta S$ with $\Delta F_{\text{max}} = 10\text{pN}$, $\Delta S = 0.05$, $i = 0, \dots, 71$, and $j = 0, \dots, 31$, i.e. covering the whole phase diagram as shown in fig. 1.15. For each set of parameters the power spectral density S_X was computed and fit with the Lorentzian ansatz eq. (2.4). Note, however, that for parameter choices in the monostable and bistable regimes, in close proximity to the Hopf bifurcations spectral densities can deviate from a purely Lorentzian shape (not shown). For all parameter values within the oscillatory regime, a reduction of the noise strength leads to a profound increase of the oscillations' phase coherence. In all three cases the point of maximal phase coherence was close to the center of the bounded oscillatory region, with a reduction of ε only having a mild effect on its exact position.

From the above we conclude that for an oscillatory hair bundle a reduction of intrinsic fluctuations enhances the quality of spontaneous oscillations. Note that in the absence of noise, i.e. $\varepsilon = 0$, being a deterministic limit cycle oscillator, oscillations of the hair bundle would have an infinite phase coherence. The described noise dependence of the oscillations' regularity distinguish the hair-bundle description used from another classical oscillatory system, namely the noisy damped harmonic oscillator defined as

$$\ddot{x} = -\lambda\dot{x} - kx + \xi(t).$$

Here λ denotes friction, k is a stiffness coefficient, and $\xi(t)$ is assumed to be Gaussian white noise with $\langle \xi(t)\xi(t') \rangle = 2d\delta(t-t')$. For this system, the power spectral density S_x can be calculated explicitly¹. It is given by

$$S_x(f) = \frac{2d}{(k - (2\pi f)^2)^2 + \lambda^2(2\pi f)^2}.$$

The spectrum scales linearly with d . Hence, while the amplitude of the oscillation depends on the noise intensity, its quality does not. Note, however, the damped harmonic oscillator in the absence of noise is quiescent. In the next chapter, we will discuss in more detail the effects of noise on the dynamics of two generic oscillators, namely the noisy phase and the noisy Hopf oscillator.

¹Write eq. (2.1) as a two-dimensional Ornstein-Uhlenbeck process and use results from [49].

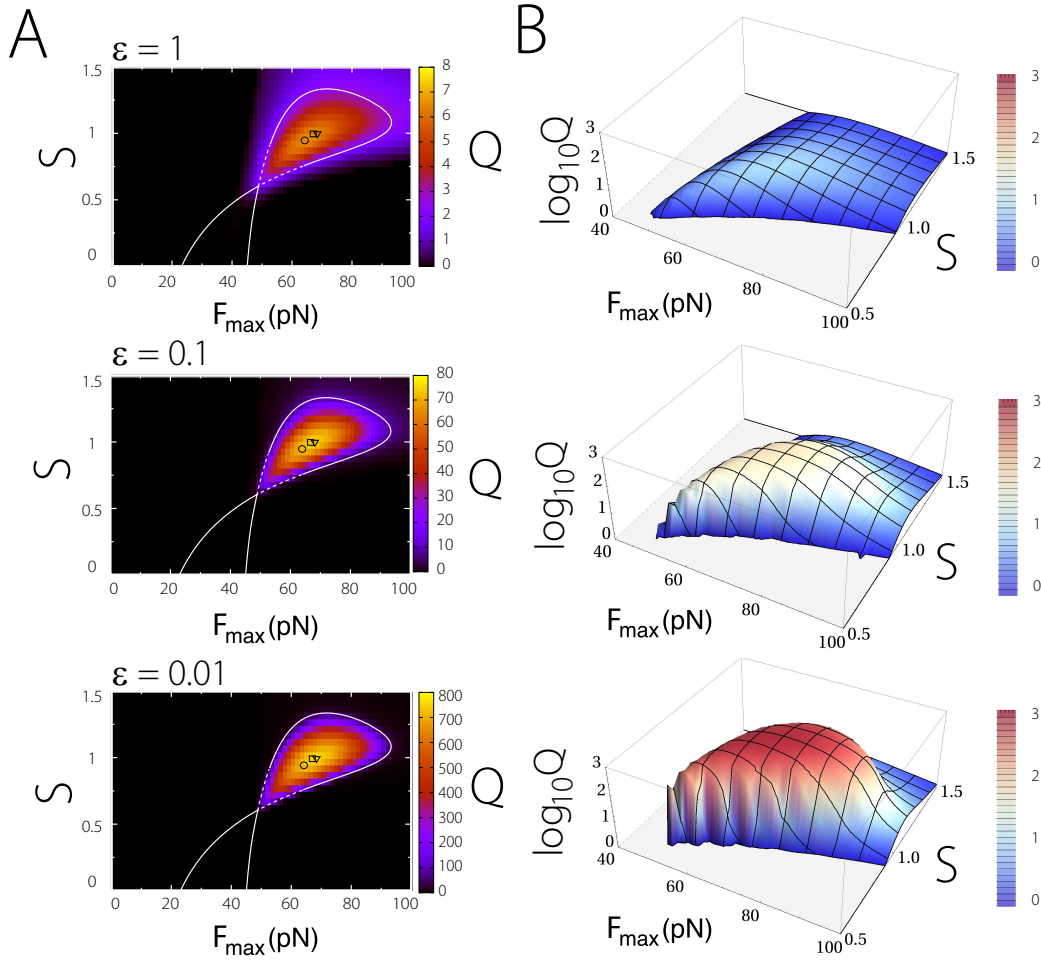


Figure 2.3: Dependence of the effects of noise reduction on the operation point of the hair bundle. In (A), for three choices of the noise reduction factor ε (indicated on top of the panels on the left side), we show a color plot of the quality factor Q as a function of the operation point of the hair bundle within the F_{\max} - S -plane. Note that the color scheme is scaled with a factor 10 for each reduction of ε by a factor 10. In all panels, we indicate the noise-dependent operation point of maximal phase coherence (\circ : $\varepsilon = 1$ - \square : $\varepsilon = 0.1$ - \triangle : $\varepsilon = 0.01$). (B) The same data as in (A) is shown with a logarithmic scale. Note the profound increase of the quality factor within the oscillatory region.

2.2 Amplification gain

In this section, the performance of the hair bundle as a detector of periodic stimuli will be analyzed. Most prominently, we will discuss the influence of intrinsic fluctuations on the hair bundle's ability to act as a nonlinear amplifier.

When a hair bundle is driven by a sinusoidal stimulus $F_{\text{ext}}(t) = F \cos(2\pi f_s t)$ of amplitude F and driving frequency f_s (see fig. 2.4A, top), after a transient it responds with a periodic mean motion $\langle X(t) \rangle$ of the same frequency (see fig. 2.4A, bottom). This response in general contains higher harmonics of the driving fre-

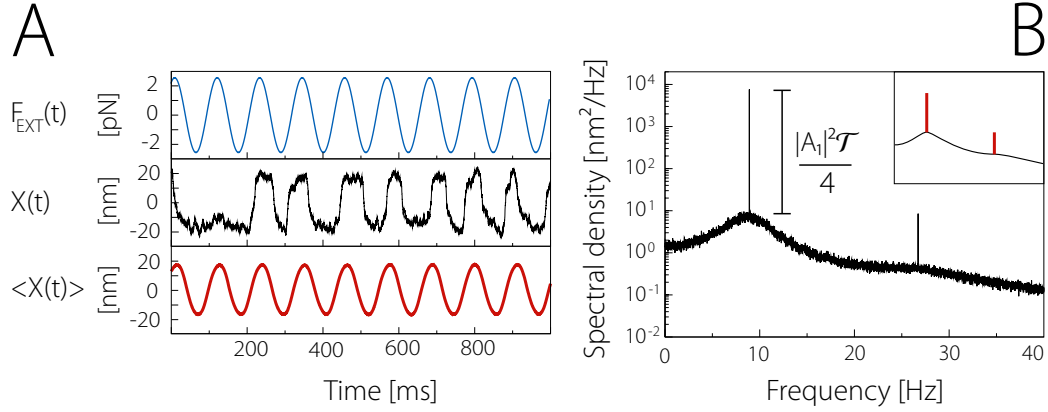


Figure 2.4: Response of the hair bundle to a periodic forcing. (A) An external periodic driving $F_{\text{ext}}(t) = F \cos(2\pi f_s t)$ of amplitude F and driving frequency f_s (top, blue trace, $f_s = 8.9\text{Hz}$, $F = 2.5\text{pN}$) modulates the statistics of hair-bundle dynamics. While for small driving amplitudes the hair bundle mainly responds by phase-locking to the external signal (middle, black trace, parameters corresponding to OP2), for large driving forces also the amplitude of the oscillatory movements is increased (not shown). These modulations lead to an oscillatory behavior of the time dependent average $\langle X(t) \rangle$ (bottom, red trace) with a frequency that coincides with the frequency f_s of the applied driving. (B) In terms of the driven hair bundle’s power spectral density S_X , an external stimulus leads to the presence of discrete peaks (marked red in the inset) at the driving frequency and its higher harmonics, in addition to a continuous background spectrum S_0 (black line in the inset). These peaks correspond to the Fourier modes (see eq. (2.7)) present in the time dependent average (red trace in (A), bottom). The peak height at the fundamental frequency in case of a finite observation time \mathcal{T} is given by $\frac{|A_1|^2 \mathcal{T}}{4}$.

quency and can be expressed as a Fourier series

$$\langle X(t) \rangle = \frac{A_0}{2} + \sum_{n=1}^{\infty} A_n \cos(2\pi n f_s t - \phi_n),$$

where $\frac{A_0}{2}$ captures a possibly nonzero static shift of the time-dependent mean value, and ϕ_n denotes the phase shift of the n th Fourier mode. Hence, when plotting the power spectral density S_X corresponding to a periodically driven hair bundle, next to a continuously varying part, denoted by S_0 , discrete peaks are present at frequencies $n f_s$ (see fig. 2.4B). Assuming a finite observation/simulation time \mathcal{T} , the height of these peaks is well approximated by

$$S_X(n f_s) - S_0(n f_s) \approx \frac{|A_n|^2 \mathcal{T}}{4}. \quad (2.7)$$

The sensitivity $|\chi|(F, f_s)$ of the hair bundle is defined as

$$|\chi|(F, f_s) = |A_1/F|$$

and thus has units of a compliance. It describes the elicited output amplitude at the fundamental frequency per unit driving force. Note that the sensitivity $|\chi|(F, f_s)$ depends on the amplitude F , as well as on the frequency f_s of the applied driving.

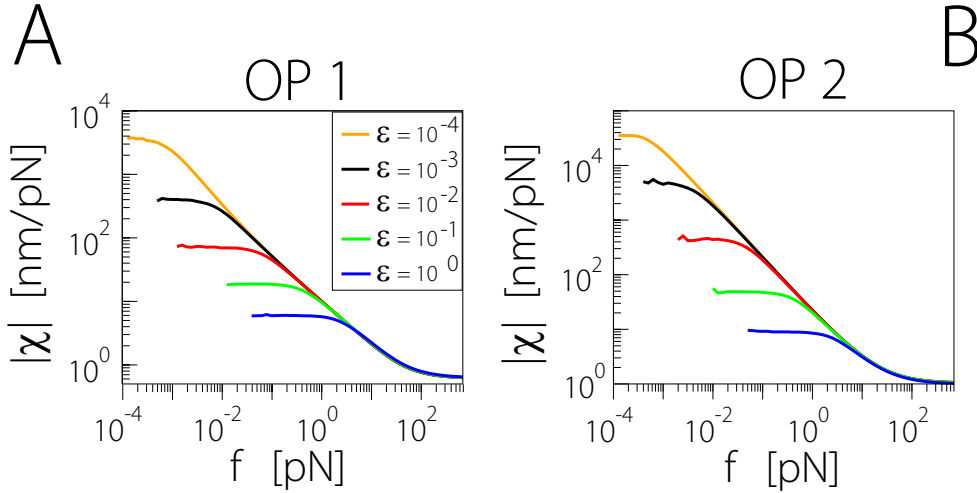


Figure 2.5: The effects of noise reduction on the sensitivity of the hair bundle model. We show the sensitivity $|\chi|(F, f_0)$ as a function of forcing amplitude for various noise reduction factors ε as indicated. Parameters were chosen to correspond to operation point OP1 in (A) and to OP2 in (B). Sensitivities were determined numerically from the response to a driving $F_{\text{ext}}(t) = F \cos(2\pi f_0 t)$ at the characteristic frequency f_0 of spontaneous oscillations.

Choosing parameters corresponding to OP1 and OP2, we determined the hair bundle's sensitivity $|\chi|(F, f_0)$ as a function of the driving amplitude F for various noise reduction factors (see fig. 2.5). Note that the driving frequency was chosen to coincide with the respective characteristic frequency f_0 , i.e. the stimulus was tuned to the noise-level dependent frequency of spontaneous oscillations. The sensitivity for both operation points as well as all noise reduction factors exhibits three different response regimes. For weak driving amplitudes, a linear response regime manifests itself in form of a plateau at a noise-dependent level. With decreasing noise strength, sensitivity in this regime is greatly enhanced. For intermediate driving amplitudes, sensitivity decays in a nonlinear fashion. The range of forces over which nonlinear compression is observed, with decreasing noise intensity extends to smaller forcing amplitudes. In the limit of strong driving, the hair bundle's response is linear again, with its sensitivity being independent of the noise intensity.

In the latter regime, the hair bundle's sensitivity, i.e.

$$|\chi_\infty|(f_s) := \lim_{F \rightarrow \infty} |\chi|(F, f_s),$$

can be calculated analytically. To this end note that for sufficiently large driving amplitudes, the contribution of the active adaptation motors, as well as the effects of gating-compliance can be neglected, i.e. one can set $F_{\text{max}} = 0$ and $D = 0$. Under

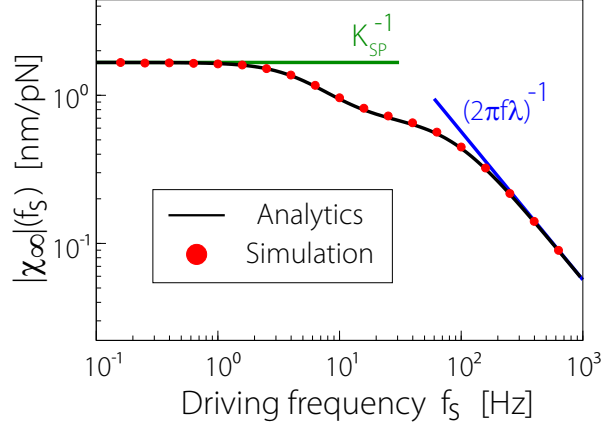


Figure 2.6: Passive response of the hair bundle model. The linear response level in the limit of strong driving, i.e. $|\chi_\infty|(f_s)$, is shown as a function of driving frequency f_s . Simulation results (red discs) were obtained for OP2 with $F = 1000\text{pN}$. We indicate the asymptotic limits for static (green line) and high frequency driving (blue line).

these assumptions, $|\chi_\infty|(f_s)$ is given by²

$$|\chi_\infty|(f_s) = \sqrt{\frac{K_{\text{GS}}^2/(4\pi^2) + \lambda_a^2 f_s^2}{2\tilde{K}\lambda_a^2 f_s^2 + \lambda_a^2 f_s^2(K_{\text{SP}}^2 + \lambda^2 4\pi^2 f_s^2) + \tilde{K}^2/(4\pi^2) + K_{\text{GS}}^2(\lambda + \lambda_a)^2 f_s^2}},$$

where $\tilde{K} = K_{\text{GS}}K_{\text{SP}}$. For large forces the hair bundle thus essentially responds like a passive low pass filter, with its sensitivity for a static driving being set by its passive stiffness K_{SP} and in the limit of large driving frequencies by its friction coefficient λ (see fig. 2.6). In particular, $|\chi_\infty|(f_s)$ is independent of the hair bundle's operation point and also of the noise strength. Note that the latter feature is shared by all noisy linear systems which are driven by white noise. The observed enhancement upon noise reduction of the sensitivity for small forcing amplitudes therefore is related to the nonlinear nature of the system. As mentioned earlier, one way to quantify the effectiveness of the active process in boosting the hair bundle's response in this regime, is by means of the so called gain G . It is formally defined as

$$G = \lim_{F \rightarrow 0} |\chi|(F, f_0)/|\chi_\infty|(f_0). \quad (2.8)$$

²Note that eqs. (1.10) and (1.11) with $F_{\text{max}} = 0$ and $D = 0$ define a two-dimensional Ornstein-Uhlenbeck process with a periodic driving $F_{\text{ext}}(t) = F \cos(2\pi f_s t)$ which is entering in the equation for X . Taking an ensemble average yields dynamic equations for the time-dependent averages $\langle X(t) \rangle$ and $\langle X_a(t) \rangle$. Assuming an infinite time window, Fourier transforming the system leads to algebraic equations for $\langle \tilde{X} \rangle$ and $\langle \tilde{X}_a \rangle$. Furthermore note that because the system is linear, its response will not contain higher harmonics of the driving, such that $\langle \tilde{X} \rangle = A_1/2(\delta(f - f_s) + \delta(f + f_s))$.

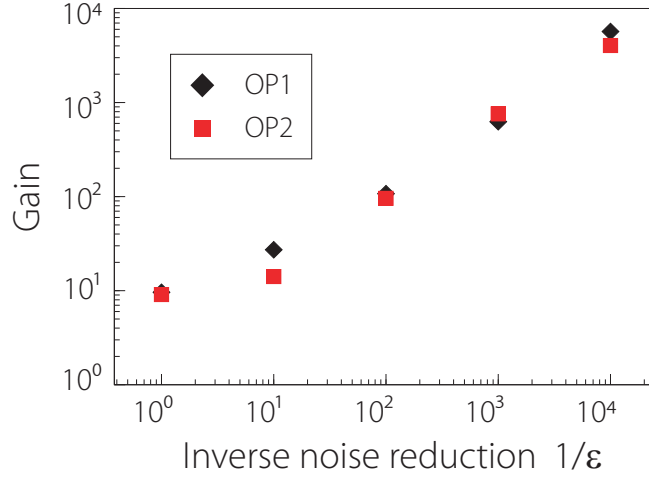


Figure 2.7: Gain of the hair-bundle model. The amplification gain G as obtained in simulations for OP1 and OP2 is plotted as a function of inverse noise reduction factor ε . Note the almost linear increase of G .

Hence, the gain of a linear system, for which the sensitivity as a function of driving amplitude is constant, is equal to unity. The gain of the hair bundle due to the nonlinearities shaping its dynamics at OP1 and OP2 for $\varepsilon = 1$, however, is about 10. This value compares favorably with gains as measured for single hair bundles in vitro [113]. When plotting the gain at OP1 and OP2 as a function of inverse noise reduction factor, an almost linear increase is found (see fig. 2.7).

We will now briefly discuss the case of detuned stimuli. In the following, $\Delta f = f_s - f_0$ will denote the frequency mismatch of the stimulus frequency f_s with respect to the hair bundle's characteristic frequency f_0 . We will present simulation results obtained for OP2. For $\varepsilon = 0.01$, in fig. 2.8A the sensitivity for various choices of the relative detuning $\Delta f/f_0$ is shown as a function of driving amplitude. In the linear response regime for weak amplitudes, sensitivity is greatly reduced. For intermediate forces, the hair bundle's response, as in the tuned case, is marked by a regime of nonlinear compression. In fig. 2.8B, the linear response level for weak stimuli is shown as a function of relative detuning. This plot provides evidence that noise reduction is most effective in enhancing the hair bundle's sensitivity for tuned stimuli. For detuned stimuli the enhancement effect is greatly reduced. A reduction of intrinsic fluctuations thus renders the hair bundle more tuned to stimuli within a more and more narrow frequency band. For $\varepsilon = 0.01$, in fig. 2.8B we plot $|\chi|(F, f_s)$ for various driving amplitudes as a function of the relative detuning. Note that for driving amplitudes beyond the sensitive linear response regime, a plateau centered at $f_s = f_0$ of almost constant sensitivity emerges. As a consequence, for large driving amplitudes the tuning of the hair bundle is poorer than in linear response.

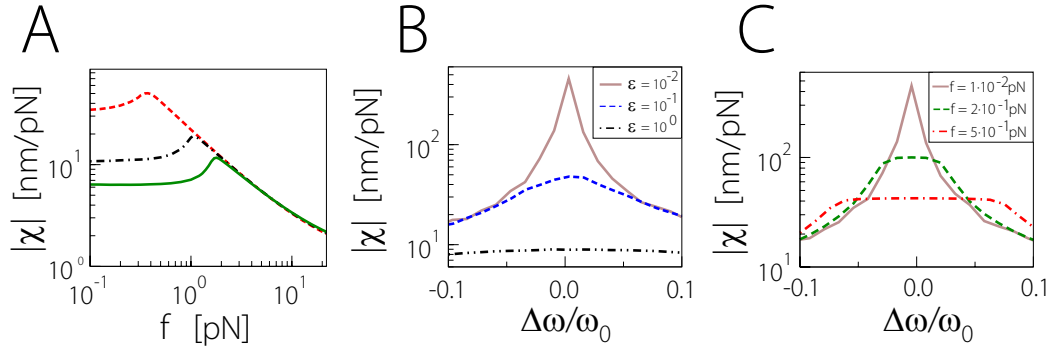


Figure 2.8: Response of the hair-bundle model at OP2 for detuned stimuli. (A) For $\epsilon = 0.01$, the sensitivity $|\chi|(F, f_s)$ is shown as a function of driving amplitude F for various choices of relative detuning $\Delta f/f_0$. (B) The linear response level for weak driving is plotted as a function of relative detuning for three different noise reduction factors as indicated. (C) For $\epsilon = 0.01$, we present the sensitivity as function of relative detuning for three different forcing amplitudes as indicated.

2.3 Local exponents of nonlinear compression

In section 1.2, we have introduced the concept of a local exponent of nonlinear compression. It was used to quantify the degree of nonlinear compression as observed in the response of the basilar membrane in dependence on the sound pressure level. In the case of the hair bundle a similar analysis can be performed. To this end, we define

$$\alpha = \frac{d \ln(|\chi|)}{d(\ln(F))}.$$

Note that the same symbol as in 1.2 is used, even though the respective quantities e.g. have different units. It will, however, be clear from the context which definition applies. By numerical differentiation, we have determined α for the data shown in fig. 2.5.

We will discuss OP1 first. In the limit of weak driving amplitudes, α is found to be close to 0, indicative of the linear behavior of the hair bundle in this regime. For intermediate driving amplitudes, α attains a noise dependent minimum. For the smallest noise intensity shown, this minimum is close to -1 . We will refer to a regime with $\alpha \gtrsim -1$ as a regime of strong nonlinear compression (SNC). For stronger driving amplitudes, a pronounced shoulder at $\alpha = -2/3$ hints at the proximity of OP1 to a supercritical Hopf bifurcation (cf. section 1.3). In the limit of strong driving, α again approaches 0, corresponding to the linear response regime for large driving amplitudes. In the case of OP2, no shoulder is found in the dependence of α upon driving amplitude. Being likewise 0 in linear response for weak stimuli, for intermediate driving amplitudes and weak noise strong nonlinear compression is found, i.e. α attains a minimum close to -1 . In the limit of large forces, as in the case of OP1, α approaches 0 again. Note that with decreasing noise reduction factor, a broadening is observed of the range of driving amplitudes over which strong

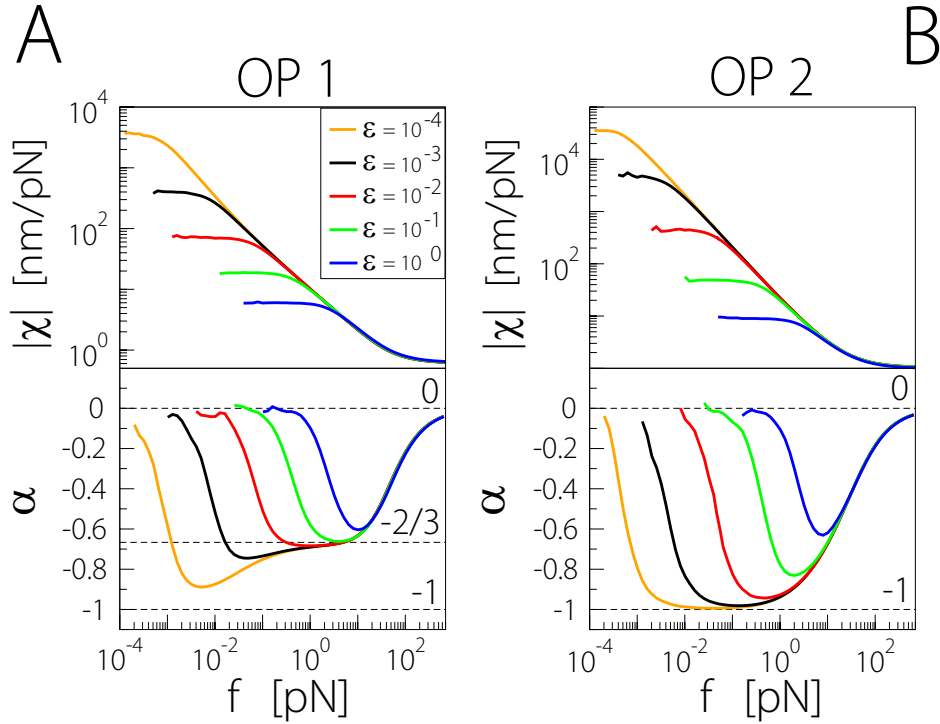


Figure 2.9: Local exponents of nonlinear compression for the hair-bundle model. In the upper panels, sensitivity at OP1 (in A) and OP2 (in B) as a function of driving amplitude is shown for various values of the noise reduction factor ε ; same data as presented in fig. 2.5. By numerical differentiation of these data we computed the local exponent α as a function of driving amplitude. OP1 is shown in A, lower panel. OP2 is shown in B, lower panel.

nonlinear compression in the response at OP2 is observed.

This finding is further illustrated in fig. 2.10. For OP2, we show α in a color plot as a function of driving amplitude F and noise reduction factor ε . Four different regimes can be distinguished. In the limit of strong driving, the hair bundle behaves linear (LR). For weaker forces, the hair bundle's response exhibits nonlinear compression. In the case of the largest noise reduction factors shown, for still weaker driving amplitudes, a direct crossover to the the hair bundle's sensitive linear response regime is found. For small noise reduction factors, however, this linear response regime is shifted towards smaller and smaller driving amplitudes. At the same time a regime of strong nonlinear compression extends over a larger and larger range of driving amplitudes.

2.4 Summary

In this chapter, we have investigated the noise-imposed limits of hair-bundle performance. For this purpose, we have introduced the noise reduction factor ε . It was

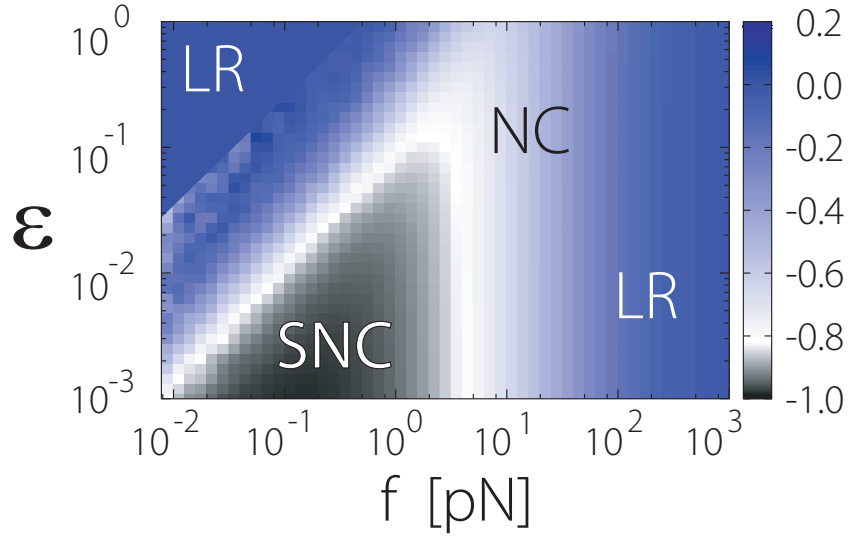


Figure 2.10: The different regimes of nonlinear compression for the hair-bundle model at OP2. A color plot of the local exponent of nonlinear compression α is shown as a function of driving amplitude F and noise reduction factor ε . We indicate the two regimes of linear response (LR), the regime of nonlinear compression (NC), and the regime of strong nonlinear compression (SNC). Note that for decreasing noise reduction factors, the regime of strong nonlinear compression extends to smaller and smaller driving amplitudes.

employed to artificially reduce the strength of noise terms within the biophysical description of hair-bundle dynamics that was introduced in the last chapter. Most importantly, for two operations points, OP1 and OP2, we have shown that the quality of spontaneous oscillations, as well as the amplification gain of an isolated hair bundle is expected to depend in an almost linear fashion on the level of intrinsic fluctuations. We have also discussed the response of the hair bundle in terms of the local exponent of nonlinear compression α . Upon noise reduction, values of α close to -1 can be attained for weak driving forces, corresponding to an even higher degree of nonlinear compression as expected for a critical oscillator operating at a supercritical Hopf bifurcation ($\alpha = -2/3$). In the next chapter, we will discuss results concerning the spontaneous and driven dynamics of the noisy phase and Hopf oscillator, i.e. two generic oscillator systems. These findings will further elucidate the observations reported here.

Chapter 3

Limit-cycle dynamics in the presence of fluctuations

In the last chapter, we have shown that a reduction of intrinsic fluctuations is expected to enhance the phase coherence and sensitivity of oscillatory hair bundles. For the parameter sets chosen, the (noiseless) hair bundle resides in the vicinity of a supercritical (OP1) respectively subcritical (OP2) Hopf bifurcation. As detailed below, the dynamics of any deterministic system operating close to this type of oscillatory instability can be transformed into the so-called normal form of the bifurcation. While specifics of the system's behavior are not preserved by this transformation, generic aspects of its dynamics are expected to be well reflected in the dynamics as defined by the normal form. In this chapter, we will therefore analyze the effects of noise on the dynamics of two generic oscillatory systems, namely the noisy phase oscillator and the noisy Hopf oscillator. While sharing many of the noise related dynamical features observed for the hair-bundle oscillator, for these systems an analytical treatment is possible.

To this end, we first review the concept of the Hopf bifurcation and the Hopf normal form in more detail. We then turn to the noisy phase oscillator as a limiting case. In particular, we discuss how phase diffusion is shaping the spectral statistics and the response behavior of the oscillator. A generalization of these results then leads to an analytic expression for the full nonlinear response function of the noisy Hopf oscillator. This response is further analyzed with regard to its regimes of nonlinear compression.

3.1 Dynamics close to a Hopf bifurcation

Consider a dynamical system that is governed by a control parameter r . Furthermore, assume there is a value r_c and a fixed point of the system that is stable whenever $r > r_c$, but unstable for choices $r_c < r$. We say that at $r = r_c$ a bifurcation occurs. More specifically, if for $r = r_c$ two complex conjugate eigenvalues of the Jacobian, evaluated at the fixed point of the system, simultaneously cross the

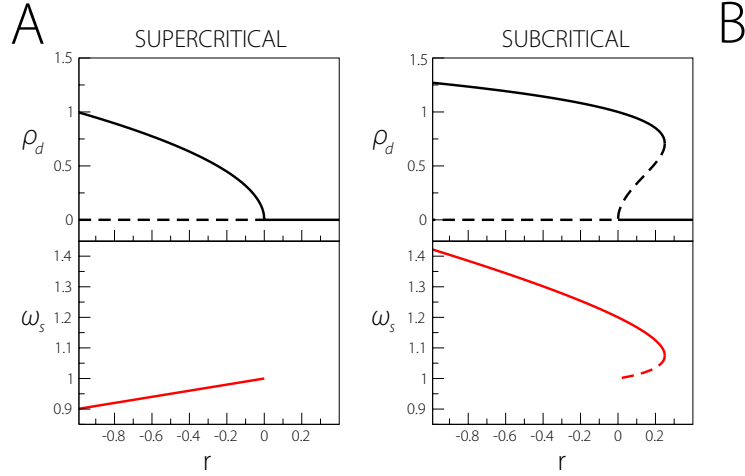


Figure 3.1: Dynamics close to a Hopf bifurcation. The radius $\hat{\rho}$ (top) and the frequency ω_s (bottom) of periodic solutions $z(t) = \hat{\rho}e^{-i\omega_s t}$ of the Hopf normal form are shown as a function of the control parameter r . Panel (A) corresponds to the supercritical case with $\omega_0 = 1, b = 1, b' = 0.1, c = c' = 0$. In (B) the subcritical case with $\omega_0 = 1, b = -1, b' = 0.1, c = 1, c' = 0.1$ is shown. Stable solutions are plotted as solid lines, unstable solutions as dashed lines. Also note that ω_s is shown only for solutions with $\hat{\rho} > 0$. When $\hat{\rho} = 0$ a frequency of oscillation is only well defined in the case the system is right at the bifurcation.

imaginary axis, i.e. are purely imaginary, the system undergoes a so-called Hopf bifurcation. This type of local bifurcation comes in two variants, the super- and the subcritical case. It can be shown that the main dynamical features of any system in the vicinity of a Hopf bifurcation can be described by the so-called normal form of the bifurcation [175]. It reads

$$\dot{z} = -(r + i\omega_0)z - (b + ib')|z|^2z - (c + ic')|z|^4z, \quad (3.1)$$

where $z = \rho e^{-i\phi}$ is a complex variable and $r, \omega_0, b, b', c, c'$ are real. A transformation of eq. (3.6) to polar coordinates yields

$$\dot{\rho} = -r\rho - b\rho^3 - c\rho^5, \quad (3.2)$$

$$\dot{\phi} = \omega_0 + b'\rho^2 + c'\rho^4. \quad (3.3)$$

This system has $z(t) = 0$ as a fixed point solution. It is stable for $r > 0$. The Hopf bifurcation occurs at $r_c = 0$.

The case $b > 0$ corresponds to the supercritical bifurcation (see fig. 3.1A). When dealing with the latter, we will always assume $c = c' = 0$. For $r < 0$, a stable limit cycle exists with $z(t) = \hat{\rho}e^{-i\omega_s t}$, where

$$\hat{\rho} = \sqrt{-r/b} \quad \text{and} \quad \omega_s = \omega_0 - \frac{b'}{b}r. \quad (3.4)$$

Here $\hat{\rho}$ is the solution of eq. (3.2) with the left hand side set to zero. Knowing $\hat{\rho}$, it is possible to determine ω_s from eq. (3.3) by noting that $\omega_s = \dot{\phi}$. Also, as the

derivative with respect to ρ of the right hand side of eq. (3.2) evaluates to $2r < 0$, this limit cycle according to linear stability analysis is stable [156].

For a choice $b < 0$, the bifurcation is subcritical. For $r > 0$, there exists a limit cycle $z(t) = \hat{\rho}e^{-i\omega_s t}$ with $\hat{\rho}$ and ω_s as defined above. In this case $2r > 0$, implying that it is unstable. At $r = 0$, its radius $\hat{\rho}$ shrinks to zero and the fixed point $z(t) = 0$ loses its stability. In the subcritical case, if the higher nonlinearity is included in a stabilizing way by choosing $c > 0$ (see fig. 3.1B), for values of r with $0 < r < b^2/4c$ two oscillatory solutions exist with

$$\hat{\rho}_{1,2} = \sqrt{-\frac{b}{2c} \pm \sqrt{\frac{b^2}{4c^2} - \frac{r}{c}}}. \quad (3.5)$$

The respective values of ω_s can again be calculated from eq. (3.3). As the resulting formula is lengthy we omit it here. The solution corresponding to $\hat{\rho}_2$ shrinks to zero amplitude when $r = 0$. Again, linear stability analysis can be used to show that it is unstable. The solution corresponding to $\hat{\rho}_2$ on the other hand is stable. It also exists for $r < 0$.

The system described by the Hopf normal form will in the following be simply referred to as the Hopf oscillator. We will always assume $c > 0$ when dealing with the subcritical variant of the Hopf oscillator. Also, we will say the Hopf oscillator is on the oscillatory side of the Hopf bifurcation whenever $r < 0$.

In particular, we will analyze the response of the noisy Hopf oscillator to an external driving. In particular a periodic driving with a single frequency of the form $F(t) = fe^{-i\omega t}$ will be considered. Without loss of generality, f will be chosen to be real. Noise will also be included into the description. The system under consideration is thus

$$\dot{z} = -(r + i\omega_0)z - (b + ib')|z|^2z - (c + ic')|z|^4z + fe^{-i\omega t} + \sqrt{2\varepsilon}\xi(t), \quad (3.6)$$

where $\xi(t)$ is assumed to be a complex-valued white Gaussian noise with $\langle \xi(t)\xi^*(t + \tau) \rangle = 2\delta(\tau)$ and $\langle \xi(t)\xi(t + \tau) \rangle = 0$. In the following, we will mostly work with the equivalent formulation of eq. (3.6) in polar coordinates

$$\dot{\rho} = -r\rho - b\rho^3 - c\rho^5 + f \cos(\phi - \omega t) + \sqrt{2\varepsilon}\xi_1(t) \quad (3.7)$$

$$\dot{\phi} = \omega_0 + b'\rho^2 + c'\rho^4 - \frac{f}{\rho} \sin(\phi - \omega t) + \sqrt{\frac{2\varepsilon}{\rho^2}}\xi_2(t). \quad (3.8)$$

Here ξ_1 and ξ_2 are independent white Gaussian noises with $\langle \xi_i(t)\xi_j(t + \tau) \rangle = \delta(\tau)\delta_{ij}$, where δ_{ij} denotes the Kronecker delta. In fig. 3.2, sample trajectories of the noisy Hopf oscillator are shown for $f = 0$.

Upon driving, i.e. for $f \neq 0$, the time-dependent average $\langle z(t) \rangle$ of a stochastic dynamical system such as the Hopf oscillator will be a periodic function with period $2\pi/\omega$. We can express this time-dependent average by means of a Fourier series as

$$\langle z(t) \rangle = \sum z_n e^{-in\omega t}.$$

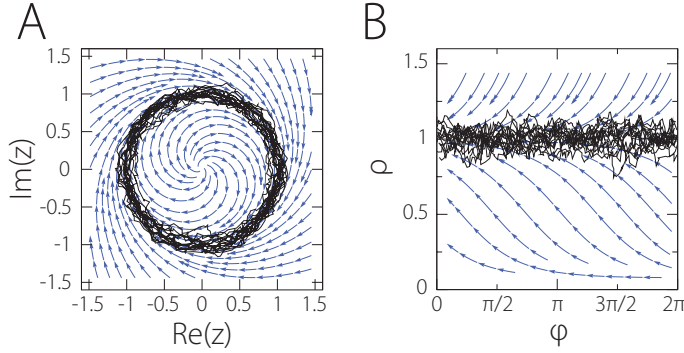


Figure 3.2: Sample trajectories of the noisy Hopf oscillator ($r = -1$, $\omega_0 = 1$, $b = b' = 1$, $c = c' = 0$, $\varepsilon = 0.1$, $f = 0$). (A) In cartesian coordinates the zigzagging movement of the oscillator along an approximately circular path around the origin is visible (black line). Also shown are streamlines (blue lines with arrow heads) of the noiseless system ($\varepsilon = 0$). These clearly delineate the stable limit cycle of the deterministic system. (B) The same trajectory (black line) is plotted in polar coordinates. Streamlines of the noiseless system are again included (blue lines with arrow heads).

The response of the system can then be discussed in terms of the sensitivity $|\chi|(f, \omega)$ defined as

$$|\chi|(f, \omega) = \frac{|z_1|}{f}. \quad (3.9)$$

3.2 Phase diffusion and partial entrainment

The dynamics of the Hopf oscillator as given by eq. (3.7) and eq. (3.8) are composed of the time evolution of a noisy amplitude and that of a noisy phase. In general both shape the statistics of noisy limit cycle oscillations and the response to an external driving. Before dealing with this full set of equations, in this section we will discuss a certain limiting situation. The partly well-known results presented in this section [126], while also being of interest in their own right, will be of use in the remainder of this chapter.

More specifically, we will neglect any amplitude dynamics, i.e. set $\rho(t) \equiv \rho_0 > 0$. Furthermore, we will assume $b' = c' = 0$. Note, however, that the corresponding terms in eq. (3.8) could be eliminated by a rescaling of the frequency ω_0 since ρ is assumed to be constant. We thus consider the dynamics of a complex variable $z(t) = \rho_0 e^{-i\phi(t)}$ described by

$$\dot{\phi} = \omega_0 - \hat{f} \sin(\phi - \omega t) + \sqrt{2\hat{\varepsilon}}\xi(t), \quad (3.10)$$

where we have introduced the shorthand $\hat{f} = f/\rho_0$ and $\hat{\varepsilon} = \varepsilon/\rho_0^2$. Such a dynamical system in the literature is known as a noisy phase oscillator, as its dynamics is captured by a single equation for its phase. Being confined to a circle of radius

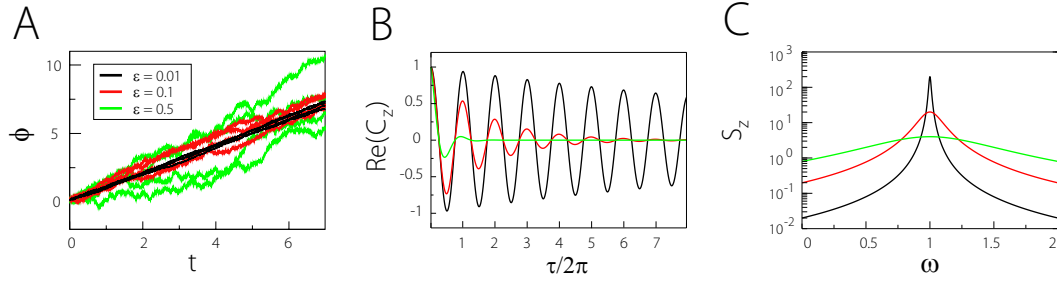


Figure 3.3: Phase diffusion in the noisy phase oscillator ($\omega_0 = 1$, $\rho_0 = 1$, $f = 0$). (A) Several traces of the phase $\phi(t)$ are shown for three different noise intensities. All traces have identical initial conditions. On average, $\phi(t)$ grows as $\omega_0 t$. Increasing the noise strength leads to more pronounced phase diffusion. (B) We plot the real part of the complex autocorrelation function of the three oscillators shown in (A) (legend in (A)). While the oscillation frequency in all three cases is ω_0 , the decay rate of correlations increases with increasing noise intensity. Quality factors corresponding to the three noise intensities are: $Q(\varepsilon = 0.01) = 50$, $Q(\varepsilon = 0.1) = 5$, $Q(\varepsilon = 0.5) = 1$. (C) The corresponding power spectral densities are all shifted Lorentzians with a peak at $\omega_0 = 1$, albeit with different half-widths corresponding to the varying quality factors (legend in (A)).

ρ_0 it revolves around the origin with an average frequency ω_0 (see fig. 3.3). Phase oscillators with and without noise constitute an important class of oscillators and have been widely studied for example in connection with synchronization phenomena in systems of coupled oscillators [176, 157, 126, 178, 4].

In order to study the spontaneous dynamics of the phase oscillator in the absence of an external driving, we will first assume $\hat{f} = 0$. The general solution of eq. (3.10) is then given by

$$\phi(t) = \phi(0) + \omega_0 t + \eta(t),$$

where

$$\eta(t) = \int_0^t \sqrt{2\hat{\varepsilon}} \xi(t) dt$$

is a Wiener process. The above choice of $\xi(t)$ thus ensures that $\eta(t)$ is normally distributed with zero mean and a variance that grows proportional to t . The probability density $p_t(\eta)$ describing the distribution of $\eta(t)$ for a given time t is given by

$$p_t(\eta) = \frac{1}{\sqrt{4\pi\hat{\varepsilon}t}} e^{-\frac{1}{2} \frac{\eta^2}{2\hat{\varepsilon}t}}.$$

This means that in addition to the deterministic growth of the phase, which is tuned by ω_0 , noise leads to so-called phase diffusion. Trajectories that are started with identical initial conditions, over the course of time will move apart from each other (see fig. 3.3A). This dephasing effect of the noise can be further analyzed in terms of the autocorrelation function and the power spectrum (for definitions see section 2.1 and note that here we use radial frequency). For the autocorrelation function

we find for $\tau \geq 0$

$$\begin{aligned}
C_z(\tau) &= \langle z(t)z^*(t+\tau) \rangle - \langle z(t) \rangle \langle z^*(t+\tau) \rangle = \langle \rho_0 e^{-i\phi(t)} \rho_0 e^{i\phi(t+\tau)} \rangle \\
&= \rho_0^2 \langle e^{i(\phi(t)+\omega_0\tau+\eta(\tau)-\phi(t))} \rangle \\
&= \rho_0^2 e^{i\omega_0\tau} \langle e^{i\eta(\tau)} \rangle \\
&= \rho_0^2 e^{i\omega_0\tau} e^{-\hat{\varepsilon}\tau},
\end{aligned}$$

where in the last step we have used that

$$\int_{-\infty}^{\infty} e^{i\eta} p_\tau(\eta) d\eta = e^{-\hat{\varepsilon}\tau}.$$

Because of

$$C_z(\tau) = C_z^*(-\tau),$$

for arbitrary τ we find

$$C_z(\tau) = \rho_0^2 e^{i\omega_0\tau} e^{-\hat{\varepsilon}|\tau|}.$$

Knowing the autocorrelation function, the power spectrum can be calculated using the Wiener-Kinchine-theorem:

$$\begin{aligned}
S_z(\omega) &= \int_{-\infty}^{\infty} \rho_0^2 e^{i\omega_0\tau} e^{-\hat{\varepsilon}|\tau|} e^{-i\omega\tau} d\tau \\
&= \frac{2\varepsilon}{\varepsilon^2/\rho_0^4 + (\omega_0 - \omega)^2}.
\end{aligned}$$

The autocorrelation function corresponds to a damped oscillation with frequency ω_0 (see fig. 3.3B). Correlations decay with a correlation time

$$\tau_{corr} = 1/\hat{\varepsilon}.$$

In other words, due to phase diffusion the phase oscillator is performing a noisy oscillation with finite phase coherence. Correspondingly, the spectrum is not a delta peak at ω_0 , as would be the case in the absence of noise, but a shifted Lorentzian of finite width (see fig. 3.3C).

For the quality of the phase oscillator one finds

$$Q = \frac{\omega_0 \rho_0^2}{2\varepsilon}, \quad (3.11)$$

i.e. the quality of oscillations is inversely proportional to the noise strength ε . Note the similarity with the results obtained in section 2.1.

We now turn to the response of the noisy phase oscillator. To this end, it is useful to introduce a new variable $\psi(t) = \phi(t) - \omega t$ that measures the of the oscillator in a coordinate system corotating with the external stimulus. Insertion into eq. (3.10) yields

$$\dot{\psi} = \Delta\omega - \hat{f} \sin \psi + \sqrt{2\varepsilon} \xi(t), \quad (3.12)$$

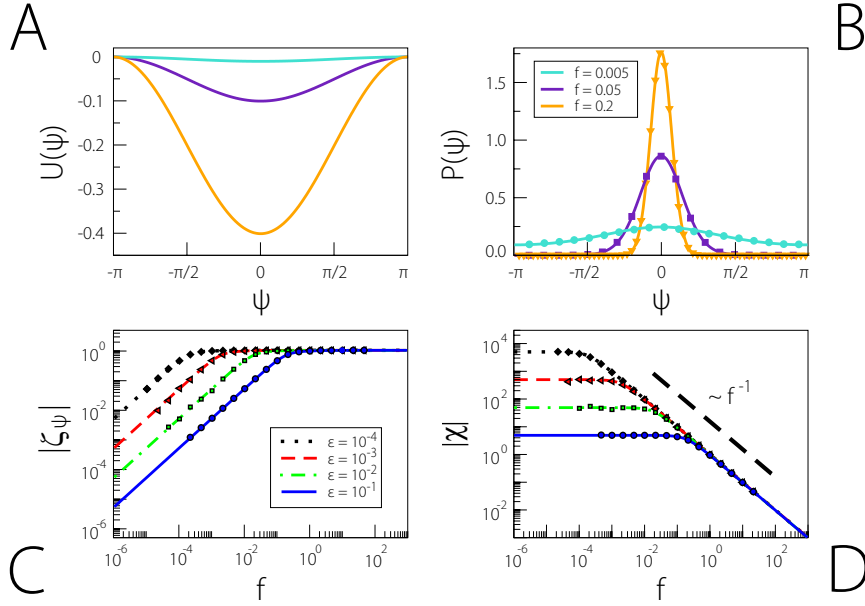


Figure 3.4: Response of the noisy phase oscillator for a tuned stimulus ($\Delta\omega = 0$, $\omega_0 = 1$, $\rho_0 = 1$). (A) One period of the potential $U(\psi)$ for three different driving forces (legend in (B)). (B) Distribution of phases $P(\psi)$ for noise intensity $\varepsilon = 0.01$ corresponding to the same driving amplitudes as in (A). (C) ζ_ψ as a function of driving amplitude f for four different noise intensities. (D) Sensitivity $|\chi|$ as a function of driving amplitude f for the same noise intensities as in (C) (legend in (C)). In all panels, analytical results are shown as lines, symbols indicate the results of stochastic simulations.

where we have introduced $\Delta\omega = \omega_0 - \omega$ as shorthand for the detuning or frequency mismatch of the external stimulus with respect to the free running frequency of the oscillator. The dynamics of ψ can be pictured as the diffusive motion of an overdamped particle in a potential landscape $U(\psi)$ driven by white noise, where

$$U(\psi) = -\Delta\omega\psi - \hat{f}\cos\psi.$$

While for a tuned stimulus, i.e. $\Delta\omega = 0$, this potential is symmetric with respect to its minimum at $\psi = 0$ (see fig. 3.4A), a finite detuning $\Delta\omega \neq 0$ introduces a tilt (see fig. 3.5A). Note that $U(\psi)$ is independent of time. By solving for the steady-state solution of the Fokker-Planck equation corresponding to eq. (3.12), one can calculate the stationary distribution $P(\psi)$ of phases in the corotating reference frame [153] (see fig. 3.4B and fig. 3.5B). It reads

$$P(\psi) = \frac{1}{N} e^{\frac{\Delta\omega}{\varepsilon}\psi + \frac{\hat{f}}{\varepsilon}\cos\psi} \int_{\psi}^{\psi+2\pi} e^{-\frac{\Delta\omega}{\varepsilon}\zeta - \frac{\hat{f}}{\varepsilon}\cos\zeta} d\zeta,$$

where N is a normalization constant given by

$$N = 4\pi^2 e^{-\pi\frac{\Delta\omega}{\varepsilon}} I_{i\frac{\Delta\omega}{\varepsilon}} \left(\frac{\hat{f}}{\varepsilon} \right) I_{-i\frac{\Delta\omega}{\varepsilon}} \left(\frac{\hat{f}}{\varepsilon} \right).$$

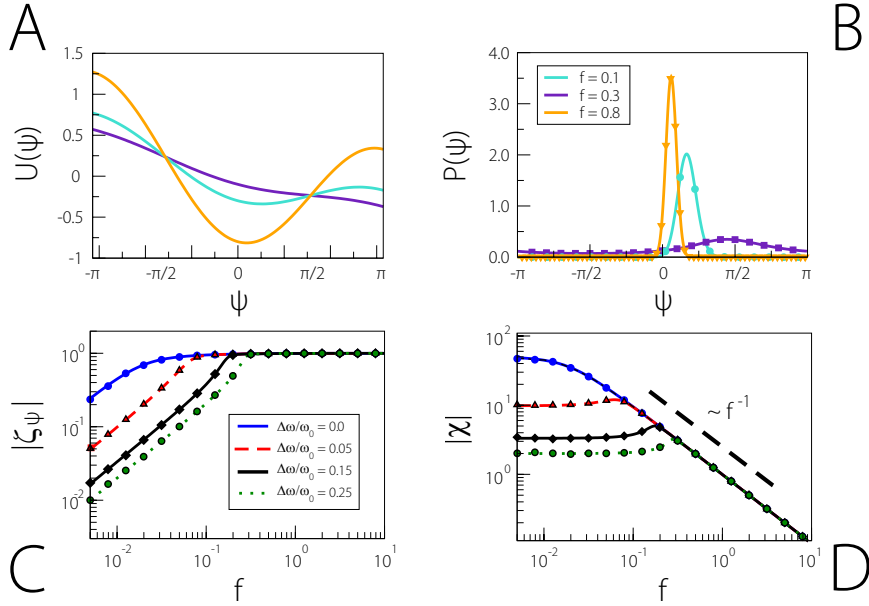


Figure 3.5: Response of the noisy phase oscillator for a detuned stimulus ($\Delta\omega \neq 0$, $\omega_0 = 1$, $\rho_0 = 1$, $\varepsilon = 0.01$). (A) One period of the tilted potential $U(\psi)$ for $\Delta\omega = 0.15$ and three different driving amplitudes (legend in (B)). (B) Distribution of phases $P(\psi)$ corresponding to the same driving amplitudes and detuning as in (A). (C) ζ_ψ as a function of driving amplitude f for four different values of relative detuning $\Delta\omega/\omega_0$. (D) Sensitivity $|\chi|$ as a function of f for the same relative detuning as in (C) (legend in (C)). In all panels, analytical results are shown as lines, symbols indicate the results of stochastic simulations.

Here $I_a(\dots)$ denotes the modified Bessel function of the first kind of possibly complex order a . In order to calculate the sensitivity of the phase oscillator, note that

$$\langle z(t) \rangle = \langle \rho_0 e^{-i\phi(t)} \rangle = \rho_0 \langle e^{-i(\psi(t) + \omega t)} \rangle = \rho_0 \langle e^{-i\psi(t)} \rangle e^{-i\omega t}. \quad (3.13)$$

We introduce the notation

$$\zeta_\psi = \langle e^{-i\psi(t)} \rangle.$$

Since $P(\psi)$ is independent of time, so is ζ_ψ . Note that ζ_ψ coincides with the value of the characteristic function $\phi(s) = \langle e^{is\psi} \rangle$ of the random variable ψ evaluated at $s = -1$ [49]. The modulus of ζ_ψ can be viewed as a measure for the degree of phase locking or entrainment of the oscillator to the external stimulus. No entrainment means that ψ is uniformly distributed in the interval $[-\pi, \pi]$, implying $|\zeta_\psi| = 0$. A large degree of phase locking renders the distribution $P(\psi)$ sharply peaked, leading to $|\zeta_\psi| \lesssim 1$. Inspection of eq. (3.13) shows that

$$\rho_0 \zeta_\psi = z_1,$$

where z_1 is the fundamental mode of the Fourier expansion of $\langle z(t) \rangle$. Note that z_1 depends on f and $\Delta\omega$ as the distribution of phases ψ does (see fig. 3.4B and

fig. 3.5B). For the sensitivity $|\chi|$ as a function of the driving amplitude f and the detuning $\Delta\omega$ we thus find

$$|\chi|(f, \omega) = \frac{\rho_0}{f} |\zeta_\psi|.$$

Using the knowledge of $P(\psi)$, an explicit formula for ζ_ψ can be derived [60]:

$$\zeta_\psi = \frac{I_{1+i\Delta\omega\rho_0^2/\varepsilon}(f\rho_0/\varepsilon)}{I_{i\Delta\omega\rho_0^2/\varepsilon}(f\rho_0/\varepsilon)}. \quad (3.14)$$

The sensitivity is then given by

$$|\chi|(f, \omega) = \frac{\rho_0}{f} \left| \frac{I_{1+i\Delta\omega\rho_0^2/\varepsilon}(f\rho_0/\varepsilon)}{I_{i\Delta\omega\rho_0^2/\varepsilon}(f\rho_0/\varepsilon)} \right|.$$

The response of the noisy phase oscillator is marked by two distinct regimes. For small amplitudes f , the periodic driving leads to partial entrainment, as evidenced by the peaks emerging in the distribution $P(\psi)$ (see fig. 3.4B and fig. 3.5B). Accordingly, $|\zeta_\psi|$ is different from zero. For small amplitudes it increases almost linearly (see fig. 3.4C and fig. 3.5C). In this linear response regime, the sensitivity is constant (see fig. 3.4D and fig. 3.5D). For a tuned stimulus, i.e. $\Delta\omega = 0$, we can expand the Bessel functions appearing in the expression for $|\chi|$ as follows [3]:

$$I_0(f\rho_0/\varepsilon) = \sum_{k=0}^{\infty} \frac{\left(\frac{1}{4} \left(\frac{f\rho_0}{\varepsilon}\right)^2\right)^k}{k!\Gamma(k+2)} = 1 + O(f^3) \quad (3.15)$$

and

$$I_1(f\rho_0/\varepsilon) = \frac{f\rho_0}{2\varepsilon} \sum_{k=0}^{\infty} \frac{\left(\frac{1}{4} \left(\frac{f\rho_0}{\varepsilon}\right)^2\right)^k}{k!\Gamma(k+2)} = \frac{f\rho_0}{2\varepsilon} + O(f^3). \quad (3.16)$$

We therefore find

$$\lim_{f \rightarrow 0} |\chi|(f, \omega_0) = \frac{\rho_0^2}{2\varepsilon},$$

i.e. the linear response level of the phase oscillator in the tuned case is inversely proportional to the noise strength ε . Note the similarity with results obtained for the hair-bundle model upon noise reduction (see section 2.2). For a detuned stimulus, i.e. $\Delta\omega \neq 0$, sensitivity in linear response is significantly reduced (see fig. 3.5D). This is reflecting the fact that it is more difficult to entrain an oscillator to a frequency that is different from its own. In the limit of strong driving, however, phase locking for any $\Delta\omega$ is essentially complete, resulting in $|\zeta_\psi| \lesssim 1$. Therefore, the sensitivity for large forcing amplitudes is inversely proportional to f and reads

$$|\chi|(f, \omega) \lesssim \frac{\rho_0}{f}.$$

In this regime, the sensitivity thus decays according to a power law $|\chi| \sim f^\alpha$ with an exponent $\alpha = -1$ (see fig. 3.4D and fig. 3.5D).

3.3 Amplitude growth vs. phase locking

In the last section, we have discussed important statistics of the spontaneous and driven dynamics of the noisy phase oscillator. In this section, we will present results that extend the previous discussion to the noisy Hopf oscillator as defined by eq. (3.7) and eq. (3.8).

We will assume to be on the oscillatory side of the Hopf bifurcation, i.e. $r < 0$. Furthermore we will set $b' = c' = 0$. This choice ensures that ρ is not entering the deterministic part of the dynamic equation for ϕ . It still enters, however, via the multiplicative noise term. We will consider the supercritical ($b > 0, c = 0$), as well as the subcritical ($b < 0, c > 0$) case.

The Hopf oscillator is performing noisy limit cycle oscillations (see fig. 3.2). Due to phase diffusion and fluctuations of its amplitude, these are marked by a finite phase coherence. The power spectrum of the Hopf oscillator is well described by a shifted Lorentzian of the form

$$S_z(\omega) = \frac{4D}{K^2 + \Lambda^2(\hat{\omega}_0 - \omega)^2}, \quad (3.17)$$

where $\hat{\omega}_0$, K , D and Λ are determined by the parameters of the oscillator. For the supercritical Hopf oscillator ($b' = 0$) and small noise intensities, perturbation theory applied to the Fokker-Planck equation corresponding to eq. (3.7) and eq. (3.8) can be used to derive explicit formulae (see ref. [79]) for the parameters appearing in eq. (3.17):

$$\begin{aligned} \hat{\omega}_0 &= \omega_0, \\ K &= \frac{2db}{|r|}, \\ \Lambda &= 16 \frac{(2r^2 + db)r^2(9dbr^2 + 2r^4 + 12d^2b^2)}{(2r^2 + 3db)^2(54dbr^2 + 8r^4 + 15d^2b^2)}, \\ D &= d. \end{aligned}$$

Note that in the limit of vanishing noise, we recover the spectrum of the phase oscillator as given by eq. (3.11). In particular, the same dependence of the oscillations' quality on noise intensity is found. In this limit, the spectrum of the Hopf oscillator is thus predominantly shaped by phase diffusion. The phase oscillator in this sense can be viewed as a weak noise limit of the Hopf oscillator.

In order to determine the sensitivity of the Hopf oscillator to a periodic driving we transform eq. (3.7) and eq. (3.8) into a coordinate frame corotating with the periodic signal. We find

$$\dot{\rho} = -r\rho - b\rho^3 - c\rho^5 + f \cos(\psi) + \sqrt{2\varepsilon}\xi_1(t) \quad (3.18)$$

$$\dot{\psi} = \Delta\omega - \frac{f}{\rho} \sin(\psi) + \sqrt{\frac{2\varepsilon}{\rho^2}}\xi_2(t), \quad (3.19)$$

where $\psi(t) = \phi(t) - \omega t$ as introduced in the last section. We now write

$$\langle z(t) \rangle = \langle \rho(t) e^{-i\phi(t)} \rangle = \langle \rho(t) \rangle \langle e^{-i(\psi(t)+\omega t)} \rangle = \langle \rho(t) \rangle \zeta_\psi e^{-i\omega t}, \quad (3.20)$$

where in the second step we have assumed that averaging over the respective contributions of the amplitude $\rho(t)$ and phase $\phi(t)$ can be performed independently. In order to calculate $\langle \rho(t) \rangle$ and ζ_ψ , we further assume that $\rho(t)$ will only mildly fluctuate about a fixed value ρ_d , i.e. that $\langle \rho(t) \rangle \approx \rho_d$ and $\frac{d}{dt} \langle \rho(t) \rangle \approx 0$. Later in this section, we will see that for small to moderate noise intensities all assumptions made so far yield reasonable results. Inserting ρ_d into eq. (3.19) yields a dynamic equation for ψ that is the same as eq. (3.12) for the phase oscillator with $\rho_0 = \rho_d$. The distribution of ψ thus is independent of time and furthermore

$$\zeta_\psi = \frac{I_{1+i\Delta\omega\rho_d^2/\varepsilon}(f\rho_d/\varepsilon)}{I_{i\Delta\omega\rho_d^2/\varepsilon}(f\rho_d/\varepsilon)}. \quad (3.21)$$

Taking averages in eq. (3.7) shows that ρ_d for consistency has to fulfill

$$0 = -r\rho_d - b\rho_d^3 - c\rho_d^5 + f\text{Re}(\zeta_\psi), \quad (3.22)$$

where we have used that $\langle \cos \psi \rangle = \text{Re}(\zeta_\psi)$. By selfconsistently solving eq. (3.21) and eq. (3.22), the sensitivity of the Hopf oscillator can be calculated:

$$|\chi|(f, \omega) = \frac{\rho_d(f)}{f} \left| \frac{I_{1+i\Delta\omega\rho_d(f)^2/\varepsilon}(f\rho_d(f)/\varepsilon)}{I_{i\Delta\omega\rho_d(f)^2/\varepsilon}(f\rho_d(f)/\varepsilon)} \right|. \quad (3.23)$$

In general, a solution of eq. (3.21) and eq. (3.22) for given f and $\Delta\omega$ needs to be sought for numerically. Some limiting cases, however, can be analyzed explicitly. In the limit of vanishing driving amplitude, the oscillator will be only very weakly phase locked to the external signal, i.e. ψ will be distributed almost uniformly in the interval $[-\pi, \pi]$. More specifically

$$\lim_{f \rightarrow 0} \zeta_\psi = 0,$$

as is also apparent from fig. 3.6A and B. Consequently, for the corresponding solution of eq. (3.22) we find

$$\lim_{f \rightarrow 0} \rho_d(f) = \hat{\rho},$$

where $\hat{\rho}$ is given by eq. (3.4) in the supercritical and eq. (3.5) in the subcritical case, respectively. Applying the expansions given in eq. (3.15) and eq. (3.16) then yields

$$\lim_{f \rightarrow 0} |\chi|(f, \omega_0) = \frac{\hat{\rho}}{2\varepsilon}. \quad (3.24)$$

Thus, the sensitivity of the Hopf oscillator in linear response is inversely proportional to the noise intensity ε . This linear response level is the same as for the phase

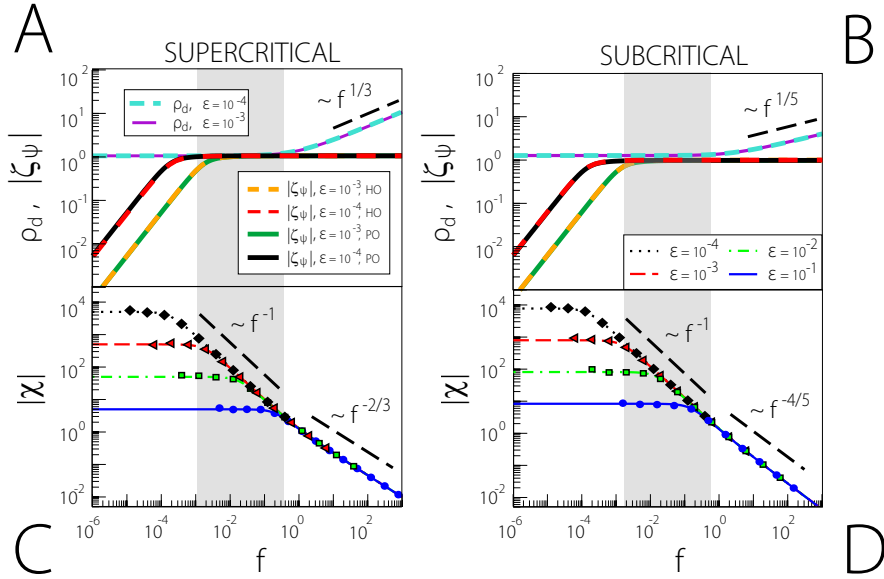


Figure 3.6: Response of the supercritical ((A), $b = 1$, $c = 0$, $r = -1$) and subcritical ((B), $b = -1$, $c = 1$, $r = -1$) Hopf oscillator to a tuned stimulus ($\omega_0 = \omega = 1$). (Top) The amplitude ρ_d according to eq. (3.22) is shown for two noise strengths as a function of driving amplitude. For the same noise intensities ζ_ψ is plotted as a function of input amplitude for the Hopf oscillator (HO) as given by eq. (3.21) and for the phase oscillator (PO) with $\rho_0 = \hat{\rho}$ as given by eq. (3.14) (legend in (A), top). (Bottom) $|\chi|$ is shown as a function of driving amplitude for four different noise intensities (legend in (B), top). Dashed lines correspond to powerlaws with exponents as indicated. Analytical results are shown as (dashed) lines, symbols indicate the results of stochastic simulations.

oscillator with $\rho_0 = \hat{\rho}$. Indeed, their respective degree of entrainment as measured by ζ_ψ over the whole range of driving amplitudes is virtually identical (see fig. 3.6A and B). While the amplitude of the phase oscillator is fixed to ρ_0 , the Hopf oscillator with increasing driving amplitude is more and more driven away from the origin. To see this, note that in the case of a strong driving phase locking will be almost complete, such that $\langle \cos(\psi) \rangle = \zeta_\psi \lesssim 1$ (see fig. 3.6B and C). In particular, note that ζ_ψ for tuned stimuli is purely real. The equation for $\rho_d(f)$ thus turns into

$$0 = -r\rho_d - b\rho_d^3 - c\rho_d^5 + f. \quad (3.25)$$

This implies that in the limit of strong forcing $\rho_d \sim f^{1/3}$ in the supercritical and $\rho_d \sim f^{1/5}$ in the subcritical case (see fig. 3.6A and B). For large forces the sensitivity thus decays according to a power law $|\chi| \sim f^\alpha$ with $\alpha = -2/3$ in the supercritical and $\alpha = -4/5$ in the subcritical case. The force dependent mean amplitude $\langle \rho(t) \rangle$ is almost independent of noise strength (see fig. 3.6A and B). While noise thus critically shapes the oscillator's response for small driving amplitudes (see eq. (3.24)), for large forcing amplitudes, where the effect of amplitude growth dominates, noise is less influential. The shaded regions in fig. 3.6 mark a response regime for intermediate driving amplitudes. In the case of small noise intensities, phase locking is almost

complete, i.e. $\zeta_\psi \lesssim 1$, but $\langle \rho(t) \rangle$ is close to its value in the absence of a stimulus, i.e. $\rho_d(f) \gtrsim \hat{\rho}$. The sensitivity therefore is approximately given by $|\chi(f, 0)| \approx \hat{\rho}/f$, corresponding to a power law decay with $\alpha = -1$. Note that for the largest noise intensity shown, this regime does not exist. In the next section, we will further analyze the different regimes in terms of the local exponent of nonlinear compression.

In the case of a finite frequency mismatch, i.e. $\Delta\omega \neq 0$, sensitivity in linear response is greatly reduced (see fig. 3.7A). For large driving amplitudes, however, phase locking also in the case of detuned stimuli is almost complete and $|\chi|$ hence decays according to the same power laws as for tuned stimuli (see fig. 3.7A). Plotting the linear response level as a function of detuning for small noise intensities, a sharp peak at $\Delta\omega = 0$ is found (see fig. 3.7B). For increasing noise intensities, this peak gets broader due to a reduction of the sensitivity for tuned stimuli. The sensitivity of the oscillator for stimuli with a large frequency mismatch is less strongly influenced by a change in the noise intensity. Noise therefore renders the Hopf oscillator's response less tuned. When showing $|\chi|$ as a function of frequency mismatch for fixed driving amplitude, plateaus of almost equal sensitivity centered at $\Delta\omega = 0$ can be distinguished (see fig. 3.7C). These can be understood by reference to the potential $U(\psi)$ that was introduced in the last section. Note, however, that in the definition of $U(\psi)$ the fixed amplitude ρ_0 needs to be substituted by $\rho_d(f)$. For input amplitudes $f > \Delta\omega\rho_d(f)$ the potential $U(\psi)$ has a minimum. If noise is small, the oscillator's phase relative to the phase of the driving will be trapped in this minimum. In other words, given a driving force f , the oscillator will be strongly phase-locked to the external signal for a range of frequency mismatches $\Delta\omega \in [-f/\hat{\rho}, f/\hat{\rho}]$. Note that as an approximation, we have substituted $\rho_d(f)$, which depends on the driving amplitude as well as the detuning $\Delta\omega$, by $\hat{\rho}$. When plotting the boundaries of this range as a function of driving amplitude f , one finds a triangular region in the f - $\Delta\omega$ -plane, a so-called Arnold tongue [126]. For the driving forces shown in fig. 3.7C, one finds $\rho_d(f) \approx \hat{\rho}$ and thus: $|\chi|(f, \omega) \approx \hat{\rho}/f$.

3.4 Local exponents of nonlinear compression

In the last section, we have shown how to calculate the sensitivity of the noisy Hopf oscillator. As a function of driving amplitude, three different response regimes could be distinguished. In this section, these will be further characterized. To this end, we remind the reader of the definition of the local exponent of nonlinear compression α (see section 1.2 and 2.3) which in the notation of this chapter for the Hopf oscillator is given by

$$\alpha = \frac{d \ln(|\chi|)}{d(\ln(f))}.$$

In the case of a tuned stimulus, i.e. $\Delta\omega = 0$, it is possible to calculate α explicitly. To this end note that in the latter case the ratio of Bessel functions appearing in eq. (3.23) is real and positive, implying that the absolute value signs can be omitted.

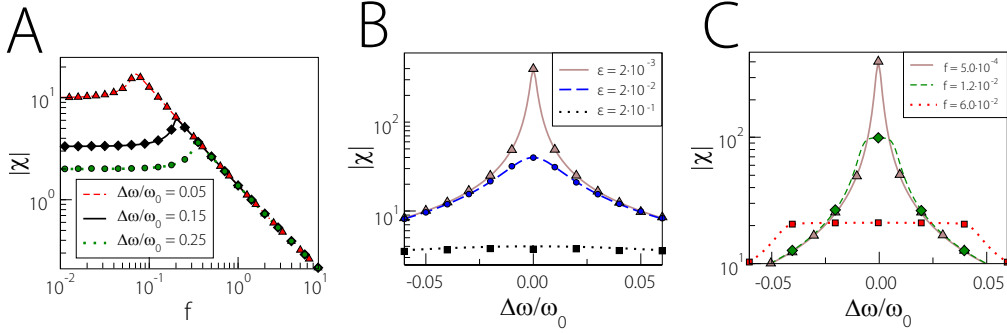


Figure 3.7: Response of the subcritical Hopf oscillator for a finite frequency mismatch ($\omega_0 = 1$, $r = -1$, $b = -1$, $c = 1$). the sensitivity $|\chi|(f, \omega)$ is shown in (A) as a function of driving amplitude for three values of relative detuning as indicated, and in (B) as a function of relative detuning for three different noise intensities, and in (C) as a function of relative detuning for three different driving amplitudes. The noise strength in (A) and (B) is $\varepsilon = 0.002$.

One finds that

$$\alpha = \frac{d \ln(|\chi|(e^{\ln(f)}, \omega_0))}{d \ln(f)} = \frac{d \ln(|\chi|(e^x, \omega_0))}{dx} \Big|_{x=\ln(f)} \quad (3.26)$$

$$= \left(\frac{d}{dx} \ln \left(\frac{\rho_d(e^x)}{e^x} \right) + \frac{d}{dx} \ln \left(\frac{I_1(\rho_d(e^x)e^x/\varepsilon)}{I_0(\rho_d(e^x)e^x/\varepsilon)} \right) \right) \Big|_{x=\ln(f)} \quad (3.27)$$

$$= f \frac{\rho_f + \rho'_d f}{\varepsilon} \left(\frac{I_0(f \rho_d/\varepsilon)}{I_1(f \rho_d/\varepsilon)} - \frac{I_1(f \rho_d/\varepsilon)}{I_0(f \rho_d/\varepsilon)} \right) - 2, \quad (3.28)$$

where $\rho'_d = d\rho_d/df$ and in the second step we have used that [3]

$$\frac{d}{dy} I_0(y) = I_1(y)$$

and

$$\frac{d}{dy} I_1(y) = I_0(y) - \frac{1}{y} I_1(y).$$

Using the expansions given in eq. (3.15) and eq. (3.16), it is possible to show that the difference of fractions of Bessel functions in eq. (3.26) will tend to $2\varepsilon/(\rho_d f)$, given that $\rho f \ll \varepsilon$. As ρ'_d in the limit of small f is bounded, we find $\lim_{f \rightarrow 0} \alpha = 0$, i.e. in linear response the sensitivity, indeed, is constant.

In order to calculate the limit of large forcing, note that using expansions for large arguments for the Bessel functions appearing in eq. (3.26), one can show that the difference of fractions of Bessel functions approaches $\varepsilon/(\rho_d f)$, given that $\rho_d f \gg \varepsilon$. Hence, in this regime we find

$$\alpha \simeq f \rho'_d / \rho_d - 1, \quad (3.29)$$

such that the exponent α depends on the asymptotics of $\rho_d(f)$. In this limit, due to the almost perfect phase locking of the oscillator, ρ_d is determined by eq. (3.25).

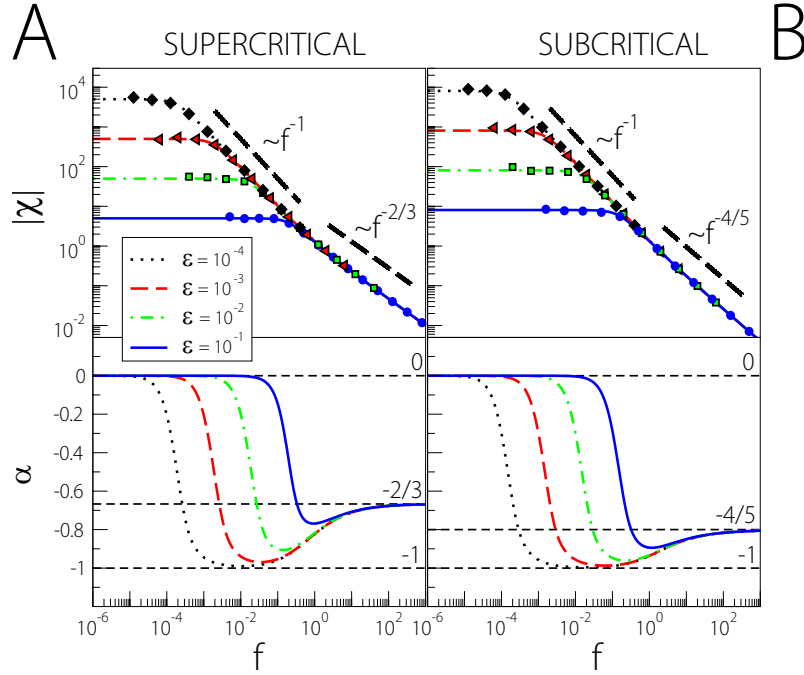


Figure 3.8: Sensitivity (top) $|\chi|(f, \omega)$ and local exponents of nonlinear compression α (bottom) vs input amplitude for the noisy Hopf oscillator. We show data for the Hopf oscillator ($r = -1, \omega = \omega_0 = 1$) for the supercritical (in (A) with $b = 1, c = 0$) and subcritical case (in (B) with $b = -1, c = 1$); simulations (symbols) compared to theory (eq. (3.23) and eq. (3.26), lines). Selected exponents (0, $-2/3$, $-4/5$, and -1) are indicated.

This yields $\rho_d \sim f^{1/3}$ and hence $\alpha = -2/3$ in the supercritical case (see fig. 3.8A), while $\rho_d \sim f^{1/5}$ and thus $\alpha = -4/5$ in the subcritical case (see fig. 3.8B).

Above we have shown that the response of the Hopf oscillator can exhibit strong nonlinear compression with $\alpha \gtrsim -1$. What exactly are the conditions that need to be met, in order for such a regime to exist? To this end, note that α according to eq. (3.29) will be close to -1 whenever $f\rho'_d \ll \rho_d$. As eq. (3.29) is valid whenever $\varepsilon/\rho_d \ll f$, we can formulate the following statement:

$$\varepsilon/\rho_d \ll f \ll \rho_d/\rho'_d \quad \rightsquigarrow \quad \alpha \gtrsim -1 \quad (3.30)$$

By taking the derivative with respect to f on both sides of eq. (3.25), the magnitude ρ'_d can be expressed in terms of ρ_d as $\rho'_d = 1/(r + 3B\rho_d^2 + 5c\rho_d^4)$. Hence, the right hand side of eq. (3.30) can be written as

$$\varepsilon/\rho_d \ll f \ll \rho_d(r + 3b\rho_d^2 + 5c\rho_d^4). \quad (3.31)$$

We remind the reader that $\rho_d(0) = \hat{\rho}$. For a tuned stimulus, due to the symmetry of the density $P(\psi)$ with respect to its peak at $\psi = 0$, one has $\text{Re}(z_\psi) = z_\psi > 0$. As $r\rho + b\rho^3 + c\rho^5 < 0$ whenever $\rho < \hat{\rho}$, eq. (3.22) implies, that $\hat{\rho} \leq \rho_d(f)$ for all driving amplitudes. Therefore, a regime of strong nonlinear compression, i.e. with $\alpha \gtrsim -1$,

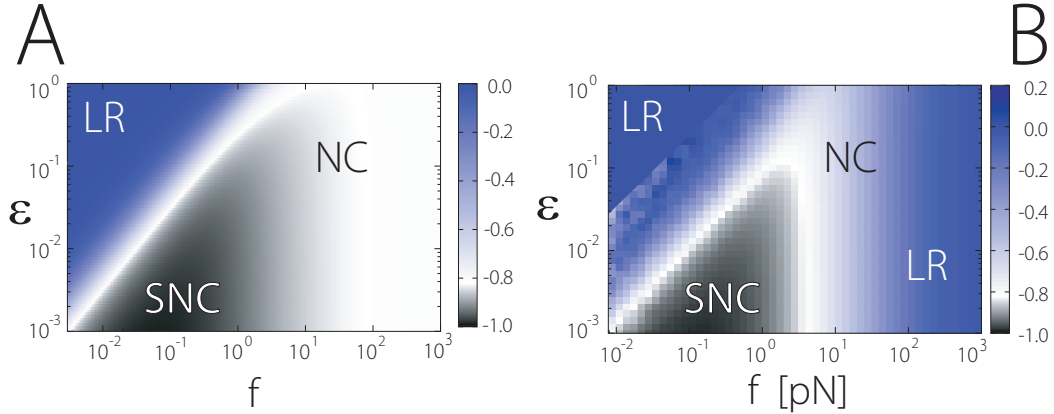


Figure 3.9: Local exponents of nonlinear compression. (A) For the subcritical Hopf oscillator ($\omega_0 = \omega = 1$, $r = -1$, $b = -1$, $c = 1$), we show α color coded as a function of noise intensity ϵ and driving amplitude f . Three different regimes are indicated: linear response (LR, $\alpha \approx 0$), nonlinear compression (NC) and strong nonlinear compression (SNC, $\alpha \gtrsim -1$). For the largest noise intensities shown, no strong nonlinear compression is realized. Instead, a direct crossover from linear response to the asymptotic value of $\alpha = -4/5$ for strong forcing amplitudes is observed. With decreasing noise strengths for intermediate driving amplitudes local exponents as low as -1 are found. The range of amplitudes for which strong nonlinear compression is observed with decreasing noise strength extends to smaller and smaller driving amplitudes. (B) For comparison, we plot α as a function of driving amplitude f and noise reduction factor ϵ in case of the the hair-bundle model operating at OP2 (same data as shown in fig. 2.10). Note the striking similarity of the data shown in A and B, respectively. The Hopf oscillator, apart from the linear response for strong driving, shares all the main features concerning nonlinear compression as found for the stochastic description of hair-bundle dynamics.

for the noisy Hopf oscillator exists whenever there is a range of forcing amplitudes f such that the condition

$$\epsilon/\hat{\rho} \ll f \ll \hat{\rho}(r + 3b\hat{\rho}^2 + 5c\hat{\rho}^4) \quad (3.32)$$

can be met. For the supercritical Hopf oscillator, with $\hat{\rho}$ given by eq. (3.4), this in particular implies that

$$\epsilon\sqrt{-b/r} \ll f \ll 2\sqrt{-r^3/b} \quad (3.33)$$

has to be fulfilled. Given the last equation, it is obvious that such a range will always be present whenever either the oscillator is operating far enough from the Hopf bifurcation, i.e. in the case that $-r$ is large enough, or if the noise strength ϵ is sufficiently small (see fig. 3.9). In the subcritical case, with ρ_d given by eq. (3.5), eq. (3.32) turns into

$$\frac{\sqrt{2c\epsilon}}{\sqrt{|b| + \kappa}} \ll f \ll \frac{\sqrt{|b| + \kappa}(\kappa - b)}{\sqrt{2c^3}}\kappa, \quad (3.34)$$

where $\kappa = \sqrt{b^2 - 4cr}$. Right at the bifurcation, i.e. $r = 0$, eq. (3.34) turns into

$$\epsilon\sqrt{c/|b|} \ll f \ll 2|b|^{5/2}/c^{3/2}. \quad (3.35)$$

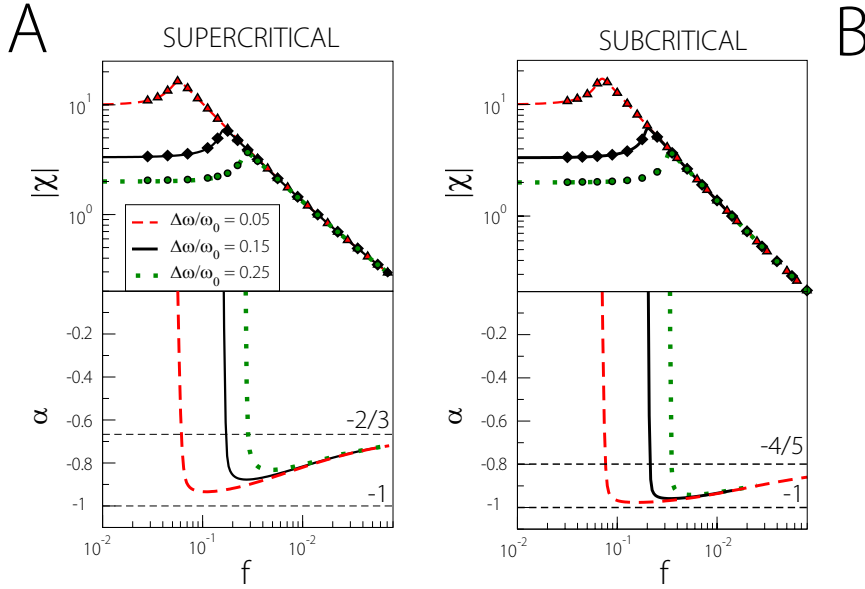


Figure 3.10: Sensitivity $|\chi|(f, \omega)$ (top) and local exponent α (bottom) vs forcing amplitude for the noisy Hopf oscillator ($r = -1$, $\omega_0 = 1$, $\varepsilon = 0.002$) for three different values of relative frequency mismatch. In (A), results for the supercritical Hopf oscillator ($b = 1$, $c = 0$), in (B), results for the subcritical Hopf oscillator ($b = -1$, $c = 1$) are shown. In the upper panels, stochastic simulations (symbols) are compared to theory (eq. (3.23), lines). Local exponents in the lower panels were determined by numerical differentiation using eq. (3.23).

This shows that for suitably small noise intensities in the subcritical case also right at the bifurcation strong nonlinear compression is possible. Note again, this is not the case for the supercritical Hopf oscillator.

We now turn to the case of a finite frequency mismatch, i.e. $\Delta\omega \neq 0$. In the last section, we have argued that for driving forces $f > |\Delta\omega|\hat{\rho}$, the oscillator will be strongly phaselocked to the external stimulus, i.e. $\zeta_\psi \lesssim 1$, so that ρ_d follows from eq. (3.25). In this regime, the detuned system responds as sensitive as the tuned system. Hence, in the limit of large input amplitudes, α will not be changed by the detuning (see fig. 3.10A and B). Also, we can extend the above conditions for strong nonlinear compression to occur. Local exponents of nonlinear compression close to -1 can be observed in the response of the detuned system whenever there is a range of forces such that the condition

$$|\Delta\omega|\hat{\rho} \ll f \ll \hat{\rho}(r + 3b\hat{\rho}^2 + 5c\hat{\rho}^4)$$

can be met (see fig. 3.10A and B).

3.5 Summary

In this chapter, we have discussed the spontaneous and driven dynamics of the noisy phase and Hopf oscillator. The quality of spontaneous oscillations in case of the phase oscillator was shown to be inversely proportional to the noise strength. The same holds true for the Hopf oscillator in the limit of weak noise. In particular, in the case of the Hopf oscillator we have derived an analytical expression for the full nonlinear response function and the local exponent of nonlinear compression α . We have shown that for both oscillators the linear response level for tuned stimuli is inversely proportional to the noise strength. In the limit of strong driving, the decay of the sensitivity of the Hopf oscillator corresponds to a local exponent of nonlinear compression $\alpha = -2/3$ in the supercritical and $\alpha = -4/5$ in the subcritical case. For weak noise, and in the supercritical case a suitable distance from the bifurcation, a regime of strong nonlinear compression with $\alpha \gtrsim -1$ can be observed.

The results presented here shed some light on the findings discussed in the last chapter. Indeed, for the stochastic hair-bundle description eq. (1.10) and eq. (1.11), power spectral densities and sensitivity curves, apart from the linear response at strong driving, are similar to the respective statistics encountered for the noisy Hopf oscillator. In further agreement, the quality of spontaneous oscillations and the amplification gain also in case of the hair-bundle model were found to be inversely proportional to the noise strength. Furthermore, similar regimes of nonlinear compression were observed. Note that the operation points OP1 and OP2 are close to a supercritical and subcritical Hopf bifurcation, respectively.

Chapter 4

Theory of coupled hair bundles

The performance of an isolated hair bundle as a nonlinear amplifier is seriously impeded by intrinsic fluctuations ([118], see also chapter 2). Noise not only leads to a poor phase coherence of spontaneous oscillations, but also limits the amplification gain of the hair bundle. Within the theoretical framework discussed in the last chapter, the detrimental effect of noise became particularly salient. The quality of spontaneous oscillations as well as the sensitivity in linear response for two generic oscillators were shown to be inversely proportional to the noise intensity. As discussed in the introduction (see section 1.4.4), most hair bundles are elastically coupled by overlying gelatinous membranes. In this chapter, we will present the results of a computational study that was aimed at investigating the possible effects of such an elastic coupling on hair-bundle dynamics. Most importantly, we will show that due to a noise reduction effect, elastic coupling is expected to effect an increased phase coherence of spontaneous oscillations and a significantly enhanced gain of the hair-bundle amplifier.

4.1 Physical description of coupled hair bundles

In this section, we will introduce the biophysical description of coupled hair bundles on which the results presented in this chapter are based.

While the excitatory directions of hair bundles typically are locally aligned (see fig. 4.1), their overall arrangement differs from one inner ear organ to the next. In the sacculus of the bullfrog, the sensory macula is endowed with about 3000 hair bundles forming a hexagonal lattice with an approximate center-to-center spacing of about $12 \mu\text{m}$ [75]. In the mammalian cochlea, three rows of outer hair cells can be discerned. The inter-row distance in humans changes gradually from $10 \mu\text{m}$ at the base, to about $25 \mu\text{m}$ at the apex [13]. Thus the typical distance between hair bundles is large compared to the amplitude of several tens of nanometers reported for spontaneous hair-bundle oscillations. Here we do not aim at a detailed geometric representation of all the various arrangements realized *in vivo*. Instead, we will discuss a more generic situation. Specifically, in our model hair bundles are arranged

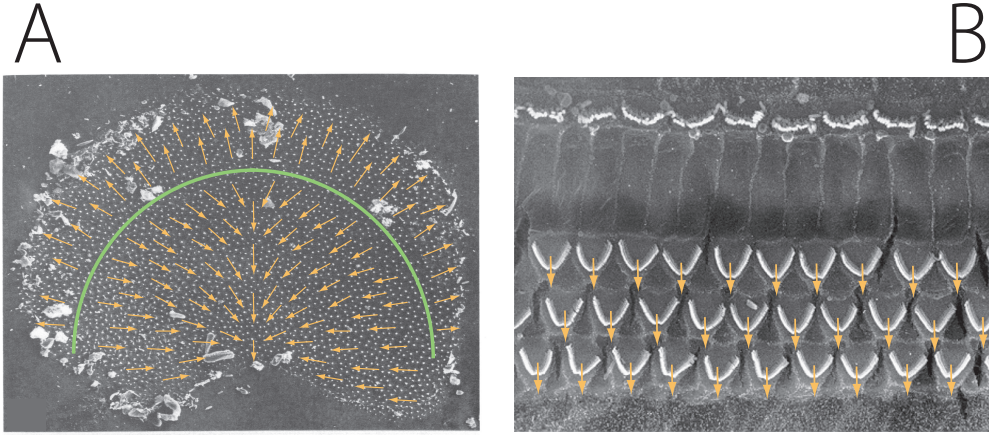


Figure 4.1: Hair-bundle orientations in sensory epithelia. In most inner ear organs the excitatory directions of hair bundles are locally aligned. We show two examples. In (A), a top view of the saccular macula of the bullfrog is displayed. The otolithic membrane has been removed. Each of the small white dots corresponds to a sensory hair bundle. We indicate the approximate local direction of mechanosensitivity by means of arrows. Note the gradual change of hair-bundle orientation over most of the epithelium. An exception is the so called striola, sketched here as a green arc. This imaginary line separates hair bundles with opposite excitatory directions. Adapted from [75]. In (B), we show a section of the rabbit cochlea with the tectorial membrane removed. Locally, the excitatory directions of outer hair cells are parallel. On larger length scales, with the cochlea having the shape of a coiled snail, orientations, however, gradually change. Adapted from [25].

on a square lattice with spacing d (see fig. 4.2). We chose $d = 50 \mu\text{m}$, a value which is comparable to typical hair-bundle distances. We have checked that the exact choice of the lattice spacing is immaterial, as long as it is large compared to the amplitude of spontaneous oscillations.

Hair bundles are labeled (i, j) according to their position on the lattice, where $i = 1, \dots, N$ and $j = 1, \dots, M$. Each hair bundle is described by two variables $X^{i,j}$ and $X_a^{i,j}$, characterizing the stereociliary deflection and the state of adaptation motors, respectively (see section 1.4.3). We consider hair bundles that are all oriented with their excitatory direction in the positive X direction and $X^{i,j}$ are the deflections along this direction. In the following, we ignore deflections in the Y direction. A given hair bundle at site (i, j) is coupled via linear springs to the neighboring hair bundles at sites $(i + k, j + l)$ with $k, l = -1, 0, 1$, including diagonal connections. Boundary conditions are introduced via the boundary sites (k, k') where at least one of these indices is 0, $N + 1$ or $M + 1$ (see grey boxes in fig. 4.2). We focus on open boundary conditions for which no elastic connections exist to the boundary sites. In the case of fixed boundaries these connections exist and $X_{k,k'} \equiv 0$ for all boundary sites. Periodic boundary conditions can be defined in a standard way by setting $X_{i,0} = X_{i,M}$, $X_{i,M+1} = X_{i,1}$, $X_{0,j} = X_{N,j}$, $X_{N+1,j} = X_{1,j}$ for $i = 1, \dots, N$ and $j = 1, \dots, M$, $X_{0,0} = X_{N,M}$, $X_{N+1,0} = X_{1,M}$, $X_{0,M+1} = X_{N,1}$, and $X_{N+1,M+1} = X_{1,1}$.

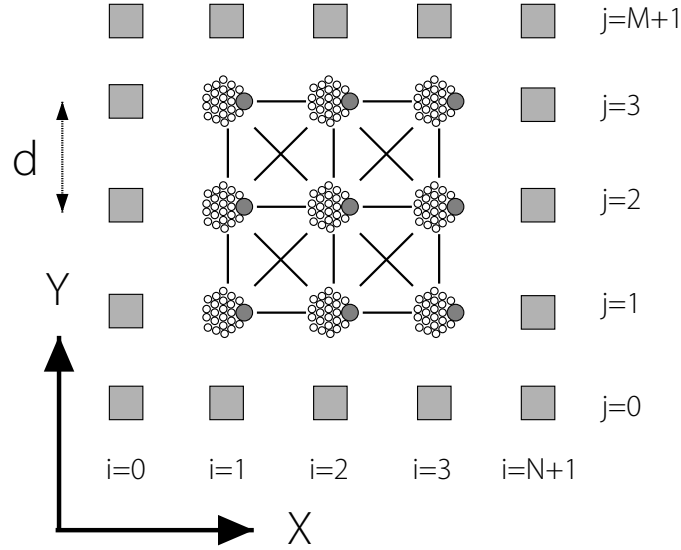


Figure 4.2: Schematic topview of the proposed model. Hair bundles are arranged on a square lattice with spacing d . Each hair bundle is labelled (i, j) according to its position on the lattice. Black lines represent springs. The excitatory direction of the hair bundles is the positive X direction. Here we ignore movements in the Y -direction. Note that the extension of diagonal and vertical springs, however, depends on the fixed offset d in the Y -direction.

We will consider both the spontaneous activity of coupled hair bundles, as well as their response to a periodic stimulus force. In the latter case, all hair bundles are stimulated by the same periodic force $F_{\text{ext}}(t) = F \cos(2\pi f_s t)$. This corresponds to a situation in which a collection of hair bundles is mechanically stimulated by a periodic shear stress applied homogeneously via the overlying elastic membrane.

The equations governing the dynamics of a system of coupled hair bundles thus read

$$\lambda \dot{X}^{i,j} = f_X(X^{i,j}, X_a^{i,j}) + F_{\text{ext}}(t) + \xi^{i,j}(t) - \sum_{k,l=-1}^1 \frac{\partial U(X^{i,j}, X^{i+k,j+l})}{\partial X^{i,j}} \quad (4.1)$$

$$\lambda_a \dot{X}_a^{i,j} = f_{X_a}(X^{i,j}, X_a^{i,j}) + \xi_a^{i,j}(t), \quad (4.2)$$

where the prime in the first equation indicates that the sum excludes boundary sites for open boundary conditions. The functions f_X and f_{X_a} , which are describing the deterministic aspect of single hair-bundle dynamics, are given by

$$f_X(X, X_a) = -K_{\text{GS}}(X - X_a - DP_o) - K_{\text{SP}}X$$

and

$$f_{X_a}(X, X_a) = K_{\text{GS}}(X - X_a - DP_o) - F_{\text{max}}(1 - SP_o),$$

respectively (see section 1.4.3). The noise terms $\xi^{i,j}$ and $\xi_a^{i,j}$, whose noise strength is given in eq. (1.12), are assumed to be pairwise independent. The potential corresponding to the elastic forces with spring constant K is given by

$$U = \frac{K}{2} \left(\sqrt{(X^{i+k,j+l} + kd - X^{i,j})^2 + l^2 d^2} - \sqrt{k^2 + l^2 d} \right)^2.$$

Note that the particular form of the interaction potential results from neglecting any dynamics in Y . This variable, however, still contributes via the diagonal springs. The interaction strength between hair bundles is tuned by the single elastic coefficient K . We will refer to the latter as the coupling stiffness or coupling strength.

Unless stated otherwise, only homogeneous systems will be considered, i.e. for all hair bundles the same parameters are implemented. In particular, we chose parameters according to OP2 (see table 1.1).

We will in the following discuss most statistics as functions of the coupling stiffness K . It is possible, however, to derive rough estimates of the coupling strength realized *in vivo* from the Young's modulus E of the membrane overlying the hair bundles. Based on dimensional analysis we expect that $K \approx E \cdot d$. For the otolithic membrane of the bullfrog's sacculus $E \approx 6.6$ kPa has been suggested [87]. With $d = 12 \mu\text{m}$ this leads to an estimate of $K = 79.2$ pN/nm, a value that is large compared to the passive pivotal stiffness K_{SP} of the hair bundle. Consistent with these putative large coupling strengths, recent experiments have shown that deflections applied locally to the otolithic membrane itself can induce correlated passive hair-bundle movements over a significant portion of the whole saccular epithelium [155]. Note, however, the above estimate does not take into account the three dimensional shape of the otolithic membrane that exhibits large cavities inside which hair-bundle tips are attached [80]. This specific geometry and a potentially soft coupling of the hair bundle to the otolithic membrane could reduce K . In the mammalian cochlea the Young's modulus of the tectorial membrane has been estimated and exhibits a gradient of tectorial stiffness [181, 2, 147, 58, 135, 50]. Values reported range from $E = 0.3$ kPa at the apex to 3 kPa at the base in gerbil [135] and from $E = 24$ kPa at the apex to 224 kPa at the base in mouse [58]. With the distance between two rows of outer hair cells being on the order of $10 \mu\text{m}$, the values observed in gerbil yield $K = 3 - 30$ pN/nm, which is comparable to passive stiffnesses of hair bundles in the mammalian cochlea [154]. The data obtained in mice suggest that $K = 240 - 2240$ pN/nm, a coupling strength that considerably exceeds K_{SP} . Note, however, that here we have neglected the effect of directional anisotropies conferred to the tectorial membrane by collagen fibrils which are organized in radial fibers [50]. Recently, it has been proposed that due to this morphological specialization, elastic coupling between outer hair cells could be stronger in the radial direction, i.e. along the direction of hair-bundle excitation, as compared to the longitudinal direction.

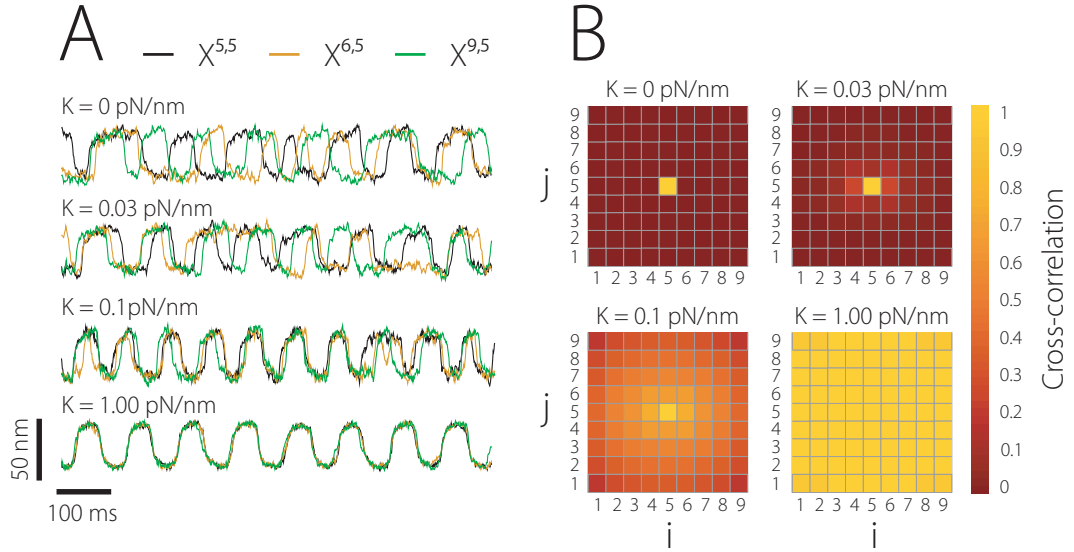


Figure 4.3: Synchronization of elastically coupled hair bundles. We present simulation results for a 9×9 system. (A) For four different coupling strengths as indicated, we plot trajectories of the hair bundle deflections $X^{5,5}$ (central hair bundle), $X^{6,5}$ and $X^{9,5}$. While being uncorrelated in the absence of coupling, under strong coupling ($K = 1.0$ pN/nm) hair-bundle movements are almost perfectly synchronized. Also note the more regular shape of the oscillations under strong coupling. (B) For the same coupling strengths as in A, we show color plots of cross-correlation coefficients determined between the central hair bundle and each of the 81 hair bundles in the system. Note that by definition this implies a cross-correlation of unity for the central hair bundle. With increasing coupling strength hair-bundle movements become more and more correlated. In all cases, cross-correlations decrease with increasing distance on the lattice.

4.2 Spontaneous noisy oscillations and synchronization

In this section, we discuss the effects of elastic coupling on the spontaneous dynamics of quadratic $N \times N$ arrays of interconnected hair bundles.

In the absence of coupling, i.e. $K = 0$ pN/nm, hair bundles move independently from one another (see fig. 4.3A). An increase of the coupling strength leads to a progressive synchronization of the performed spontaneous oscillations (see fig. 4.3A, $K = 0.03 - 1.00$ pN/nm). We characterized the degree of synchronization by means of cross-correlation coefficients. For two hair bundles at respective sites (i, j) and (m, n) the cross-correlation coefficient is given by

$$C = \frac{\langle (X^{i,j} - \langle X^{i,j} \rangle)(X^{m,n} - \langle X^{m,n} \rangle) \rangle}{\sqrt{\text{Var}(X^{i,j})\text{Var}(X^{m,n})}},$$

where $\text{Var}(X^{i,j})$ and $\text{Var}(X^{m,n})$ denote the variance of the deflections $X^{i,j}$ and $X^{m,n}$, respectively. For a 9×9 array we show in fig. 4.3B for various choices of the coupling stiffness K color plots of the cross-correlation coefficients between the central hair bundle at site $(5,5)$ and all 81 hair bundles in the system. Cross-correlations

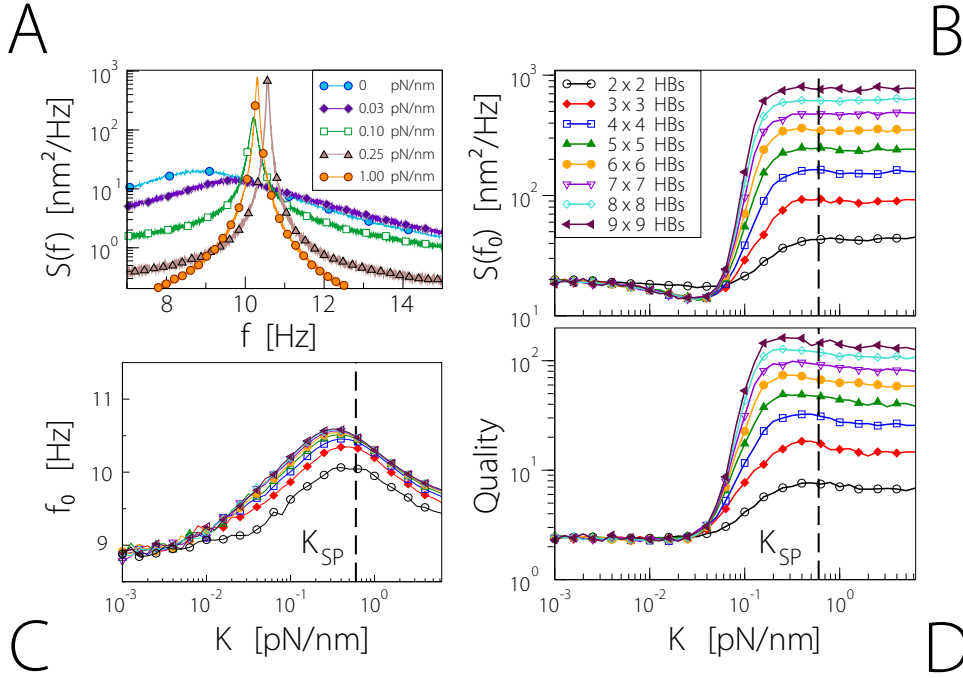


Figure 4.4: Spectral statistics of spontaneous oscillations in systems of elastically coupled hair bundles. In (A), we show power spectra of the central hair bundle in a 9x9 system for various K as indicated. Note the sharpening of the spectral peak. In (B), the peak height $S(f_0)$, in (C), the characteristic frequency f_0 , and in (D), the quality factor Q of the central hair bundle in systems of different sizes is shown as a function of coupling strength K . System sizes for C and D are indicated in B. We mark the passive hair bundle stiffness K_{SP} by vertical, dashed lines in B, C, and D. Note that while the frequency changes only mildly (less than 10%), the peak height and quality beyond a certain critical value increase rapidly, and in the strong coupling regime approach a size-dependent value which is larger than in the uncoupled case.

increase along with coupling strength K . Note that for a given coupling stiffness cross-correlations decay with increasing distance from the central hair bundle. For sufficiently strong coupling (see the data for $K = 1$ pN/nm in fig. 4.3A and B) all hair bundles in the array are almost perfectly synchronized. The cross-correlation coefficient between any two hair bundles in this case is close to one (not shown).

In order to reveal the effect of coupling on the phase coherence of spontaneous oscillations, we varied the spring constant K and the system size, and determined the power spectrum $S(f)$ of the central hair bundle's displacement. The central hair bundle is the hair bundle at position $(\frac{1}{2}(N+1), \frac{1}{2}(N+1))$ in the case of odd N , or in the case of even N at position $(\frac{1}{2}N, \frac{1}{2}N)$. The power spectral density was defined in section 2.1. Power spectra for increasing coupling strength K , shown in fig. 4.4A for a 9×9 array, demonstrate a sharpening of the spectral peak, indicative of an increased degree of phase coherence. This is further quantified in fig. 4.4B and fig. 4.4D in terms of the height $S(f_0)$ of the spectral peak at its characteristic frequency f_0 , and its quality factor $Q = f_0/\Delta f$ (see section 2.1). The height and

quality dependence on K reveal three regimes: weak (low plateau), intermediate (steep slope), and strong coupling (high plateau). In the latter two regimes, the height and quality of the spectral peak depend on the system size — the respective plateau at large K is growing with N . Note that coupling strengths larger than the pivotal stiffness K_{SP} belong to the strong coupling regime. The frequency f_0 varies only mildly with increasing coupling strength (about 10%; fig. 4.4C) resulting in a shallow maximum of the quality factor vs the coupling strength K .

We conclude, elastic coupling in our simulations synchronizes hair bundle movements and causes the latter to perform oscillations of higher quality, i.e. with a higher phase coherence. Note that a similar enhancement upon a reduction of intrinsic fluctuations was observed for a single hair bundle (see chapter 2) and for the two generic oscillators discussed in the last chapter.

4.3 Nonlinear amplification

The main task of hair bundles is the transduction and amplification of sound signals. In this section, we therefore study how the linear and the nonlinear response of a system of coupled hair bundles depends on coupling parameters, i.e. system size and coupling strength.

All hair bundles in a given system were simultaneously driven with a periodic stimulus $F_{\text{ext}}(t) = F \cos(2\pi f_s t)$. We characterized the response of the central hair bundle by means of the sensitivity $|\chi|(F, f_s)$ and the amplification gain G . Both measures were introduced in section 2.2.

The sensitivity as a function of coupling strength for a driving at the characteristic frequency, i.e. $f_s = f_0$, is displayed in fig. 4.5A. The resulting behavior resembles the one of the spectral peak height discussed in the previous section. At weak coupling the sensitivity changes little with increasing coupling or system size and is close to the value of a single hair bundle ([118], also see section 2.2). Beyond a certain critical coupling $K \gtrsim 0.1$ pN/nm, the sensitivity sharply increases and saturates at a size-dependent level.

In order to characterize the best possible performance, for the following we have tuned the coupling strength such that the sensitivity is at or close to its high-coupling limit. Specifically, we have chosen the coupling strength that maximizes the quality of the spontaneous activity. We have checked that the exact value of the coupling was immaterial as long as we were in the strong coupling regime discussed above.

The sensitivity for weak stimuli, i.e. in the sensitive linear response regime, is shown in fig. 4.5B as a function of the frequency mismatch $f_s - f_0$. Close to the spontaneous frequency ($f_s \approx f_0$), the sensitivity attains its maximum which increases and sharpens strongly for increasing N . For large frequency mismatch the sensitivity is independent of N .

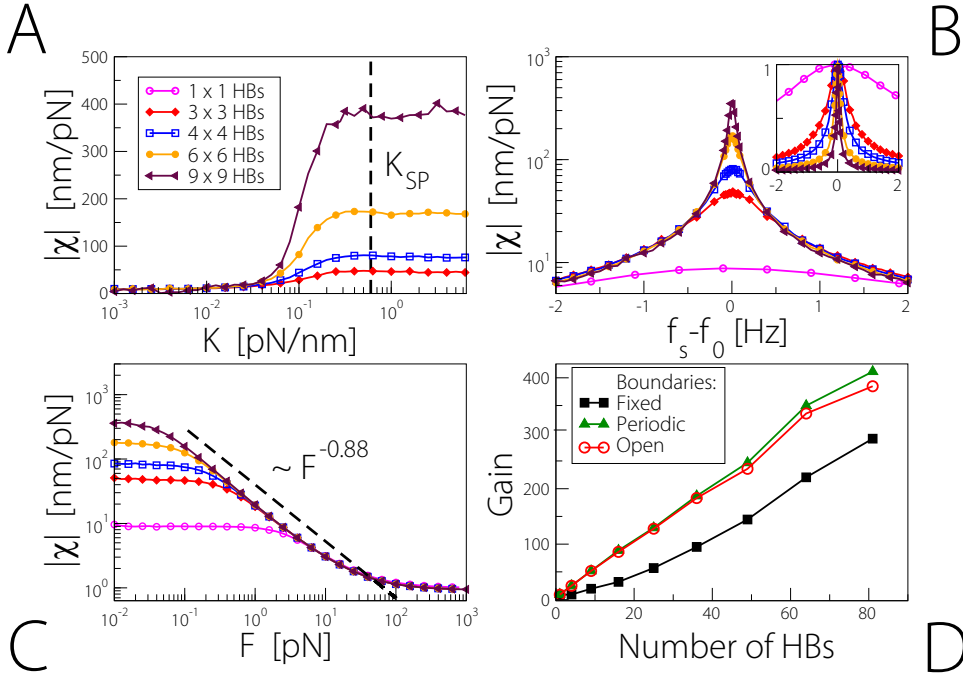


Figure 4.5: Sensitivity with respect to a periodic driving. In (A), we plot the sensitivity $|\chi|(F, f_0)$ for a driving with $f_s = f_0$ at weak forcing ($F = 0.1$ pN for 1×1 , $F = 0.05$ pN for 3×3 , 4×4 , $F = 0.025$ pN for 6×6 , $F = 0.01$ pN for 9×9) vs coupling strength. For comparison, we mark the passive stiffness K_{SP} of a single hair bundle by a dashed line. Note that the sensitivity in the strong coupling regime is enhanced. In (B), we show $|\chi|(F, f_s)$ as a function of frequency detuning for coupling strengths corresponding to the strong coupling regime. In particular, K was chosen so as to maximize the quality of spontaneous oscillations ($K = 0.45$ pN/nm for 3×3 and 4×4 , $K = 0.32$ pN/nm for 6×6 , $K = 0.28$ pN/nm for 9×9). The driving amplitude was adjusted so as to be in the sensitive linear response regime for weak driving (same driving forces as in A). The inset in (B) shows all the data with their maxima rescaled to one. Note the sharpening of these tuning curves with increasing system size. In (C), we show $|\chi|(F, f_0)$ as a function of driving amplitude for the same coupling strengths as in (B). As a dashed line we indicate a power law F^{α_0} with an exponent $\alpha_0 = -0.88$. In (D), we display the gain G (defined by eq. (2.8)) as a function of the total number of hair bundles (boundary conditions as indicated). Note the linear increase for open and periodic boundary conditions.

The nonlinear response to periodic forcing can be characterized by the dependence of the sensitivity on the forcing amplitude F (see fig. 4.5C). As shown earlier, a clear nonlinearity can be seen already for a single hair bundle ([118] and section 2.2). At small driving amplitude, the linear response regime for weak driving amplitudes manifests itself by a plateau. At higher values of F , the sensitivity decreases approximately like a power law $|\chi| \sim F^{\alpha_0}$. For still larger driving amplitudes the response is linear again. By increasing the system size we increase considerably the range of forcing amplitudes for which a power law applies. For a 9×9 array, the sensitivity exhibits a power-law behavior with $\alpha_0 \approx -0.88$ over at least two orders of magnitude. Note that the value of α_0 is smaller than the one characterizing the

nonlinearity for a single hair bundle ($\alpha_0 \approx -0.66$). The value of α_0 reported here implies an even stronger nonlinear compression.

We find that the gain increases almost linearly with the number of hair bundles (see fig. 4.5D)) and attains a value of about 400 for a 9x9 array. Note that this value is comparable to the gain of the mammalian cochlea as observed in basilar membrane vibrations upon acoustic stimulation [138]. In order to verify that this result is not solely due to the kind of boundary conditions chosen we repeated the simulations for periodic and fixed boundary conditions. The resulting gain (see fig. 4.5D) demonstrates that even in the rather pessimistic setting with fixed boundaries an enhancement effect (although reduced compared to the case with open boundary conditions) survives. Interestingly, the curve for periodic boundary conditions differs only marginally from the main result for open boundary conditions.

The observed effects of coupling on the driven dynamics of hair bundles closely parallel the findings for the noisy Hopf oscillator discussed in chapter 3 and those for a single hair bundle presented in chapter 2. In both cases a reduction of the noise level brought about a similar enhancement as reported here. E.g. for a single hair bundle, a reduction of intrinsic fluctuations not only sharpens the tuning (see fig. 2.8B), but also the amplification gain increases linearly with inverse noise reduction factor (see fig. 2.7). Also the larger degree of nonlinear compression upon coupling can readily be understood with reference to our discussion of the response of the the hair bundle in terms of the local exponent α of nonlinear compression. In section 2.3, we have pointed out that upon a sufficient reduction of the noise level, a single hair bundle operating at OP2 will exhibit regimes of nonlinear compression corresponding to local exponents α as small as -1. In light of these results, also the decrease of α_0 observed here highlights the possibility that the main effect of elastic coupling is an effective reduction of the noise strength shaping the dynamics of the central hair bundle. Note that in agreement with this interpretation, coupling has no appreciable effect on e.g. the sensitivity in the linear response regime for strong driving amplitudes. In the framework of a mean-field type argument we will show in section 4.6 in what sense elastic coupling, indeed, leads to such an effective noise reduction.

In summary, we conclude that elastic coupling can bring about a pronounced enhancement of the hair bundles' signal detection and amplification properties. While here we discuss the response solely in terms of the central hair bundle, we stress that we observed similar effects for all hair bundles in a given system. In the strong coupling regime, with all hair bundles being strongly synchronized, also their respective tuning characteristics and amplification gains were similar.

4.4 Transient responses

So far, we have discussed the response of coupled hair bundles for long stimulation times after transients have vanished. After a stimulus is switched on it takes,

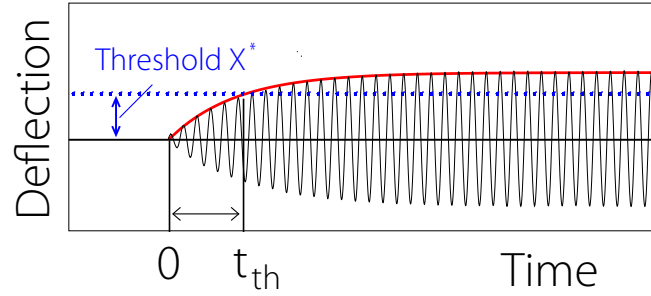


Figure 4.6: Transient build-up of the mean hair-bundle response. When all hair bundles in a given system (here 3x3) receive a stimulus $F_{\text{ext}}(t) = F \cos(2\pi f_0 t)$ which is switched on at $t = 0$, the time-dependent mean value of the central hair bundle's deflection for $t > 0$ performs an oscillation of the same frequency. The amplitude of the response relaxes exponentially to its final value. We show this mean response (averaged over 263000 realizations) as a black line for a stimulation amplitude of $F = 0.065$ pN. We indicate the relaxation by a fit of the envelope from eq. (4.3) (red line). We indicate the detection threshold X^* as a dashed blue line. Note that the response amplitude reaches the threshold within a time t_{th} . For this choice of detection window t_{th} , the minimal threshold force is thus given by $F^* = 0.065$.

however, a certain time until the system reaches its final response amplitude (see fig. 4.6). In this section, we will discuss certain aspects related to the time course of this transient response build-up.

To this end, we determined the relaxation time τ of the mean response amplitude after a periodic stimulus ($f_s = f_0$) was switched on at time $t = 0$ (fig. 4.6). For $t > 0$ the response is well described by

$$\langle X(t) \rangle \approx F |\chi|(F) (1 - \exp[-t/\tau(F)]) \cos(2\pi f_0 t - \phi_1), \quad (4.3)$$

where ϕ_1 denotes the phase shift of the mean response with respect to the periodic stimulus. Note that here we have neglected the possible presence of higher harmonics in the response. The relaxation time $\tau(F)$ obtained by a fit of this expression to simulation data is displayed in fig. 4.7A as a function of stimulus amplitude F for various system sizes. The coupling stiffness K was chosen so as to maximize the central hair bundle's quality of oscillation. At small amplitude, the relaxation time is largest and is approximately given by

$$\tau \approx Q/(\pi f_0) = \tau_{\text{corr}},$$

shown by solid lines in fig. 4.7A. Note that τ coincides with the relaxation time τ_{corr} of the autocorrelation function of hair-bundle deflections (see section 2.1). In the absence of an external stimulus, τ_{corr} is a measure for the time it takes for correlations to die out among independent hair bundles with identical initial conditions¹.

¹To avoid confusion: these independent hair bundles could also be elements of independent systems of coupled hair bundles of identical size and identical initial conditions.

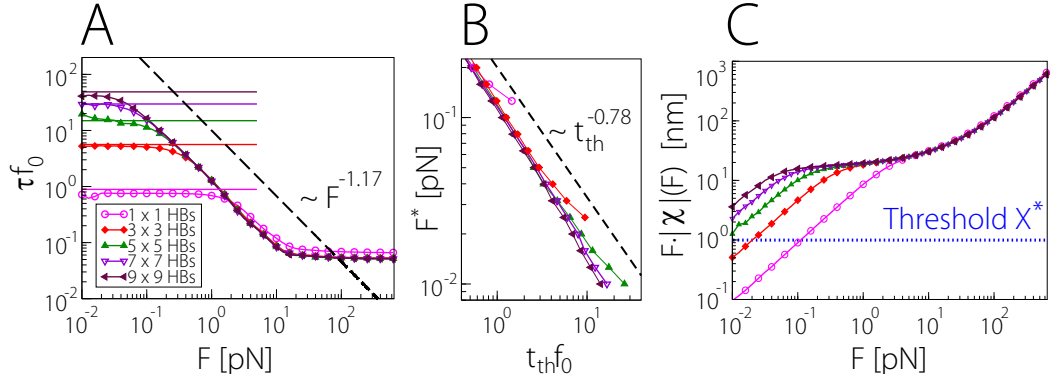


Figure 4.7: Transient response of driven oscillations. In (A), we show the relaxation time $\tau(F)$ obtained from fits as shown in fig. 4.6 in units of driving periods f_s^{-1} (note that here $f_s = f_0$) as a function of forcing amplitude F . We present data for various system sizes as indicated. For weak forcing, we find that $\tau = Q/(\pi f_0)$ (horizontal lines). For intermediate forcing amplitudes the data is well described by a power law decay with $\tau \sim F^{-1.17}$ (dashed line). In (B), we display the minimal force F^* needed to reach a given threshold X^* after a given number $t_{th} f_0$ of stimulus cycles. For large systems we find that approximately $F^* \sim t_{th}^{-0.78}$ (dashed line). In (C), we show the final response amplitude $F \cdot |\chi|(F)$, i.e. after the response amplitude has fully relaxed. This shows that the threshold $X^* = 1$ nm for all system sizes considered here lies in the sensitive linear response regime for weak forcing. Note that in this representation, a linear response regime, in which by definition the response amplitude grows proportional to the driving amplitude F , corresponds to a slope of unity.

Reciprocally, in linear response τ_{corr} determines how fast correlations among independent hair bundles with random initial states are build up by means of a weak periodic signal.

A 9×9 system relaxes at weak stimulus after about 100 stimulation cycles, whereas a single hair bundle already relaxes after one cycle. The relaxation time decreases for stronger stimuli as a power law $\tau \sim F^{\beta_0}$ with $\beta_0 \approx -1.17$. This power law occurs in the same range of stimulus amplitudes as does the power law of the sensitivity (cf. fig. 4.5C). Therefore, as the stimulus amplitude is increased, sensitivity is reduced; the response, however, builds up faster. We note that the relaxation time saturates for strong forcing at a value corresponding to the relaxation time of the passive system. The latter can be estimated as $\tau_\infty \approx (K_{GS} + K_{SP})/\lambda$ and is much shorter than $1/f_0$, i.e. one oscillation cycle.

For a sound detector such as the hair bundle an important property is the minimal force amplitude F^* required for the mean response to reach a detection threshold X^* within a given time t_{th} (see fig. 4.6). Using eq. (4.3) we determine the relation between t_{th} and F^* as

$$t_{th} = \tau(F^*) \ln \frac{F^* |\chi|(F^*)}{F^* |\chi|(F^*) - X^*}. \quad (4.4)$$

This relation is displayed in fig. 4.7B using our simulation data for arrays of different sizes and a physiologically reasonable threshold amplitude of $X^* = 1$ nm [43]. For

increasing detection window t_{th} , the threshold amplitude F^* decreases. As the final response amplitude $F \cdot |\chi|(F)$ (see fig. 4.7C) tends to zero for decreasing driving amplitude, a minimal threshold, however, exists. For a threshold of 1 nm this minimal threshold amplitude for all studied system sizes is attained in the linear response regime for weak driving amplitudes. This can also be understood with recourse to the results presented in chapter 3. There we have shown that the noisy Hopf oscillator responds in a linear fashion at least up to a driving amplitude for which the phase-locked response has an amplitude that is comparable to the one of the spontaneous oscillation. At OP2, hair bundle oscillations have an amplitude of about 20 nm, i.e. are much larger than the threshold considered here. It is therefore, indeed, to be expected that the minimal threshold amplitude will fall into the linear response regime even for larger system sizes. The minimal threshold force is then given by $X^*/|\chi|(F=0)$, where $|\chi|(F=0)$ denotes the limiting value of the sensitivity for weak driving amplitudes, i.e. the linear response level. For increasing system size, cooperativity of hair bundles leads to a reduction of this minimal threshold force (see fig. 4.7B). While sensitivity thus is enhanced, it requires increasingly large stimulus durations t_{th} in order for the response amplitude to reach the threshold. Note, however, that in case of a 9x9 system for a force amplitude of $F = 10^{-2}$ pN, which is in the sensitive linear response regime, only about 20 stimulus cycles ($t_{\text{th}} = 20 f_0^{-1}$) are required to reach the detection threshold of $X^* = 1$ nm.

For large systems, we obtain a power law for the dependence of the threshold amplitude F^* on the detection window size t_{th} . Its exponent can be estimated by noting that

$$\begin{aligned} t_{\text{th}} &= \tau(F^*) \ln\left(1 + \frac{X^*}{F^*|\chi|(F^*) - X^*}\right) \\ &\approx \tau(F^*) \frac{X^*}{F^*|\chi|(F^*)} \\ &\sim F^{*-1-\alpha_0+\beta_0}, \end{aligned}$$

where we have used that for large systems and intermediate forcing amplitudes $F|\chi|(F) \gg X^*$, while also $|\chi|(F) \sim F^{\alpha_0}$ and $\tau(F) \sim F^{\beta_0}$. We thus find the power law dependence $F^* \sim t_{\text{th}}^{1/(-\alpha_0+\beta_0-1)}$ which is indicated in fig. 4.7C as a dashed line. We note here that in many hearing organs so-called temporal integration curves have been measured [38, 45], revealing nonlinear relationships between the detection threshold and the duration of a sound stimulus. Often power laws close to $F^* \sim t_{\text{th}}^{-3/8}$ are reported [38] (assuming that F is proportional to stimulus pressure). As shown above, coupling of hair bundles naturally generates power laws, albeit with an exponent closer to $-3/4$ than to $-3/8$.

4.5 Heterogeneities

In the above, we have considered systems of $N \times N$ identical hair bundles. However, in vertebrate hearing organs neighboring hair cells can differ in their characteristic frequencies. For instance, in the cochlea outer hair cells exhibit a frequency gradient along the basilar membrane. To verify that the effects discussed above are not solely due to the specific setup chosen, we have also investigated systems of $N \times M$ coupled hair bundles with different values of N and M , and random and graded frequency profiles with up to 20% frequency variability. In general, if the coupling is sufficiently strong, we recover all of the effects found in homogeneous quadratic systems (synchronization, enhanced frequency tuning, and enhanced gain). In this section, we discuss the specific case of $N=3$ and $M=27$, thus mimicking the geometric setup as realized in the cochlea.

Along the basilar membrane for each distance from the stapes a unique characteristic frequency f_{CF} exists (see section 1.1). This frequency decreases almost exponentially from base to apex, i.e.

$$f_{CF}(x) \approx \omega_0 e^{-\frac{x}{l}}, \quad (4.5)$$

where x denotes distance from the stapes, ω_0 is the frequency at the base, and l is a decay length. In the case of the mammalian cochlea $l \approx 7$ mm [57]. In each of the three rows of outer hair cell, the human cochlea along its length of about 35mm [164] hosts approximately 4000 outer hair cells. With the longitudinal distance between two outer hair cells thus being on the order of $10 \mu\text{m}$, 27 rows of outer hair cells span only about 0.26 mm, i.e. a fraction of the decay length l . The frequency gradient over 27 triplets of outer hair cells can thus be assumed to be almost linear. In the following we will therefore investigate the effect of graded frequency profiles in form of linear frequency gradients only.

Note that the intrinsic frequency of an individual hair bundle depends on the pivotal stiffness K_{SP} in an almost linear fashion (see inset of fig. 4.8A). By varying K_{SP} between 0.5 pN/nm and 0.7 pN/nm, we can tune the spontaneous oscillations to frequencies varying about 20%.

In a 3×27 system we could thus introduce an intrinsic linear frequency gradient along the Y -axis by a linear gradient of pivotal stiffness with a range ΔK_{SP} . Denoting the passive stiffness of the hair bundle at site (i, j) by $K_{SP}^{i,j}$ we used

$$K_{SP}^{i,14+j} = \bar{K}_{SP} + j \cdot K_{SP}/26 \quad \text{for } j = -13, \dots, 13.$$

Therefore \bar{K}_{SP} is the pivotal stiffness of the central hair bundle at site $(2, 14)$ and coincides with the average stiffness of all hair bundles in the system. In our simulations we have used $\bar{K}_{SP} = 0.6$ pN/nm. The remaining hair-bundle parameters were identical throughout the system and were chosen according to OP2 (see table 1.1).

Denoting by $f_0^{i,j}$ the characteristic frequency of the hair bundle at site (i, j) , the frequency range for a given system is then defined as $\Delta f_0 = f_0^{2,27} - f_0^{2,1}$. The

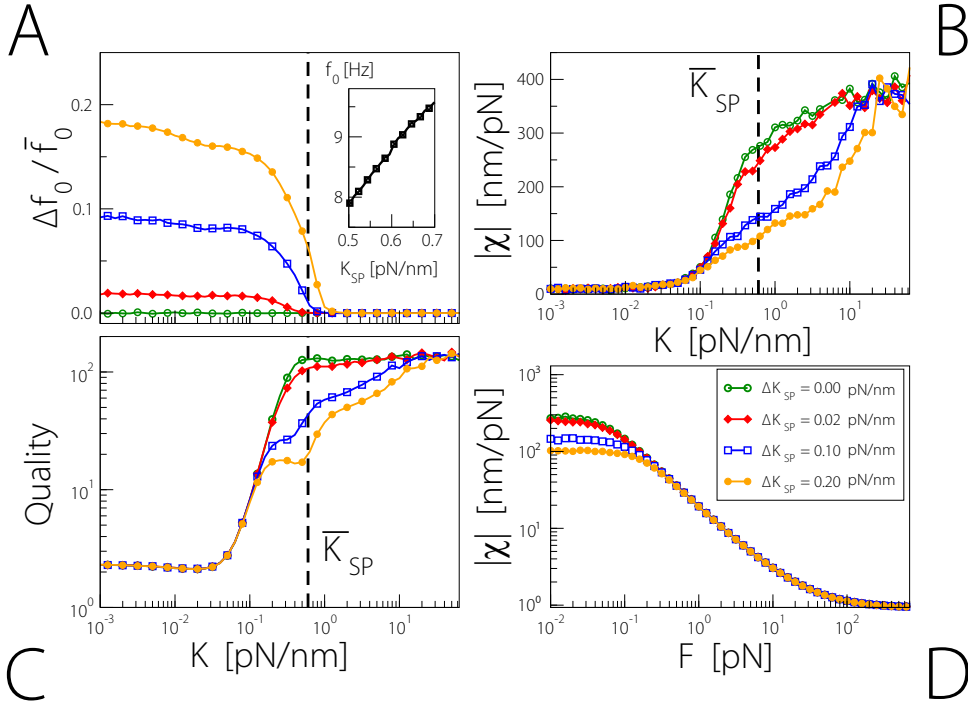


Figure 4.8: The effect of a linear stiffness gradient in a system of 3x27 coupled hair bundles. Four different frequency gradients are generated by a linear variation of pivotal stiffness over different ranges ΔK_{SP} as indicated in D. For all systems we have chosen $\bar{K}_{SP} = 0.6$ pN/nm. In (A) for each system we plot the relative frequency range $\Delta f_0/\bar{f}_0$ as a function of coupling strength K . Note that for all systems, due to synchronization in the limit of strong coupling the relative frequency range tends to zero. In (B), for all four systems we show the sensitivity $|\chi|(F, \bar{f}_0)$ (driving at the central hair bundle's characteristic frequency \bar{f}_0) of the central hair bundle in the sensitive linear response regime ($F = 0.01$ pN) as a function of coupling strength K . Note that in the limit of large K the results of all systems agree. In (C), we display the quality Q of the central hair bundle's spontaneous oscillations as a function of K . Again, while for $K \approx \bar{K}_{SP}$ differences between the four system can be seen, in the limit of strong coupling the results for all four systems agree. The dashed line in (B) and (C) indicates the passive stiffness \bar{K}_{SP} of the central hair bundle. In (D), we plot the sensitivity of the central hair bundle for the four systems as a function of driving amplitude F . Here we have chosen $K = \bar{K}_{SP} = 0.6$ pN/nm and $f_s = \bar{f}_0$.

frequency of the central hair bundle is $\bar{f}_0 = f_0^{2,14}$. In particular, below we will discuss the relative frequency range which is defined as the ratio $\Delta f_0/\bar{f}_0$. In the case of the cochlea this relative frequency range can be estimated using eq. (4.5) to be on the order of 5%.

In fig. 4.8, we show the statistics of the spontaneous and driven activity of the central hair bundle for different ranges of intrinsic frequencies. Fig. 4.8A shows the relative frequency range $\Delta f_0/\bar{f}_0$ as a function of coupling strength. In the absence of coupling ($K = 0$ pN/nm), Δf_0 equals the intrinsic frequency range of the system. The examples shown correspond to relative intrinsic frequency ranges of 0% (green), 2% (red), 9% (blue) and 18% (yellow). In the limit of large coupling ($K \gg K_{SP}$),

Δf_0 vanishes and all hair bundles are synchronized. For $K \leq \bar{K}_{\text{SP}}$, the frequency range is reduced. A significant frequency gradient, however, remains.

The maximal sensitivity $|\chi|$ in linear response and the quality Q of the central hair bundle's spontaneous oscillations are displayed in fig. 4.8B and C, respectively, as functions of coupling strength K . Deviations from the homogeneous case (green lines) for both quantities occur predominantly when $K \approx \bar{K}_{\text{SP}}$. In the limit of strong coupling, all systems show the same behavior. If K differs by less than an order of magnitude from \bar{K}_{SP} , amplification and frequency tuning are significantly enhanced, while at the same time frequency gradients can be preserved.

The sensitivity as a function of driving amplitude is shown in fig. 4.8D for a coupling strength $K = \bar{K}_{\text{SP}}$. At this coupling strength, sensitivity is significantly enhanced by coupling, while there still exists a range Δf_0 of frequencies of the spontaneous activity in heterogeneous systems. All cases shown exhibit a strong compressive nonlinearity and amplification gain. Increasing the intrinsic frequency range from 0% to 18%, the amplification gain, however, is reduced from about 300 to about 100.

The mammalian cochlea needs to perform well according to at least two criteria. On the one hand, very high sensitivity is desirable. On the other hand, fine frequency resolution, e.g. for speech recognition, needs to be achieved. The results presented in this section indicate that these two aspects could constitute competing requirements. Strong coupling, while enhancing sensitivity, could reduce the ability of the cochlea to resolve a stimulus' frequency content. No coupling, while not changing intrinsic frequency gradients, could render sensitivity too low. Above we have shown that balancing both aspects is possible. Our results suggest that locally adjusting the coupling strength to the passive hair-bundle stiffness, while enhancing sensitivity, would not entirely flatten out frequency profiles. As pointed out in section 4.1, the tectorial membrane is not homogeneous along its length, but from base to apex exhibits a morphological stiffness gradient. Based on data obtained in gerbil [135], the effective coupling strength changes from about $K = 30$ pN/nm at the base to about $K = 3$ pN/nm at the apex. Interestingly, a similar gradient of passive hair-bundle stiffness is observed in the cochlea of the guinea pig. In this species, the passive stiffness was reported to gradually change from about $K_{\text{SP}} = 40$ pN/nm at the base to about $K_{\text{SP}} = 0.5$ pN/nm at the apex [154]. This finding underscores the possibility that coupling strength in the mammalian cochlea could, indeed, be locally adjusted in order to achieve an optimal tradeoff between the two performance criteria of high sensitivity and frequency resolution.

4.6 A mean-field argument

In the previous four sections, we have discussed numerical results showing that elastic coupling of active hair bundles can have a profound effect on their spontaneous and driven dynamics. The observed effects, as for example the almost linear increase

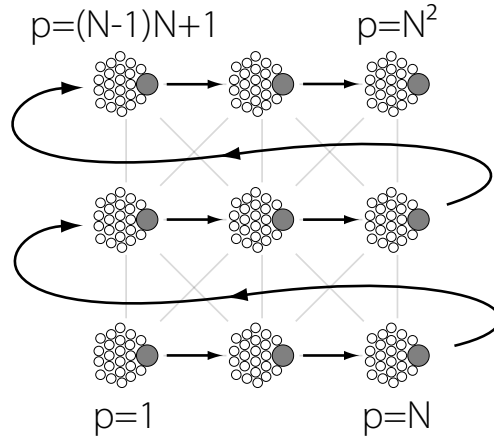


Figure 4.9: Relabeling of hair bundles. Unlike in the previous sections, here we label hair bundles with a single index. Starting from the left lower corner, each row of hair bundles is labeled with a running index, starting from the left. While in no way affecting the coupling geometry or the dynamics of the system, this new labeling will be useful when presenting the results of this section.

of the amplification gain along with system size (see fig. 4.5D), are reminiscent of the effects observed upon reducing the intrinsic fluctuations shaping the dynamics of an isolated hair bundle (see chapter 2). In this section, we will argue that it is indeed by effectively reducing the noise level that elastic coupling enhances hair-bundle performance.

We will consider quadratic systems and open boundary conditions only. The arguments presented, however, can be straightforwardly generalized to non-quadratic systems and periodic boundary conditions, yielding qualitatively similar results.

For the purpose of this section, it is useful to label hair bundles in a different manner as compared to previous sections (see fig. 4.9). Given a system of $N \times N$ coupled hair bundles, we define a deflection vector $\mathbf{x} = (x^p)$, a motor position vector $\mathbf{x}_a = (x_a^p)$, as well as two noise vectors $\boldsymbol{\xi} = (\xi^p)$ and $\boldsymbol{\xi}_a = (\xi_a^p)$, such that for given i, j with $1 \leq i, j \leq N$ we have

$$x^{(i-1)N+j} = X^{i,j}, x_a^{(i-1)N+j} = X_a^{i,j}, \xi^{(i-1)N+j} = \xi^{i,j}, \xi_a^{(i-1)N+j} = \xi_a^{i,j}.$$

We furthermore introduce the average deflection \bar{x} (see fig. 4.10) and the average motor position \bar{x}_a of all hair bundles in the system, i.e.

$$\bar{x} = \frac{1}{N^2} \sum_{p=1}^{N^2} x^p \quad \text{and} \quad \bar{x}_a = \frac{1}{N^2} \sum_{p=1}^{N^2} x_a^p. \quad (4.6)$$

These average positions will also be referred to as mean-field variables or simply as the mean field. The deviation vectors $\boldsymbol{\delta} = (\delta^p)$ of the individual deflections (see fig. 4.10) and $\boldsymbol{\delta}_a = (\delta_a^p)$ of the individual motor positions from the respective

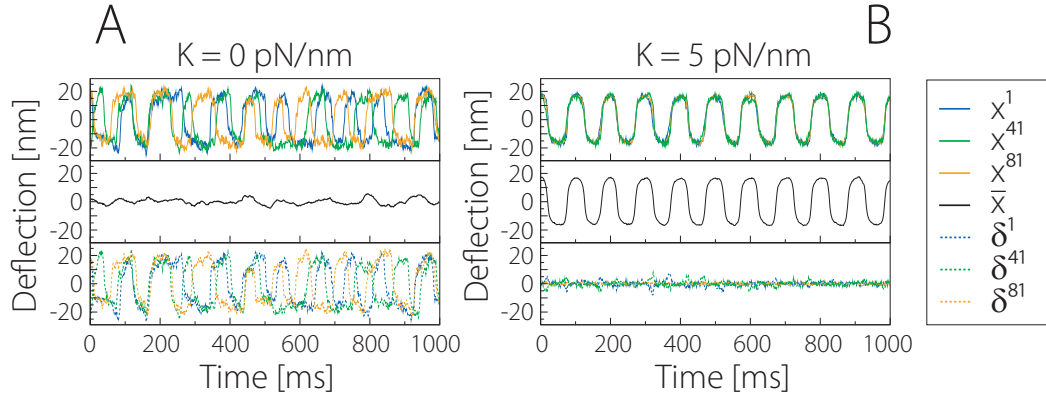


Figure 4.10: Coupling-induced oscillations of the mean field. A 9×9 system was simulated for two coupling strengths, corresponding to no coupling (A, $K = 0$ pN/nm) and the strong coupling regime (B, $K = 5$ pN/nm). In the upper panel we plot trajectories of three hair bundles within the respective system (x^1 (lower left corner), x^{41} (central hair bundle), x^{81} (upper right corner)). As shown in section 4.2, coupling leads to synchronization (see B). In the middle panel we plot the corresponding time course of the respective mean-field variable \bar{x} . Note that in A, with all hair bundles being independent, the mean field only fluctuates mildly about zero. With hair bundles being synchronized, in the strong coupling regime, however, the mean field performs a well-defined oscillation comparable to the oscillations of the individual hair bundles. Note the more regular shape of the oscillation as compared to the individual trajectories shown in A. In the lower panel, we plot the deviations δ^1, δ^{41} , and δ^{81} from the mean field corresponding to the respective traces shown in the upper panel. In A, as the mean field is almost zero, these deviations are large and almost equal the individual trajectories. In the strong coupling regime, deviations in contrast are small compared to the hair bundles' oscillation amplitudes. The dynamics of each hair bundle, in other words, safe of these deviations, largely coincides with the dynamics of the mean field.

mean-field variable are given by

$$\delta^p = x^p - \bar{x} \quad \text{and} \quad \delta_a^p = x_a^p - \bar{x}_a. \quad (4.7)$$

Note that the above definitions imply

$$\sum_{p=1}^{N^2} \delta^p = 0 \quad \text{and} \quad \sum_{p=1}^{N^2} \delta_a^p = 0. \quad (4.8)$$

Assuming that K is chosen sufficiently large, hair bundles do oscillate in near synchrony (see section 4.2). In this strong coupling regime, the mean field variable \bar{x} oscillates in a similar fashion as compared to the individual hair bundles that the system consists of (see fig. 4.10B). The deviations δ^p of individual hair bundle deflections from the mean field value \bar{x} are small versus the oscillation amplitude (see fig. 4.10B). Even though motor variables are not coupled, we will additionally assume that deviations of the individual motor variables δ_a^p from the mean field value \bar{x}_a are likewise small. Under these assumptions, in the following we will derive approximate dynamic equations for the mean-field variables, as well as for the deviation vectors. Later on we will see that, indeed, these assumptions lead to self-consistent results.

To this end, as a first step we linearize the coupling term describing elastic hair bundle interactions in eq. (4.1). Note that typical deflection amplitudes of hair bundles are on the order of several tens of nanometers. The lattice constant, however, which also sets the rest length of the springs mediating the elastic coupling, was chosen to be $d = 50 \mu\text{m}$. It is therefore reasonable to expand coupling forces up to linear order in relative deflections $X^{i+k,j+l} - X^{i,j}$ of interacting hair bundles, leading to

$$-\frac{\partial U(X^{i,j}, x^{i+k,j+l})}{\partial X^{i,j}} \approx \begin{cases} K(X^{i+k,j+l} - X^{i,j}) & \text{for } |k| = 1, l = 0 \\ \frac{1}{2}K(X^{i+k,j+l} - X^{i,j}) & \text{for } |k| = 1, |l| = 1 \\ 0 & \text{for } |k| = 0, |l| \leq 1. \end{cases}$$

In particular, note that vertical springs in this approximation do not add to the elastic interactions induced by coupling and that these forces are independent of the lattice spacing d . Using these linearized coupling forces, the deflection dynamics for a hair bundle in the coupled system reads

$$\lambda \dot{x}^p = f_X(x^p, x_a^p) + K \sum'_{m,n=-1} (1 - \frac{|n|}{2}) |m| (x^{p+nN+m} - x^p) + F_{\text{ext}}(t) + \xi^p(t),$$

where the prime indicates that the sum extends over next-nearest neighbors only.

In order to further facilitate the notation, we introduce the coupling matrix $\mathbf{C} = (c_{pq})$. It is uniquely defined by the requirement that for all p with $1 \leq p \leq N^2$

$$\sum'_{m,n=-1} (1 - \frac{|n|}{2}) |m| (x^{p+nN+m} - x^p) = \sum_{q=1}^{N^2} c_{pq} x^q.$$

In particular, note that \mathbf{C} is symmetric and that

$$\sum_{q=1}^{N^2} c_{pq} = 0 \tag{4.9}$$

for all p with $1 \leq p \leq N^2$. The full dynamics for a hair bundle in the coupled system can thus be written as

$$\lambda \dot{x}^p = f_X(x^p, x_a^p) + K \sum_{q=1}^{N^2} c_{pq} x^q + F_{\text{ext}}(t) + \xi^p(t) \tag{4.10}$$

$$\lambda_a \dot{x}_a^p = f_{X_a}(x^p, x_a^p) + \xi_a^p(t). \tag{4.11}$$

We can approximate these dynamics to linear order in δ^p and δ_a^p as

$$\begin{aligned}
\lambda \dot{x}^p &= f_X(x^p, x_a^p) + K \sum_{q=1}^{N^2} c_{pq} x^q + F_{\text{ext}}(t) + \xi^p(t) \\
&= f_X(\bar{x} + \delta^p, \bar{x}_a + \delta_a^p) + K \sum_{q=1}^{N^2} c_{pq} (\bar{x} + \delta^q) + F_{\text{ext}}(t) + \xi^p(t) \\
&\approx f_X(\bar{x}, \bar{x}_a) + \left. \frac{\partial f_X}{\partial X} \right|_{\bar{x}, \bar{x}_a} \delta^p + \left. \frac{\partial f_X}{\partial X_a} \right|_{\bar{x}, \bar{x}_a} \delta_a^p + K \sum_{q=1}^{N^2} c_{pq} \delta^q + F_{\text{ext}}(t) + \xi^p(t),
\end{aligned} \tag{4.12}$$

and

$$\begin{aligned}
\lambda_a \dot{x}_a^p &= f_{X_a}(x^p, x_a^p) + \xi_a^p(t) \\
&\approx f_{X_a}(\bar{x}, \bar{x}_a) + \left. \frac{\partial f_{X_a}}{\partial X} \right|_{\bar{x}, \bar{x}_a} \delta^p + \left. \frac{\partial f_{X_a}}{\partial X_a} \right|_{\bar{x}, \bar{x}_a} \delta_a^p + \xi_a^p(t),
\end{aligned} \tag{4.13}$$

where in eq. (4.12) we have used eq. (4.9). We can therefore derive the following dynamic equations for the mean field:

$$\begin{aligned}
\lambda \dot{\bar{x}} &= \frac{1}{N^2} \sum_{p=1}^{N^2} \lambda \dot{x}^p \\
&= f_X(\bar{x}, \bar{x}_a) + \left. \frac{\partial f_X}{\partial X} \right|_{\bar{x}, \bar{x}_a} \frac{1}{N^2} \sum_{p=1}^{N^2} \delta^p + \left. \frac{\partial f_X}{\partial X_a} \right|_{\bar{x}, \bar{x}_a} \frac{1}{N^2} \sum_{p=1}^{N^2} \delta_a^p \\
&\quad + \frac{K}{N^2} \sum_{p=1}^{N^2} \sum_{q=1}^{N^2} c_{pq} \delta^q + F_{\text{ext}}(t) + \frac{1}{N^2} \sum_{p=1}^{N^2} \xi^p(t) \\
&= f_X(\bar{x}, \bar{x}_a) + F_{\text{ext}}(t) + \frac{1}{N^2} \sum_{p=1}^{N^2} \xi^p(t),
\end{aligned} \tag{4.14}$$

$$\begin{aligned}
\lambda_a \dot{\bar{x}}_a &= \frac{1}{N^2} \sum_{p=1}^{N^2} \lambda_a \dot{x}_a^p \\
&= f_{X_a}(\bar{x}, \bar{x}_a) + \frac{1}{N^2} \sum_{p=1}^{N^2} \xi_a^p(t).
\end{aligned} \tag{4.15}$$

Here, we have used the symmetry of the coupling matrix \mathbf{C} and the properties stated in eq. (4.8) and eq. (4.9). Note that

$$\left\langle \frac{1}{N^2} \sum_{q=1}^{N^2} \xi^q(t) \frac{1}{N^2} \sum_{p=1}^{N^2} \xi^p(t') \right\rangle = \frac{1}{N^4} \sum_{p=1}^{N^2} \langle \xi^p(t) \xi^p(t') \rangle = \frac{2\lambda k_B T}{N^2} \delta(t - t'),$$

as the white noise terms ξ^p are pairwise uncorrelated. A similar argument holds true for the sum of noise sources appearing in the equation for \bar{x}_a . As the sum of Gaussian variables is again Gaussian, we can therefore substitute the sums of noise sources appearing in eq. (4.14) and eq. (4.15) by two effective white noise terms $\sqrt{1/N^2}\tilde{\xi}(t)$ and $\sqrt{1/N^2}\tilde{\xi}_a(t)$ with respective autocorrelation functions $\langle \tilde{\xi}(t)\tilde{\xi}(t') \rangle = 2\lambda k_B T \delta(t-t')$ and $\langle \tilde{\xi}_a(t)\tilde{\xi}_a(t') \rangle = 2\lambda_a k_B T_a \delta(t-t')$. The equations for the mean field accordingly reduce to

$$\lambda \dot{\bar{x}} = f_X(\bar{x}, \bar{x}_a) + F_{\text{ext}}(t) + \sqrt{\frac{1}{N^2}} \tilde{\xi}(t), \quad (4.16)$$

$$\lambda_a \dot{\bar{x}}_a = f_{X_a}(\bar{x}, \bar{x}_a) + \sqrt{\frac{1}{N^2}} \tilde{\xi}_a(t). \quad (4.17)$$

In other words, the mean field behaves as a single hair bundle, albeit with reduced noise (cf. fig. 4.10B). Note that the strength of fluctuations which drive mean field dynamics is inversely proportional to the total number N^2 of hair bundles in the system.

We now turn to the deviations δ^p and δ_a^p of the individual hair bundles from the mean field. Their dynamics are governed by the following equations:

$$\begin{aligned} \lambda \dot{\delta}^p &= \lambda \dot{x}^p - \lambda \dot{\bar{x}} \\ &= \left. \frac{\partial f_X}{\partial X} \right|_{\bar{x}, \bar{x}_a} \delta^p + \left. \frac{\partial f_X}{\partial X_a} \right|_{\bar{x}, \bar{x}_a} \delta_a^p + K \sum_{q=1}^{N^2} c_{pq} \delta^q + \xi^p(t) - \frac{1}{N^2} \sum_{q=1}^{N^2} \xi^q(t), \end{aligned} \quad (4.18)$$

$$\begin{aligned} \lambda_a \dot{\delta}_a^p &= \lambda_a \dot{x}_a^p - \lambda_a \dot{\bar{x}}_a \\ &= \left. \frac{\partial f_{X_a}}{\partial X} \right|_{\bar{x}, \bar{x}_a} \delta^p + \left. \frac{\partial f_{X_a}}{\partial X_a} \right|_{\bar{x}, \bar{x}_a} \delta_a^p + \xi_a^p(t) - \frac{1}{N^2} \sum_{q=1}^{N^2} \xi_a^q(t). \end{aligned} \quad (4.19)$$

The latter can be written conveniently in matrix form as

$$\begin{pmatrix} \lambda \dot{\boldsymbol{\delta}} \\ \lambda_a \dot{\boldsymbol{\delta}}_a \end{pmatrix} = \begin{pmatrix} K\mathbf{C} + \mathbf{B}_{11} & \mathbf{B}_{12} \\ \mathbf{B}_{21} & \mathbf{B}_{22} \end{pmatrix} \begin{pmatrix} \boldsymbol{\delta} \\ \boldsymbol{\delta}_a \end{pmatrix} + \begin{pmatrix} \mathbf{D} & \mathbf{0} \\ \mathbf{0} & \mathbf{D} \end{pmatrix} \begin{pmatrix} \boldsymbol{\xi}(t) \\ \boldsymbol{\xi}_a(t) \end{pmatrix}. \quad (4.20)$$

Here we have defined the shorthand

$$\begin{aligned} \mathbf{B}_{11} &= \left. \frac{\partial f_X}{\partial X} \right|_{\bar{x}, \bar{x}_a} \mathbb{1}, & \mathbf{B}_{12} &= \left. \frac{\partial f_X}{\partial X_a} \right|_{\bar{x}, \bar{x}_a} \mathbb{1}, \\ \mathbf{B}_{21} &= \left. \frac{\partial f_{X_a}}{\partial X} \right|_{\bar{x}, \bar{x}_a} \mathbb{1}, & \mathbf{B}_{22} &= \left. \frac{\partial f_{X_a}}{\partial X_a} \right|_{\bar{x}, \bar{x}_a} \mathbb{1}, \end{aligned} \quad (4.21)$$

where $\mathbb{1}$ denotes the $N^2 \times N^2$ identity matrix. Furthermore, the $N^2 \times N^2$ matrix $\mathbf{D} = (d_{pq})$ is given by

$$d_{pq} = \begin{cases} 1 - \frac{1}{N^2} & \text{for } p = q \\ -\frac{1}{N^2} & \text{for } p \neq q. \end{cases}$$

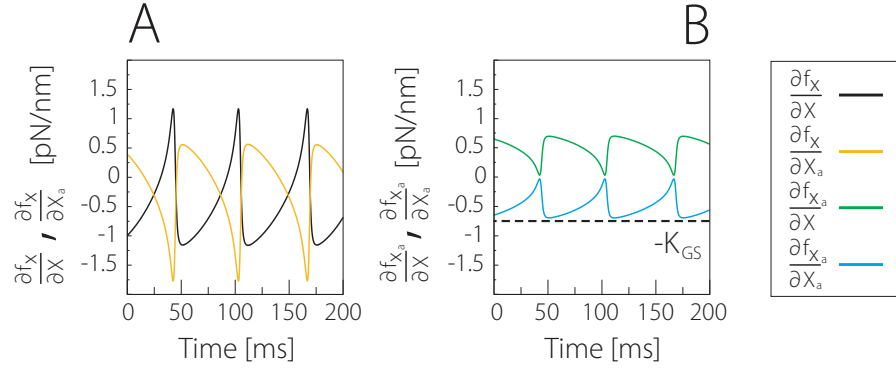


Figure 4.11: Derivatives of the state-dependent forces f_X and f_{X_a} acting on the deflection and motor variable, respectively. We plot for a hair bundle operating at OP2, in the absence of noise, in (A) the derivatives $\frac{\partial f_X}{\partial X}$, $\frac{\partial f_{X_a}}{\partial X_a}$, and in (B) the derivatives $\frac{\partial f_{X_a}}{\partial X}$, $\frac{\partial f_{X_a}}{\partial X_a}$ as solid lines. Note that these derivatives are all bounded and oscillate with twice the frequency (about 16Hz) of the hair bundle's deflection X (about 8 Hz). In (B), we also indicate as a dashed line the minimum value, namely $-K_{GS}$, which $\frac{\partial f_{X_a}}{\partial X_a}$ can attain (for X , X_a such that $P_o(X, X_a) = 0$ or 1).

According to eq. (4.20), the dynamics of the deviation vectors δ and δ_a obey a $2N^2 \times 2N^2$ -dimensional Ornstein-Uhlenbeck process with time-dependent coefficients [49]. Note, however, that all derivatives defining the matrices \mathbf{B}_{ij} for given deflection X and motor position X_a solely depend on the open probability $P_o(\bar{x}, \bar{x}_a)$. As this dependence is continuous on the closed interval $[0, 1]$, the respective derivatives can only attain values which are bounded from below and above (see fig. 4.11). In particular, the respective bounds are independent of the coupling strength K . In the limit of strong coupling, the influence of elastic forces due to the coupling term $K\mathbf{C} \sim K$ can therefore be assumed to dominate the dynamics of δ . In this regime, we can in other words neglect the influence of the mean field and effectively set

$$\mathbf{B}_{11} = \mathbf{B}_{12} = 0.$$

Note that this choice decouples the dynamics of δ_a and δ , yielding

$$\lambda \dot{\delta} = K\mathbf{C}\delta + \mathbf{D}\xi(t).$$

Both \mathbf{C} and \mathbf{D} have a zero eigenvalue. The corresponding eigenspace in both cases is one dimensional and is spanned by the same eigenvector $\mathbf{v} = (1, \dots, 1)$. The dynamics of δ therefore in effect are confined to a $N^2 - 1$ -dimensional subspace. An application of the Gershgorin circle theorem [51] shows that all eigenvalues of \mathbf{C} lie in the closed interval $[-8, 0]$. As the real and symmetric matrix \mathbf{C} is diagonalizable and is of rank $N^2 - 1$, we can further conclude that all eigenvalues, apart from one, are strictly smaller than zero. The latter assures that a stationary distribution for δ exists and that $\langle \delta \rangle = 0$. The stationary covariance matrix

$$\sigma = (\langle \delta^p \delta^q \rangle)_{1 \leq p, q \leq N^2}$$

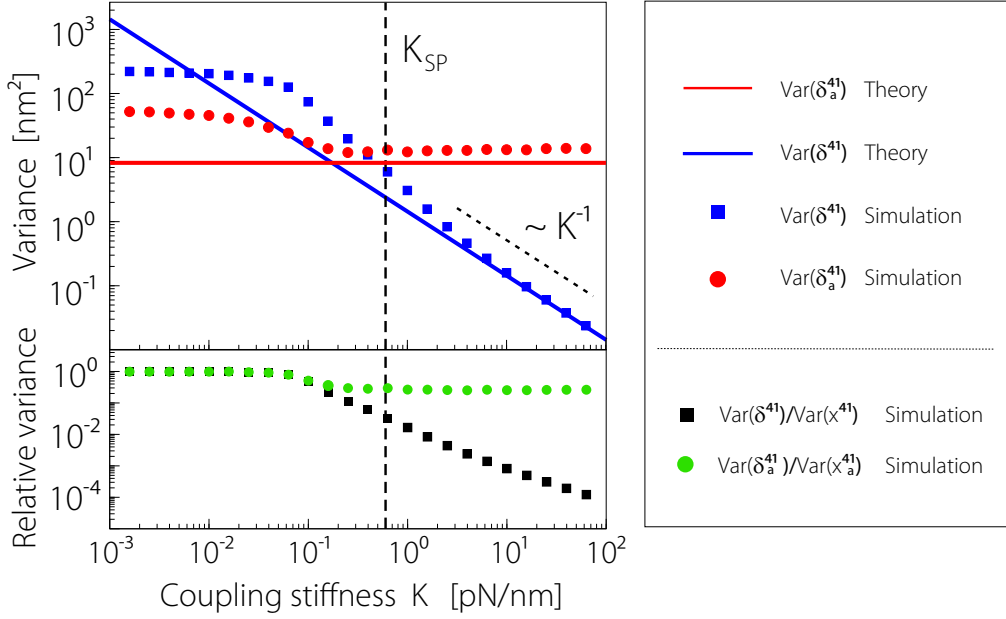


Figure 4.12: Deviations from the mean field. For the central hair bundle in a 9×9 system, we plot in the upper panel the variances of its deviations $\delta^{41} = x^{41} - \bar{x}$ and $\delta_a^{41} = x_a^{41} - \bar{x}_a$ from the respective mean-field variables as a function of coupling stiffness K . We compare simulation results (blue squares and red discs) to our theoretical results (solution of eq. (4.22) for $\text{Var}(\delta^{41})$; the value stated in eq. (4.25) for $\text{Var}(\delta_a^{41})$). Note that indeed $\text{Var}(\delta^{41}) \sim k_B T / K$ for large coupling strengths K . In contrast, $\text{Var}(\delta_a^{41})$ is not tending to zero and is in the large coupling regime bounded from below by $k_B T_a / K_{\text{GS}}$. For comparison we also indicate as a dashed vertical line the pivotal stiffness K_{SP} of the hair bundle. In the lower panel we plot the relative variances of the deviations δ^{41} and δ_a^{41} with respect to the respective variances of the hair bundle variable x^{41} and x_a^{41} . Note that, indeed, for the deflection variable this ratio tends to zero. For a coupling strength $K \gtrsim K_{\text{SP}}$ it is already less than 10%.

can be shown to obey [49]

$$(\mathbf{C}\boldsymbol{\sigma} + \boldsymbol{\sigma}\mathbf{C}) = -\frac{2k_B T}{K}\mathbf{D}. \quad (4.22)$$

Eq. (4.22) implies (see fig. 4.12)

$$\boldsymbol{\sigma} \sim \frac{k_B T}{K}, \quad (4.23)$$

so that in particular

$$\lim_{K \rightarrow \infty} \langle \delta^p \delta^p \rangle = 0. \quad (4.24)$$

Concerning the deviations the motor positions δ_a^p , note that in the limit of large N we can assume that $\mathbf{D} \approx \mathbb{1}$. Furthermore, neglecting the influence of $\boldsymbol{\delta}$, which according to eq. (4.24) in the limit of large coupling strength is reasonable, the

dynamics of each δ_a^p are given in terms of a one dimensional Ornstein-Uhlenbeck process as

$$\lambda_a \delta_a^p = -k \delta_a^p + \xi_a^p(t),$$

where we have used the notation $k = -\frac{\partial f_{X_a}}{\partial X_a}|_{\bar{x}, \bar{x}_a}$. The effective stiffness k still depends on the dynamics of the mean field. Its range of possible values, however, is restricted to $0 < k < K_{GS}$ (see fig. 4.11). In order to estimate a lower bound for the variance of δ_a^p , we thus set $k = K_{GS}$. This leads to

$$\langle \delta_a^p \delta_a^p \rangle = \frac{k_B T_a}{K_{GS}} \approx 8.3 \text{ nm}^2, \quad (4.25)$$

which is in reasonable agreement with our simulation results (see fig. 4.12).

Most importantly, the above shows that in a system of strongly coupled hair bundles the variances of all deviations δ^p from the mean field tend to zero. The statistics of spontaneous and driven hair-bundle oscillations as observed in the deflection variables x^p , in this strong coupling regime are thus, indeed, expected to resemble the respective measures for the mean-field variable \bar{x} . The mean field in turn was shown to behave as a single hair bundle with reduced noise. In this sense, elastic coupling brings about an effective noise reduction. In particular, note that in the presence of an external signal the mean field will respond more sensitively as compared to a single uncoupled hair bundle. As the external stimulus is not entering the dynamics of the deviations, elastically coupled hair bundles in the strong coupling regime are expected to exhibit higher amplification gains.

4.7 Summary

In the framework of the biophysical description of stochastic hair-bundle dynamics discussed in chapter 2, in this chapter we have presented results as to the expected effects of an elastic coupling on hair-bundle dynamics. We have argued that by effectively reducing intrinsic fluctuations, elastic coupling of suitable strength enhances the quality of spontaneous oscillations as well as the tuning and the amplification gain of the hair bundles in a coupled system. In our simulations, these beneficial effects were observed in homogeneous systems as well as in systems with built-in frequency gradients. In this case, when the coupling strength was close to the passive stiffness of the hair bundles in the system, amplification was enhanced while frequency gradients were maintained.

In many inner ear organs elastic coupling between hair bundles is implemented by means of gelatinous membranes. There is no agreement as to the exact elastic moduli describing the material properties of these membranes (cf. e.g. [58] and [135]). The available data, however, indicate that coupling of suitable strength is realized *in vivo*. Inner ear organs therefore might make use of coupling-induced noise reduction in order to boost their responsiveness to sensory stimuli.

Chapter 5

The hair bundle and its cyber clones - A hybrid experiment

In the last chapter, we have argued that on theoretical grounds it is to be expected that the elastic coupling of already a small number of hair bundles can bring about a substantial reduction of the noise impinging on the individual hair bundles within the group. In our simulations, hair bundles within such oscillatory modules were found to exhibit spontaneous oscillations of higher quality as well as higher amplification gains than isolated hair bundles.

In this chapter, we will present results of an experimental study for which we have interfaced stochastic simulations of noisy hair-bundle motility as described by eq. (1.10) and eq. (1.11) with micromanipulation experiments performed on single hair bundles from the sacculus of the bullfrog. By means of a dynamic force clamp we were able to emulate a situation in which a biological hair bundle under study was elastically coupled to two neighboring hair bundles of similar characteristics. Here we write “emulate”, as the neighboring hair bundles only existed virtually as stochastic simulations of hair-bundle dynamics. The results of this hybrid experiment underscore the findings presented in the last chapter and constitute strong evidence for the hair bundle’s ability to profitably integrate into a multicellular system of elastically coupled hair bundles.

5.1 Dynamic force clamp

In this section, we will introduce the design of the hybrid experiment. We will deal with the basic procedures first. As these are well established [111], some minor technical details will be omitted. Instead, we will concentrate on the specifics of the experiment at hand. We will also present two results which serve as a consistency check of the implemented setup.

An excised preparation of the sacculus of the American bullfrog (*Rana catesbeiana*) was mounted on a two-compartment chamber. Due to the specific design of this microscope slide, the basal side of the preparation could be bathed in standard

saline, while hair bundles projected into artificial endolymph. The otolithic membrane was removed. Accordingly, hair bundles were neither coupled to the otolithic membrane, nor were they elastically coupled to each other. Under these conditions hair bundles routinely display noisy spontaneous oscillations [111]. A hair bundle's deflection X could be quantified by means of projecting a magnified image of its tip onto a pair of photodiodes. A difference in the illumination of the two diodes induces a current. Movements of the hair bundle lead to a change in this relative illumination. The effected change in current output over the physiologically relevant range of deflections depends linearly on the distance moved by the hair bundle. After calibration, the deflection X of the hair bundle could be inferred from the photodiodes' current output with subnanometer precision. Positive deflections by convention correspond to movements of the hair bundle in the direction of the kinocilium.

Flexible glass fibers were employed in order to apply prescribed forces to the hair bundle (see also fig. 5.1B). With a fiber's tip being attached to the kinociliary bulb of the hair bundle, the position Δ of the base of the fiber could be adjusted by means of a piezoelectric actuator. The utilized glass fibers over the relevant range of deflections acted as linear springs with stiffness K_f . Given a deflection X of the hair bundle and a position Δ of the fiber's base, a force

$$F = K_f(\Delta - X)$$

was thus exerted at the hair bundle's tip. The fiber was firmly attached to the kinocilium, such that pulling and pushing forces could be applied. The stiffness K_f of a given fiber was determined prior to each measurement by means of spectral analysis of the fluctuating motion of the tip of the detached fiber in the endolymph surrounding the hair bundles.

Note that given this experimental apparatus it was only possible to observe and interact with a single hair bundle at a time.

Now imagine a hair bundle which is coupled by means of linear springs to two flanking neighbors of similar characteristics (see fig. 5.1A). In such a situation, in each instant of time the hair bundle experiences a coupling induced force $F_K = F_1 + F_2$, where F_1 and F_2 are due to the elastic linkages connecting the hair bundle to its neighbor to the left and to the right, respectively. At the same time, reaction forces $-F_1$ and $-F_2$ are exerted on the flanking hair bundles. Here F_1 , F_2 and F_K depend on the deflections X_1 , X and X_2 of the three hair bundles as well as on the spring constant K . The latter will also be referred to as the coupling strength or coupling stiffness. An external stimulus corresponding to a force F_{ext} might additionally be present, acting on all hair bundles within the group.

At present it is technically impractical to recreate *in vitro* a setup as just described. Therefore, instead of elastically coupling three biological hair bundles, a setup was implemented in which the two flanking hair bundles were effectively substituted by what will be referred to as "cyber clones", i.e. real-time stochastic simulations of active hair bundle motility (see fig. 5.1B).

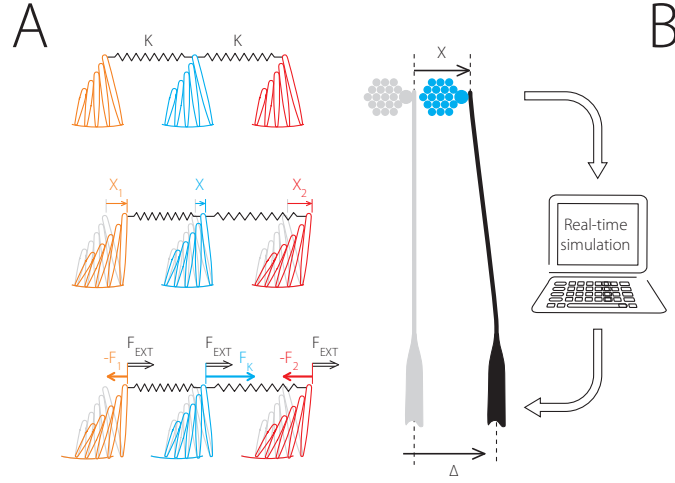


Figure 5.1: Coupling a hair bundle to two cyber clones by dynamic force clamp. (A) Schematic representation of a system of three coupled hair bundles. A hair bundle (blue) is connected to one neighbor on each side (orange and red) by identical springs of stiffness K . The positions of the hair bundles (X_1 , X , and X_2) oscillate spontaneously. Relative movements of adjacent hair bundles yield elastic forces ($-F_1$, $F_K = F_1 + F_2$, and $-F_2$). All three hair bundles experience the same external force F_{ext} . (B) Experimental realization. A stimulus fiber was attached to the hair bundle's tip. From each measured hair-bundle position X , the position Δ of the fiber's base was dynamically actuated to apply the force $F = F_{\text{ext}} + F_K$ depicted in (A) for the central hair bundle. This force was calculated in real time from a stochastic computer simulation which emulated the behavior of the two neighbors, called cyber clones. The cyber clones, in other words, were substituted for the two hair bundles at X_1 and X_2 in (A).

More specifically, during each experiment the position X of the hair bundle was measured at discrete times $n\Delta t$ with a sampling rate $1/\Delta t$ between 2.5 and 10 kHz (see fig. 5.2A). Simultaneously, two simulations ($i = 1, 2$) of hair-bundle dynamics were performed in real time according to

$$\dot{X}_i = \dot{X}_{i,\text{DET}} - F_i(t) + F_{\text{ext}}(t) + \xi_i(t) \quad (5.1)$$

$$\dot{X}_{a,i} = \dot{X}_{a,i,\text{DET}} + \xi_{a,i}(t), \quad (5.2)$$

where

$$\dot{X}_{i,\text{DET}} = -K_{\text{GS}}(X_i - X_{a,i} - DP_{o,i}) - K_{\text{SP}}X \quad (5.3)$$

$$\dot{X}_{a,i,\text{DET}} = K_{\text{GS}}(X_i - X_{a,i} - DP_{o,i}) - F_{\text{max}}(1 - SP_{o,i}) \quad (5.4)$$

defining at each time $n\Delta t$ the positions X_1 and X_2 of two cyber clones (see fig. 5.2B). Apart from the coupling term F_i specified below, eq. (5.1) and eq. (5.2) are identical to the hair bundle description presented in chapter 1.4.3. The Gaussian white noise terms ξ_i and $\xi_{a,i}$ were assumed to be pairwise independent. In each experiment, parameters in the above description were chosen in order to render the cyber clones having similar characteristics as the hair bundle under study. We will elaborate on this point in the next section.

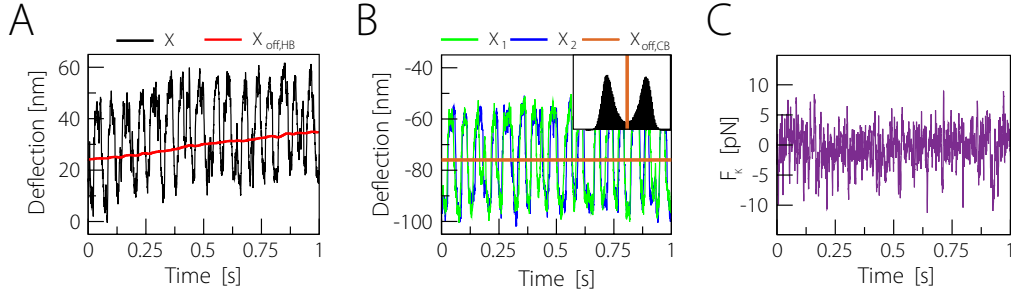


Figure 5.2: Coupling a hair bundle to two cyber clones. All data shown were recorded during a single experiment with $K = 0.2$ pN/nm. (A) Deflection $X(t)$ of the hair bundle (black) shown as function of time. A small drift can be seen. Accordingly, the offset position $X_{\text{off,HB}}$ (red) changes over time. (B) Deflections $X_1(t)$ and $X_2(t)$ plotted as a function of time for those cyber clones the hair bundle shown in (A) was coupled to. Also indicated is the constant offset position $X_{\text{off,CB}}$ (orange). In the inset, a histogram of cyber clone deflections in the absence of coupling is shown. The offset position $X_{\text{off,CB}}$, which is defined as the local minimum between the two peaks, is marked by a vertical line (orange). (C) We show the coupling force F_K exerted on the hair bundle as calculated from the trajectories and offsets in (A) and (B).

In line with the intention of emulating a situation in which the hair bundle was elastically coupled to two neighbors by means of springs with stiffness K , at each time $n\Delta t$ coupling forces F_i defined as

$$F_i = -K(X - X_i - X_{\text{off}})$$

were calculated. Note that there are slow drifts present in most preparations (see fig. 5.2A). Also, the positions of cyber clones are not oscillating about a zero mean position, i.e. $\langle X_i(t) \rangle \neq 0$ for $i = 1, 2$ (see fig. 5.2B). In order to compensate for these effects, differences in deflections were measured with respect to an offset position $X_{\text{off}} = X_{\text{off,HB}} + X_{\text{off,CB}}$. Here $X_{\text{off,HB}}$ at each time $n\Delta t$ was estimated as the average position of the hair bundle over the last second of data acquisition (see fig. 5.2A). $X_{\text{off,CB}}$ was defined as the position of the minimum in the distribution of positions of the cyber clones in the absence of coupling (see fig. 5.2B and inset). Thus $X_{\text{off,CB}}$ corresponded to a deflection halfway between the open and closed state of the cyber clone. As cyber clones with mostly symmetric oscillations were chosen during the experiments, $X_{\text{off,CB}}$ was also close to the average position $\langle X_i(t) \rangle$ of the cyber clones.

A total force $F = F_K + F_{\text{ext}}$ with $F_K = F_1 + F_2$ (see fig. 5.2C) was then applied at the hair bundle's tip. This was achieved by moving the base of the attached glass fiber (see fig. 5.1B) of known stiffness K_f to the position

$$\Delta = \frac{F}{K_f} + X.$$

Note that in order to study the influence of coupling on spontaneous oscillations, also the case $F_{\text{ext}} = 0$ was considered. At the same time, the forces $-F_i + F_{\text{ext}}$

were included in the simulations of the two cyber clones. The positions of the cyber clones at time $(n + 1)\Delta t$ were updated according to a Euler scheme as

$$\begin{aligned} X_i((n + 1)\Delta t) &= X_i(n\Delta t) + \left(\dot{X}_{i,\text{DET}} - F_i(t) + F_{\text{ext}} \right) \Delta t + x_{i,n} \sqrt{2k_B T \lambda \Delta t} \\ X_{a,i}((n + 1)\Delta t) &= X_{a,i}(n\Delta t) + \dot{X}_{a,i,\text{DET}} \Delta t + x_{a,i,n} \sqrt{2k_B T_a \lambda_a \Delta t}, \end{aligned}$$

where $x_{i,n}$ and $x_{a,i,n}$ were normally distributed random numbers with zero mean and unit variance.

Note that by applying the above feedback procedure at each consecutive instant $n\Delta t$, during the experiment the hair bundle and the cyber clones in real time were dynamically influencing each other's behavior. In the remainder of this section, we will discuss two results that can be viewed as controls of the implemented setup.

In the absence of coupling, i.e. $K = 0$ pN/nm, the attached glass fiber was supposed not to exert any force on the hair bundle. By definition $F_K = 0$ pN at all times. In other words, the fiber's base needed to follow the movements of the hair bundle faithfully. We recorded spontaneous hair bundle movements under the following three conditions and compared the corresponding power spectral densities: (i) a free-standing hair bundle, (ii) the same hair bundle with an attached glass fiber with a fixed base, (iii) the same hair bundle with an attached glass fiber whose base was dynamically adjusted according to the described feedback procedure with $K = 0$ pN/nm. Attaching a glass fiber to its tip poses an elastic load on the hair bundle. In accordance with previous results [111], such a load effected an increase of the oscillation frequency and a reduction of the overall oscillation amplitude. When the feedback was applied, however, the resulting oscillations were very similar to the ones performed in the absence of the fiber. We conclude that the attached fiber for vanishing coupling strength was, indeed, not interfering with the dynamics of the hair bundle.

We also checked that the finite discretization used to integrate cyber clones is not expected to alter the outcome of the experiment. We present results concerning this question in Appendix A.

5.2 Cyber clones

In the last section, we have introduced the dynamic force clamp which during our hybrid experiments was used to couple a given hair bundle to two cyber clones. That way a situation was emulated in which the hair bundle was elastically coupled to two neighboring hair bundles. In this section, we will deal with the question as to how parameters in each experiment were chosen in the physical description used to generate the two cyber clones.

At the start of each experiment, several statistics of the spontaneous oscillations of the hair bundle under study were quantified. When $F_{\text{ext}} \neq 0$, also the driven activity of the hair bundle was characterized. By recording its spontaneous oscillations, the

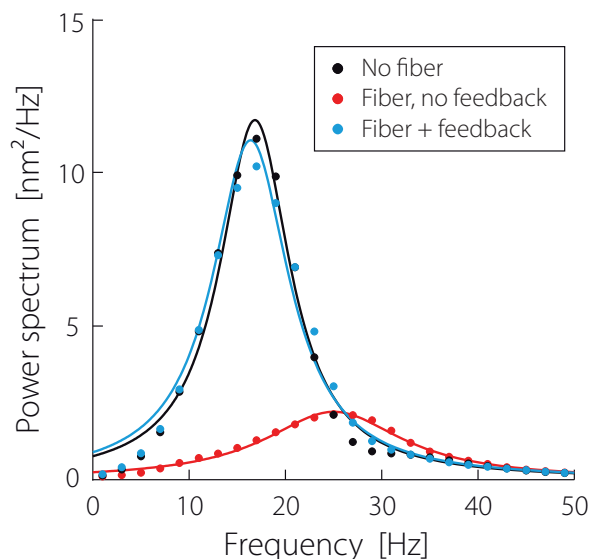


Figure 5.3: Control of the dynamic force clamp with $K = 0$ pN/nm. We show power spectral densities of the same hair bundle under three different conditions: (i) no fiber attached (black), (ii) with a fiber attached whose base was fixed (red), and (iii) with a fiber attached whose base was moved according to the implemented feedback with $K = 0$ pN/nm (blue). While the power spectrum of the hair bundle was significantly altered when attached to a glass fiber with a static base, applying the feedback eliminated the effect of the fiber on hair-bundle dynamics.

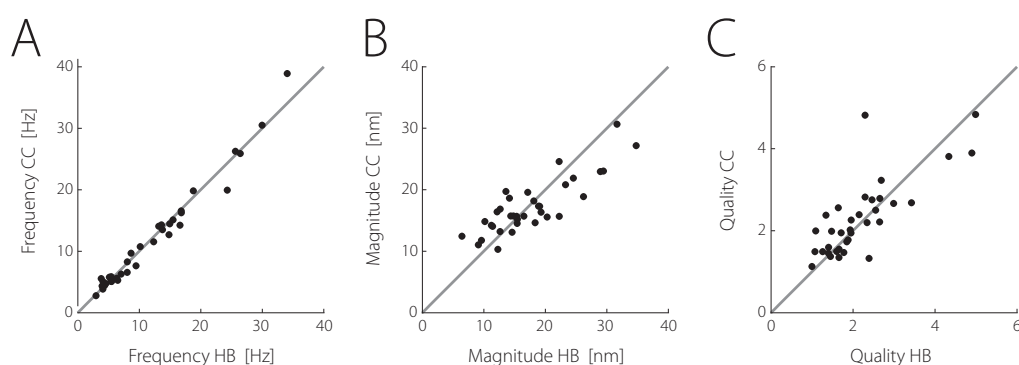


Figure 5.4: Matching cyber clones (CC) to observed hair bundles (HB). In (A) the characteristic frequency, in (B) the root-mean-squared amplitude, and in (C) the quality of spontaneous oscillations is shown for the 33 cyber clones used in experiments as a function of the respective value for the hair bundle that these cyber clones were supposed to mimic. Perfect matches in (A)-(C) correspond to points on the grey lines of slope unity going through the respective origins.

power spectral density $S(\nu)$ was determined. Fitting with a Lorentzian function as given in eq. (2.4) yielded the characteristic frequency ν_0 , the root-mean-squared amplitude A_{RMS} , and the quality factor of the noisy oscillation $Q = \nu_0/\Delta\nu$ (see section 2.1). Here $\Delta\nu$ is the half-width of the spectral peak at the characteristic frequency. When $F_{\text{ext}} \neq 0$, the response of the hair bundle to a periodic driving $F_{\text{ext}}(t) = F_0 \sin(2\pi\nu_0 t)$ applied at its tip was measured in terms of the sensitivity $|\chi|(F_0, \nu_0) = |X_\nu/F_\nu|$ (see section 2.2). Here X_ν and F_ν are the Fourier amplitudes of hair-bundle motion and driving force at the frequency of stimulation, respectively. The sensitivity was quantified in the sensitive linear response regime for weak driving ($F_0 \approx 0.5\text{pN}$), as well as in the linear response regime for strong driving ($F_0 \approx 50\text{pN}$). In this way, the gain of the hair bundle, defined as the ratio between these two values, could be determined.

Given the above characteristics of the observed hair bundle, a set of parameters was determined to produce stochastic simulations that closely matched the properties of the observed hair bundle, namely its spectrum of spontaneous oscillations (see fig. 5.4) and, when $F_{\text{ext}} \neq 0$, its nonlinear response function to sinusoidal stimuli (not shown). In order to achieve a reasonable match within about 5-10 minutes of experimentation time, we developed two complementary strategies. First, we made use of a lookup table that listed approximately 10,000 virtual hair bundles for which we knew the quality factor, the frequency, and the root-mean-squared magnitude of spontaneous oscillations, respectively within a range of 1-5, 5-50 Hz, and 10-20 nm. This table was created by exploring a restricted region of parameter space (see table 5.1) and running stochastic simulations. A cyber bundle that closely matched the properties of the hair bundle could then be selected from the list and serve as cyber clone. The solution was not unique and several sets of parameters could yield comparable results. Second, we finely tuned standard parameters (see OP2 in table 1.1) that yield typical spontaneous oscillations to optimize the fit between hair-bundle and cyber-clone dynamics. For this purpose, an interactive graphic interface was developed that allowed for the efficient generation and analysis of stochastic simulations within a few seconds. Applying an informed trial-and-error strategy, several parameters were varied until a close match between cyber clones and hair bundle was achieved. In particular, the frequency of cyber bundles could be adjusted at will by a uniform rescaling of the two friction coefficients λ and λ_a (see also section 5.6). The dependence of the remaining characteristics on parameter values was less accessible.

5.3 Synchronization and increased phase coherence

In a first set of experiments, we investigated how coupling influenced the statistics of the three oscillators' spontaneous activity. In other words, during these experiments we chose $F_{\text{ext}} = 0$. While in the absence of coupling ($K = 0 \text{ pN/nm}$), the oscillatory movements performed by the hair bundle and the two cyber clones were pairwise

Parameter	Definition	Value
λ	Friction coefficient of the hair bundle	0.6-5.3 $\mu\text{N}\cdot\text{s}\cdot\text{m}^{-1}$
λ_a	Friction coefficient of adaptation motors	1.4-21.9 $\mu\text{N}\cdot\text{s}\cdot\text{m}^{-1}$
K_{GS}	Combined gating-spring stiffness	0.37-0.83 $\text{mN}\cdot\text{m}^{-1}$
K_{SP}	Combined stiffness of stereociliary pivots	0.08-0.70 $\text{mN}\cdot\text{m}^{-1}$
D	Gating-swing of a transduction channel	51-71 nm
F_{max}	Maximal motor force	37-70 pN
S	Feedback strength	0.29-1.06

Table 5.1: Table of parameters that were varied in order to generate cyber clones with suitable characteristics. In the rightmost column minimal and maximal values for the respective parameter are given.

uncorrelated (see fig. 5.5A, top), with increasing coupling strength, they became more and more correlated. Under strong coupling ($K = 0.4$ pN/nm) near complete synchronization was observed (see fig. 5.5A, bottom). We quantified the onset of synchronization by means of cross-correlation coefficients $C_{i,j}$ ($i = \text{HB}, 1, 2$ and $i \neq j$), defined as

$$C_{i,j} = \frac{\langle (X_i - \langle X_i \rangle)(X_j - \langle X_j \rangle) \rangle}{\sqrt{\text{Var}(X_i)\text{Var}(X_j)}},$$

where $\text{Var}(\cdot)$ denotes the variance of the respective quantity. As a function of coupling strength, a smooth transition from uncorrelated oscillations ($C_{i,j} = 0$ at $K = 0$ pN/nm) to near complete synchronization ($C_{i,j} > 0.85$ for $K \geq 0.4$ pN/nm) was found (see fig. 5.5B). Note that for all coupling strengths the cross-correlation coefficient measured for the two cyber clones, i.e. $C_{1,2}$, was smaller than the corresponding one measured for the hair bundle and any of the two cyber clones, i.e. $C_{\text{HB},1}$ and $C_{\text{HB},2}$. This was to be expected, as the two flanking cyber clones did not influence each other's dynamics directly, but only via their mutual interaction with the hair bundle.

Spontaneous oscillations of the hair bundle and of the two cyber clones under coupling also became more regular, as evidenced by a sharpening of the spectral peak at the characteristic frequency of the oscillation (see fig. 5.6A and B, top). The phase coherence of spontaneous oscillations was quantified in terms of the quality factor Q (see section 2.1). When increasing the coupling strength from $K = 0$ pN/nm to $K = 0.4$ pN/nm, the quality of spontaneous oscillations increased until it saturated at about twice its initial value (see fig. 5.6A and B, bottom). This effect was observed for both the hair bundle and the two cyber clones. We performed pure computer simulations of three coupled cyber clones for the 33 parameter sets used in experiments to describe cyber clones. The results obtained were in quantitative agreement with the findings made in experiments (see fig. 5.6A and B, bottom).

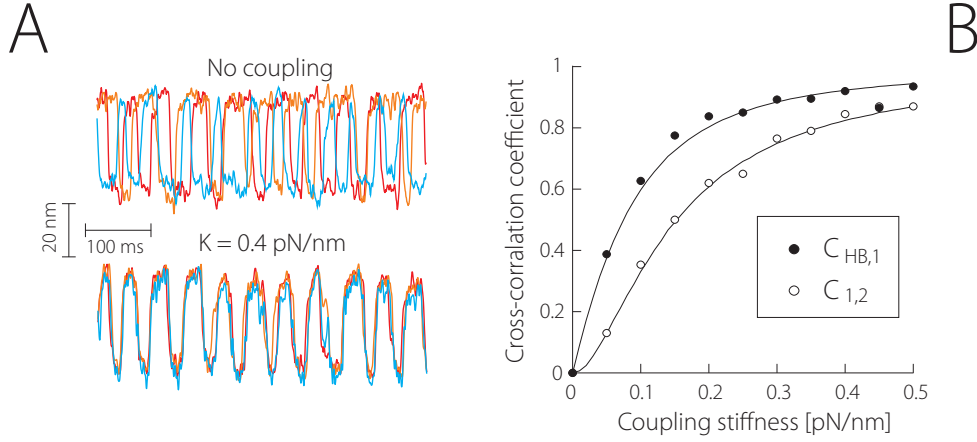


Figure 5.5: Coupling-induced synchronization. (A) Example trajectories of a hair bundle (blue) and the two cyber clones (red and orange) it was coupled two. In the absence of coupling (top, $K = 0$ pN/nm) the movements of the three oscillators were uncorrelated. Under strong coupling (bottom, $K = 0.4$ pN/nm) near complete synchronization was found. (B) Cross-correlation coefficients $C_{HB,1}$ (black discs) and $C_{1,2}$ (open circles) as a function of coupling strength. With increasing coupling stiffness, gradual synchronization was observed. Note that $C_{1,2}$ for all K is smaller than $C_{HB,1}$. Solid lines correspond to results obtained in pure computer simulations of three coupled cyber clones. Cyber-clone parameters in these simulations were the same as during the experiment shown. Data in (A) and (B) of the same cell.

5.4 Enhancement of mechanical amplification

In a second set of experiments, we characterized the response of the hair bundle to periodic stimuli. More precisely, an external force $F_{\text{ext}}(t) = F_0 \sin 2\pi\nu t$ was applied to the hair bundle and the two cyber clones in addition to the coupling forces F_K and $-F_i$, respectively. Here F_0 denotes the amplitude of the applied driving. In order to achieve maximal responses, the frequency ν was chosen to coincide with the characteristic frequency ν_0 of the hair bundle under study.

When measuring the sensitivity $|\chi|(F_0, \nu)$ as a function of driving amplitude, the different regimes typical of hair bundle responsiveness could be distinguished (see fig. 5.7A): the sensitive linear response regime for weak driving ($F_0 \lesssim 1$ pN), the regime of nonlinear compression for intermediate driving amplitudes, and the less sensitive linear response regime for strong driving ($F_0 \gtrsim 50$ pN). In order not to damage the hair bundle during the experiment, no forcing amplitudes larger than $F_0 = 50$ pN were used. When the hair bundle was coupled to two cyber clones of similar characteristics, an increase of the sensitivity for weak driving amplitudes ($F_0 < 1$ pN) was observed (see fig. 5.7A). By measuring the sensitivity of the hair bundle for a weak stimulus ($F_0 = 0.3$ pN) alternatingly in the coupled ($K = 0.2$ pN/nm) and not-coupled situation ($K = 0$ pN/nm), we could show that the observed effect was reversible (see fig. 5.7B). When determining the hair bundle's response for a weak stimulus ($F_0 = 0.3$ pN) for increasing coupling stiffnesses, we found that

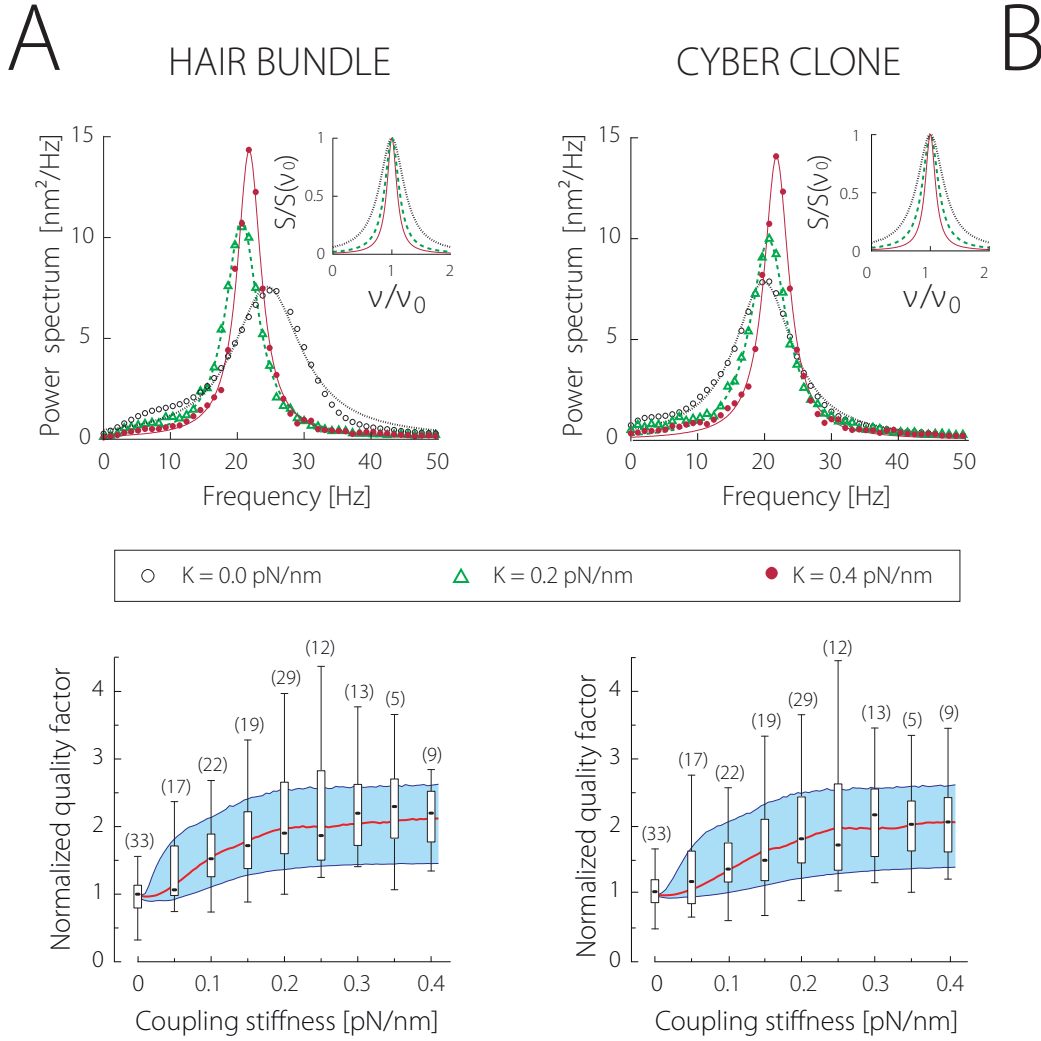


Figure 5.6: Increased coherence of spontaneous oscillations. (Top) Power spectral densities $S(\nu)$ of a hair bundle (shown in A) and of the two cyber clones it was coupled to (shown in B) for various coupling strengths. Solid lines correspond to fits with a Lorentzian function. In the respective inset, these fits are shown as a function of normalized frequency ν/ν_0 as well as normalized by their respective peak value. Note the sharpening of the peak with increasing coupling strength K . The data shown was obtained with the same cell as shown in fig. 5.5. (Bottom) The quality factor Q of hair-bundle oscillations (shown in A) and cyber-clone oscillations (shown in B) as a function of coupling stiffness K . A summary of the experimental data recorded for 33 different cells is shown. Quality factors for each cell were normalized by the mean value obtained from different measurements (typically three) in the absence of coupling. Boxes include 25% of the data points above and below the median (thick dash); whiskers delimit the total range of measured values (numbers of cells that were recorded are indicated above top whiskers). Also shown are the median (red line) and the total range of values (blue area) obtained for the quality of the central hair bundle in pure simulations of three coupled cyber clones using the 33 sets of parameters implemented in experiments. Correlation between median values obtained from experiments and simulations was quantified by a Pearson test ($R=0.97$, $P < 10^{-5}$).

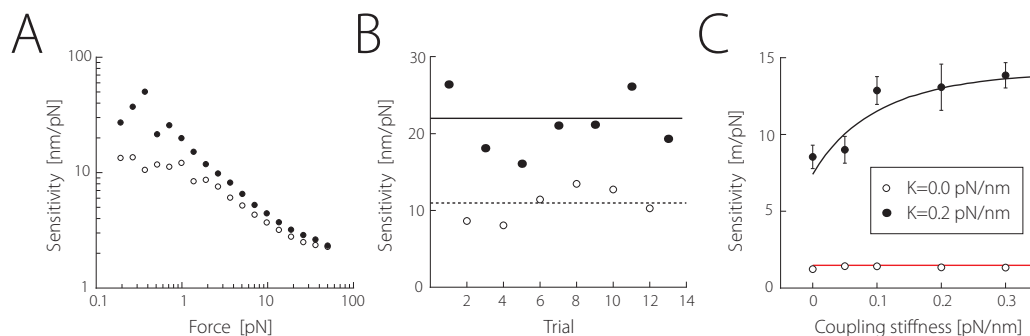


Figure 5.7: Effects of coupling on nonlinear amplification. (A) Hair-bundle sensitivity as a function of the external force F_{ext} without coupling (white disks) and with a coupling stiffness $K = 0.2$ pN/nm (black disks). (B) Hair-bundle sensitivities at $F_{\text{ext}} = 0.3$ pN with $K = 0.2$ pN/nm (black disks) and without coupling (white disks) were significantly different (Student t-test $P < 5.0 \cdot 10^{-4}$). Pure computer simulations yielded sensitivities shown by thin continuous (coupled) and dashed (uncoupled) lines that were not statistically different from mean experimental values (Student t-tests $P = 0.78$ and $P = 0.59$ for coupled and uncoupled conditions, respectively). (C) Hair-bundle sensitivity at $F_{\text{ext}} = 0.5$ pN (black disks) and $F_{\text{ext}} = 50$ pN (white disks) as a function of coupling stiffness. Simulations yielded similar sensitivities shown by thin lines (Pearson correlation coefficient for $F_{\text{ext}} = 0.5$ pN: $R = 0.91$, $P = 0.03$).

its sensitivity saturated for the strongest couplings we could achieve (see fig. 5.7C). For large driving forces ($F_0 = 50$ pN), the sensitivity under coupling was almost unchanged as compared to the uncoupled case (see fig. 5.7C). We compared our findings with results from pure computer simulations of three coupled cyber clones, using the same parameter sets as implemented in experiments. Good agreement was found (see fig. 5.7B and C).

Coupling induced an increase of sensitivity for weak driving amplitudes, but did not have an effect on the sensitivity for strong driving. The gain of the hair bundle (see eq. (2.8)) accordingly increased as an effect of coupling to the two cyber clones. More specifically, it grew from a value of 6.0 ± 0.6 (mean \pm SE; $n=14$ cells) in the absence of coupling to 11.3 ± 0.9 for strong coupling (see fig. 5.8A). When quantifying the response of the two cyber clones as measured during the experiments, a similar gain increase was found (see fig. 5.8B). As in the case of the increased coherence of spontaneous oscillations, the bidirectional coupling we implemented thus brought about an enhancement of the performance for both the hair bundle and the two cyber clones.

5.5 Effects of gentamicin

Gentamicin, an aminoglycoside antibiotic that blocks transduction channels of hair bundles [111], afforded a means to switch off the amplifier of the hair bundle and thus to further assay the interplay between the hair bundle and its two cyber clones. When an oscillatory hair bundle was strongly coupled to its cyber clones, gentamicin

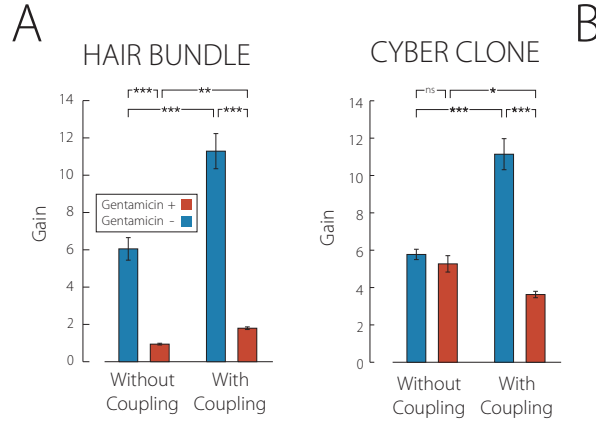


Figure 5.8: Gain of the hair-bundle amplifier under various conditions. (A) Average gains are shown for the hair bundle as measured in experiments under normal conditions (blue) and in the presence of the channel blocker gentamicin (red). We compare the results in the absence of coupling (left) and under strong coupling with $K = 0.15 - 0.4$ pN/nm (right). The statistical significance of observed differences under these diverse conditions was evaluated by a Student t-test and is indicated (**: $p < 0.01$; ***: $p < 0.001$, ns: not significant). (B) Corresponding results are shown for those cyber clones that were coupled to the hair bundles during data acquisition for the plots in (A).

application to the hair bundle (keeping the cyber clones unchanged) resulted in a gain reduction of the hair bundle from 11.3 ± 0.9 to 1.8 ± 0.1 ($n=3$ cells, see fig. 5.8A). This value was only slightly larger than the gain of unity for which the hair bundle provides no amplification. Weak amplification resulted here from the active driving of the passive hair bundle by the oscillatory cyber clones. In addition, the amplificatory gain of the cyber clones decreased from 11.1 ± 0.8 to 3.6 ± 0.2 , thus to a lower value than the gain of 5.3 ± 0.4 that was measured for the uncoupled system (see fig. 5.8B).

5.6 Parameter mismatches

As was shown in fig. 5.4, the cyber clones used in experiments had similar statistics as compared to the respective hair bundle they were coupled to. The attained match, however, between hair bundle and cyber clones due to the limited time available for parameter adjustment was not perfect. This poses the question as to the expected effects of parameter inhomogeneities. To address this problem, we performed pure computer simulations of three coupled cyber clones for a number of coupling stiffnesses and parameter mismatches between the central and the two identical flanking oscillators. The parameter set defining the central cyber clone was unchanged in all simulations¹. In the absence of coupling, its spontaneous

¹Parameters of the central cyber clone: $\lambda = 2.8 \mu\text{N}\cdot\text{s}\cdot\text{m}^{-1}$, $\lambda_a = 10.0 \mu\text{N}\cdot\text{s}\cdot\text{m}^{-1}$, $K_{GS} = 0.75 \cdot \text{m}^{-1}$, $K_{SP} = 0.6 \text{mN}\cdot\text{m}^{-1}$, $D = 62.14 \text{nm}$, $N = 50$, $T = 300 \text{K}$, $T_a = 1.5T$, $\Delta G = 10k_B T$, $F_{\max} =$

oscillations had a characteristic frequency of $f_0 \approx 7.5$ Hz, a root-mean-squared amplitude of $A_{\text{RMS}} \approx 16$ nm and a quality of $Q \approx 2.15$ (see fig. 5.9B).

Scaling both friction coefficients of an oscillatory cyber clone by a constant factor $c > 0$, while not affecting their amplitude and quality, leads to a shift of the characteristic frequency of spontaneous oscillations. To see this, note that the corresponding equations capturing cyber-clone dynamics, i.e.

$$\begin{aligned} c\lambda \frac{dX(t)}{dt} &= -K_{\text{GS}}(X - X_a - DP_o) - K_{\text{SP}}X + \sqrt{c}\xi(t) \\ c\lambda_a \frac{dX_a(t)}{dt} &= K_{\text{GS}}(X - X_a - DP_o) - F_{\text{max}}(1 - SP_o) + \sqrt{c}\xi_a(t), \end{aligned}$$

by means of introducing the rescaled variable $\bar{t} = t/c$ can be transformed into

$$\begin{aligned} \lambda \frac{dX(\bar{t})}{d\bar{t}} &= -K_{\text{GS}}(X - X_a - DP_o) - K_{\text{SP}}X + \xi(\bar{t}) \\ \lambda_a \frac{dX_a(\bar{t})}{d\bar{t}} &= K_{\text{GS}}(X - X_a - DP_o) - F_{\text{max}}(1 - SP_o) + \xi_a(\bar{t}). \end{aligned}$$

In particular, the rescaling of the noise term appearing in the dynamic equation for the deflection X follows from

$$\langle \sqrt{c}\xi(t)\sqrt{c}\xi^*(t') \rangle = c\delta(t - t') = \delta\left(\frac{t - t'}{c}\right) = \delta(\bar{t} - \bar{t}') = \langle \xi^*(\bar{t})\xi(\bar{t}') \rangle.$$

A similar calculation holds true for the noise term affecting the dynamics of the motor variable X_a . In other words, rescaling the two friction coefficients is equivalent to an appropriate rescaling of time. As a consequence, the quality and magnitude of spontaneous oscillations are indeed unchanged. For the frequency shift $\Delta f = f_c - f_0$ between the cyber clone with rescaled friction coefficients and frequency f_c and the original cyber clone with frequency f_0 , we find

$$\Delta f = f_0 \left(\frac{1}{c} - 1 \right).$$

In our simulations, we introduced a prescribed intrinsic frequency mismatch Δf between the central cyber clone and the two neighboring ones by adjusting the friction coefficients of the two cyber clones accordingly (see fig. 5.9A and D). For the two flanking two cyber clones identical parameters were chosen. Varying the coupling stiffness K , we then studied the behavior of the system under elastic coupling (see fig. 5.9A-C).

We found that for all Δf in the range [-5,25] Hz the three cyber clones under strong coupling ($K \gtrsim 0.3$ pN/nm) synchronized and oscillated at a single characteristic frequency (see fig. 5.9A). In order to reach this synchronized state, with

increasing frequency mismatch larger coupling stiffnesses were required. The root-mean-squared amplitude of oscillations in the case of vanishing frequency mismatch, i.e. $\Delta f = 0$ Hz, under coupling remained almost constant (see fig. 5.9B). In contrast, for frequency mismatches $\Delta f \gtrsim 5$ Hz and intermediate coupling strengths, i.e. $K \approx 0.2$ pN/nm, an appreciable reduction was found when the minimal oscillation amplitude of all three cyber clones was measured. Oscillations, however, never entirely ceased, i.e. no so-called amplitude death occurred [41, 124]. Most importantly, in all cases an increase in the quality of spontaneous oscillations was observed under strong coupling for all three cyber clones (see fig. 5.9C). For three identical cyber clones, i.e. $\Delta f = 0$, an appreciable enhancement was found already for weak coupling stiffnesses. For large Δf and intermediate K , coupling, however, resulted in a poorer quality of spontaneous oscillations.

On the basis of these results, we do not expect small parameter mismatches to have affected the outcome of our measurements in a profound way. In particular, inhomogeneities as considered above are anticipated to counteract the beneficial effects of elastic coupling. Hence, our experimental results might have been obtained under less than ideal conditions. This suggests that coupling-mediated noise reduction, indeed, constitutes a robust mechanism for the enhancement of hair-bundle performance.

5.7 Summary

In this chapter, we have presented the results of a hybrid experiment. By means of a dynamic force clamp, we were able to couple a hair bundle to two so called cyber clones, i.e. two virtual hair bundles that only existed as stochastic simulations on a computer. In this way, a situation was emulated in which the hair bundle was elastically coupled to two flanking neighbors of similar characteristics. The results presented in chapter 4 gave rise to the expectation, such an elastic coupling could lead to an increased regularity of spontaneous oscillations as well as an enhancement of the gain of the hair-bundle amplifier. Note, however, the outcome of our experiment *a priori* was not to be foreseen. The physical description of hair-bundle dynamics presented in chapter 1.4.3 was shown to capture many important features characteristic of a noisy hair bundle's behavior. Its predictive power for a complex situation such as posed by a system of elastically coupled hair bundles, however, remained to be established. In our experiments, we indeed found that the synergic interaction between the hair bundle and its two cyber clones effected an enhancement in the expected way for all three oscillators. On the one hand, this offers evidence for the applicability of the results obtained in the computational study presented in chapter 4. More importantly, our findings attest the hair bundle's ability to integrate in a mutually beneficial way in a multicomponent system of coupled noisy oscillators. A hair bundle that is elastically coupled to hair bundles of similar characteristics is thus strongly expected to outperform an isolated one.

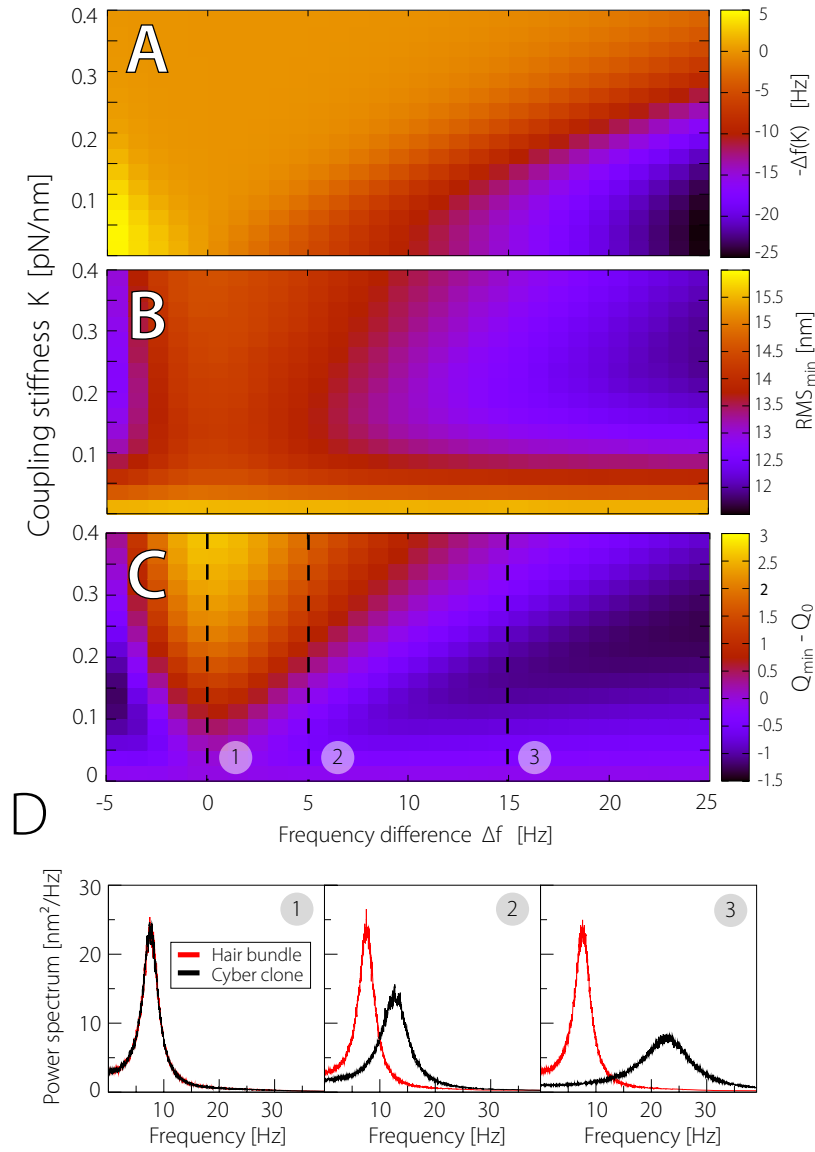


Figure 5.9: The effect of coupling in simulated systems of three coupled non-identical cyber clones. In (A-C), we show color plots as functions of coupling stiffness K and frequency mismatch Δf . In (A), the negative frequency mismatch $-\Delta f(K)$ between the left and central cyber clone is shown. Note that for large coupling strengths only one frequency in each system survives. In (B), we plot the minimum of all root-mean-squared amplitudes RMS_{\min} of spontaneous oscillations performed by the three cyber clones. For large Δf and intermediate K , this quantity is appreciably reduced. In (C), the difference between the minimum of all quality factors Q_{\min} as measured in each system and the respective value in the absence of coupling, denoted Q_0 , is shown. Values larger than zero indicate an enhanced phase coherence for all cyber clones in a system. Note that the most pronounced enhancement is observed in the case of vanishing frequency mismatch Δf . In (D), power spectra of the spontaneous activity in the absence of coupling are shown for choices of parameters corresponding to the dashed lines in (C). The frequency shift due to the scaled friction coefficients of cyber clones is clearly visible.

Chapter 6

Conclusions and outlook

Human hearing relies on an active process. The cochlear amplifier produces mechanical work to boost basilar membrane vibrations in order to achieve its high sensitivity, sharp frequency selectivity, and wide dynamic range. Spontaneous otoacoustic emissions constitute a demonstrative manifestation of this physiologically vulnerable mechanism. Current theoretical descriptions of active cochlear mechanics are based on the physics of nonlinear oscillators. When operating close to a supercritical Hopf bifurcation, any dynamical system exhibits generic features of nonlinear amplification reminiscent of cochlear functioning. Sensory hair bundles can power mechanical movements of their tip, oscillate spontaneously, and operate as tuned nonlinear amplifiers of weak periodic stimuli. Active hair-bundle motility therefore constitutes a promising candidate with respect to the biophysical implementation of the active process underlying human hearing.

Individual hair bundles, however, quantitatively do not match the extraordinary performance of the cochlear amplifier. While for instance the response of the basilar membrane to auditory stimulation can exhibit gains of up to 1000, the gain of an isolated hair bundle is on the order of only about 5-10. The hair bundle is subject to intrinsic fluctuations originating from diverse sources, such as thermal interactions with the surrounding fluid, the stochastic opening and closing of mechanosensitive ion channels, and fluctuating forces generated by adaptation motors. In this thesis, we have investigated the noise-imposed limitations of nonlinear amplification by active sensory hair bundles from a theoretical and experimental point of view.

Conclusions. In chapter 2, we have presented theoretical results obtained within the framework of a stochastic description of active hair-bundle motility. In particular, we have studied the effects of noise reduction on the spontaneous and driven dynamics of an isolated hair bundle [99]. The phase coherence of spontaneous oscillations as measured in terms of the quality Q was found to increase linearly with inverse noise strength. While the response to periodic stimulation for large stimulus forces is almost independent of noise strength, for weak driving amplitudes sensitivity is ultimately limited by fluctuations. More specifically, the amplification gain

G was found to increase almost linearly with inverse noise strength. At the same time, reducing intrinsic fluctuations effects an extension of the range of forces for which nonlinear compression is observed. We have quantified the degree of nonlinear compression by means of the local exponent of nonlinear compression α . For both operation points under study, upon a suitable reduction of intrinsic fluctuations the local exponent α as a function of driving amplitude exhibits a minimum close to -1. This value corresponds to an even more compressive response than expected for a critical oscillator operating at a supercritical Hopf bifurcation ($\alpha \equiv -2/3$). Furthermore, in line with the narrower spectral bandwidth corresponding to the enhanced regularity of spontaneous oscillations, the response of the hair bundle upon noise reduction was found to be more and more sharply tuned. These results attest to the noise-imposed limits of hair-bundle performance. We conclude that a reduction of intrinsic fluctuations is expected to enhance the performance of the hair bundle as a tuned nonlinear amplifier.

In chapter 3, we have discussed the spontaneous and driven dynamics of two generic oscillatory systems, the noisy phase oscillator and the noisy Hopf oscillator [79, 99]. In particular, the dynamics of the Hopf oscillator were considered on the oscillatory side of the bifurcation. The quality of spontaneous oscillations in the case of the phase oscillator was shown to be proportional to the inverse noise strength. In the limit of weak noise intensities, the same holds true for the Hopf oscillator. The response of the two oscillators to a periodic driving can be understood as being shaped by phase-locking, and in the case of the Hopf oscillator in addition by a growth of the oscillation amplitude. The degree of entrainment in the limit of weak driving amplitudes depends critically on the driving frequency and the noise intensity. Sensitivity for tuned stimuli in linear response for both oscillators was shown to be proportional to the inverse noise strength. In the limit of strong driving, phase-locking is essentially complete for any given noise strength and driving frequency. In the case of the phase oscillator, once full entrainment is reached, a further increase of the driving amplitude cannot be reflected in the response of the system. In terms of the sensitivity this corresponds to a decay with a local exponent $\alpha = -1$. An external driving of sufficient strength in the case of the Hopf oscillator also effects a growth of the oscillation amplitude. For the noisy Hopf oscillator, we have derived an analytical expression for the full nonlinear response function and the local exponent of nonlinear compression α . In the limit of strong driving, the sensitivity of the Hopf oscillator decays in a nonlinear fashion with a local exponent $\alpha = -2/3$ in the supercritical and $\alpha = -4/5$ in the subcritical case. In this limit, the response of the oscillator is largely independent of the noise strength. For intermediate driving amplitudes, strong nonlinear compression with a local exponent $\alpha \gtrsim -1$ may also be present for the noisy Hopf oscillator. While phase-locking is almost complete, the oscillation amplitude in this regime is unchanged by the stimulus. Such a regime can exist if noise is suitably small, and in the case of the supercritical Hopf oscillator, if the system operates far enough from the bifurcation. In summary, we conclude that the noisy Hopf oscillator, next to being of interest

in its own right, can be viewed as offering the right abstract framework in order to discuss and analyze generic aspects of active hair-bundle dynamics.

Hair bundles *in vivo* are often coupled via overlying membranes. In chapter 4, we have presented the results of a theoretical study that was aimed at investigating the effects of elastic coupling on the spontaneous dynamics and amplification properties of groups of interconnected hair bundles [34]. For one, we have presented simulation data for homogeneous systems of $N \times N$ hair bundles that were coupled by means of linear springs of stiffness K . We have found that coupling of suitable strength synchronizes spontaneous hair-bundle oscillations throughout the system. For coupling strengths exceeding the passive hair-bundle stiffness, $K > K_{\text{SP}}$, coupling was found to induce an effective noise reduction. By means of a meanfield argument, we could show that strong coupling is expected to reduce the strength of intrinsic fluctuations by a factor $1/N^2$, i.e. in proportion to the number of hair bundles within the system. Consistent with results presented in chapter 2 for isolated hair bundles with artificially reduced noise strength, elastic coupling was shown to effect an increased quality of spontaneous oscillations, a sharper frequency selectivity, and an enhanced amplification gain for all hair bundles in a given system. In the limit of strong coupling, both the quality and the amplification gain were found to increase linearly with the number of coupled hair bundles. Coupling already a modest number of hair bundles ($N^2 = 81$) could increase the gain of the central hair bundle to about 400, i.e. to a value comparable to gains observed for the mammalian cochlea. Furthermore, we have investigated the effect of coupling on systems of 3×27 hair bundles with a built-in frequency gradient, mimicking the setup as observed in the mammalian cochlea. Most importantly, we found that for intermediate coupling strengths comparable to the average pivotal stiffness, $K \approx \bar{K}_{\text{SP}}$, the amplification gain of hair bundles within the system was significantly enhanced, while some frequency variability in the system was preserved. Our results suggest that in the cochlea a local adjustment of tectorial membrane elasticity to the pivotal stiffness of hair bundles could optimize the tradeoff between frequency variability and coupling-induced noise reduction. According to the available measurements of material properties of the tectorial membrane in various species, such local stiffness matching is, indeed, realized. We conclude that elastic coupling as frequently observed *in vivo* might for some inner ear organs constitute a morphological specialization, enhancing hair-bundle mediated active amplification by means of a noise reduction effect.

In chapter 5, we have presented the results of an experimental study [9]. To probe the effect of elastic coupling on the dynamics of oscillatory hair bundles from the sacculus of the bullfrog, we combined micromanipulation experiments with real-time stochastic computer simulations of hair-bundle dynamics. By means of a dynamic force clamp procedure we could effectively couple a biological hair bundle to two virtual neighbors, also referred to as cyber clones. By finely tuning simulation parameters, we were able to produce cyber clone oscillations that in the absence of coupling had similar characteristics as compared to the respective hair bundle

under study. As predicted by our theoretical results discussed in chapter 4, coupling lead to a synchronization of the spontaneous oscillations of the three oscillators and furthermore rendered these oscillations more regular. Probing the response of the hair bundle to periodic driving, we found that the amplification gain of the hair bundle increased from about 6.0 ± 0.6 (mean \pm SE; n=14 cells) in the absence of coupling, to about 11.3 ± 0.9 under strong coupling. All observed effects were in quantitative agreement with pure computer simulations of three coupled cyber clones. Upon interfering with the active process of the hair bundle by means of gentamicin, the observed increased amplification gain was lost. On the one hand, our results validate the biophysical description of hair-bundle dynamics that was used throughout this thesis. On the other hand, our data strongly support the conclusion that hair bundles, indeed, are capable to benefit from coupling-induced noise reduction. Our experimental results therefore reinforce the conclusions drawn on the basis of the results discussed in chapter 4.

Active hair-bundle motility exhibits all the hallmarks characteristic of the cochlear amplifier. Single hair-bundle performance, however, is seriously impeded by intrinsic fluctuations. Elastic coupling of already a small group of hair bundles can significantly reduce the detrimental effect of noise. In summary, our results suggest that the cochlear amplifier relies on hair-bundle cooperation to overcome intrinsic noise limitations and achieve high sensitivity and sharp frequency selectivity.

Outlook. Two noise sources have been proposed to directly influence the deflection of the hair bundle and thus shape its spectral characteristics and amplification properties. On the one hand, there is thermal excitation by the surrounding fluid. On the other hand, there is channel clatter, i.e. the stochastic opening and closing of mechanosensitive ion channels. Because of the gating swing, channel clatter leads to a fluctuating force that acts on the hair bundle. In order to better understand the noise-imposed limits of hair-bundle performance, a more detailed analysis of the relative importance of these two sources of fluctuations is desirable. In ref. [118] it has been argued on theoretical grounds that channel clatter dominates hair-bundle dynamics. As of today, no experimental verification of this claim exists. The dynamics of ion channels within the hair bundle are characterized by time constants on the order of one millisecond [133]. Hence, channel clatter effectively acts as colored noise. Fluctuations due to hydrodynamic friction, in contrast, occur on much faster time scales and therefore can be assumed as white. First results indicate that by means of an analysis of the temporal fine structure of hair bundle trajectories, the relative importance of noise acting on different time scales can be extracted from experimental data. Furthermore, extending the hair-bundle description presented in ref. [118] by including the dynamics of individual ion channels could foster a deeper insight as to the relative importance of the two noise sources.

In this thesis, we have investigated the biophysical principles underlying cochlear amplification on a multicellular scale (see fig. 6.1). Focusing on active hair-bundle motility, our results suggest that cochlear amplification relies on small groups of

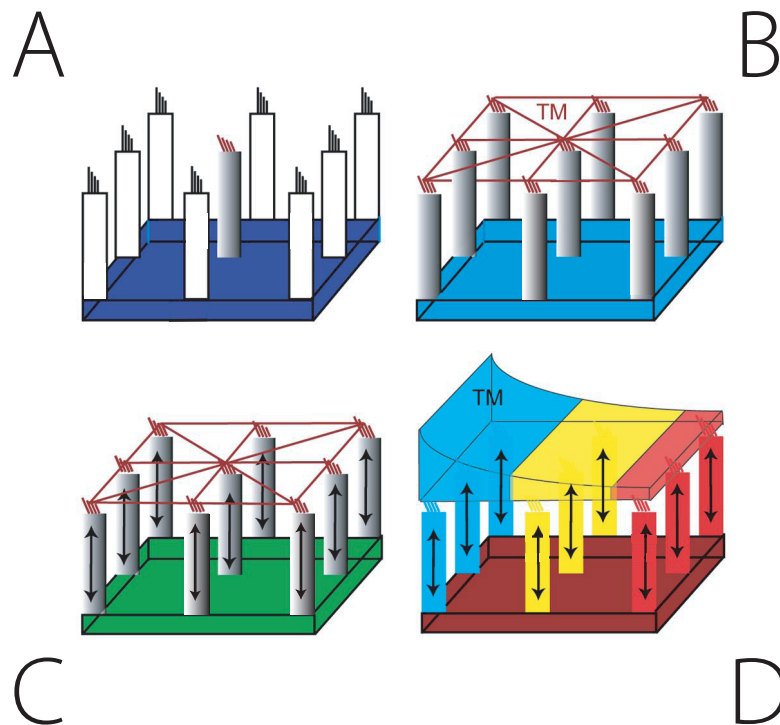


Figure 6.1: Towards an understanding of active cochlear mechanics on a multicellular scale. (A) A vast body of literature exists, dealing with the properties of isolated hair cells. (B) This thesis aims at adding new insights at the level intermediate to the single cell and the whole organ. In particular, we have investigated the dynamics of small groups of coupled hair bundles. For simplicity, coupling by the tectorial membrane (TM) has been described by means of linear springs. (C) A more realistic model of cochlear operation will need to incorporate the electromotile response of cochlear outer hair cells. (D) Furthermore, for instance the effect of gradients and anisotropies in tectorial membrane stiffness needs to be elucidated. Adapted from ref. [127].

elastically coupled hair bundles to provide sharp frequency selectivity and a compressive nonlinearity extending over a wide dynamic range. However, there are two limitations. Firstly, the high amplification gain observed in the cochlea is not easily reached in our model if at the same time a frequency gradient is maintained. Secondly, hair bundle movements may be inefficient to significantly drive basilar membrane vibrations. These issues could be resolved by regarding the cochlear amplifier as a combination of outer hair cell electromotility and active motility of locally coupled hair bundles. In this scenario, the frequency selectivity and the compressive nonlinear properties of the cochlear amplifier are provided by coupled hair bundles. Outer hair cell electromotility is a largely linear element [5]. It may allow hair bundle movements to efficiently drive basilar membrane vibrations. To elucidate the role of electromotility in cochlear amplification and its interplay with active hair bundle motility poses an important task for future work [107]. Further-

more, in this thesis we have opted for a description of elastic coupling by means of linear springs. Tectorial and otolithic membranes *in vivo* can exhibit morphological gradients as well as anisotropies [147, 58, 135, 50]. In order to further gauge the importance of elastic coupling for the cochlea and other inner ear organs, a more detailed description of hair-bundle coupling as realized *in vivo* is asked for.

Next to a mechanical oscillator in form of their sensory hair bundle, hair cells are known to possess an electrical oscillator, residing within their basolateral membrane [74, 149, 143]. This oscillator can perform spontaneous and evoked voltage oscillations. It has been suggested that the frequency-tuning of frog saccular hair cells is partly determined by characteristics of this electrical system [42]. Because of the mechanosensitive ion channels in the tips of stereocilia, hair-bundle oscillations modulate the ionic currents entering the soma and thus influence the electric circuitry of the underlying hair cell. Recent experimental results suggest that a coupling also exists in the opposite direction [130]. It has been hypothesized that by modulating the electro-diffusion of calcium ions, oscillations of the membrane potential could influence hair-bundle dynamics [12, 70, 130]. Recently, it has been shown on theoretical grounds that a bidirectional coupling of the mechanical and electrical oscillator of the hair cell could bring about an enhancement of the quality of spontaneous hair-bundle oscillations and of the amplification properties of the hair-bundle amplifier [61]. This result indicates that sensory organs in the inner ear in addition to elastic coupling of hair bundles might also employ alternative routes for reducing the detrimental effect of intrinsic fluctuations and enhancing their performance. To gain a better understanding with respect to the relative importance of these different strategies poses an interesting challenge for further research.

Appendix A

Discretization of cyber-clone dynamics

During the hybrid experiment described in chapter 5.1, the dynamic equations of cyber clones in each iteration of the dynamic force clamp were integrated with a finite time step Δt between 10^{-1} ms and $4 \cdot 10^{-1}$ ms, i.e. X_1 and X_2 were updated at discrete times $n\Delta t$. The same holds true for the base of the stimulus fiber that was used to apply forces to the tip of the hair bundle under study. Due to technical limitations, the stepsize Δt could not be decreased further. Movements of the hair bundle, in contrast, were continuous in time. In this appendix, we present results that suggest that the discrete nature of the feedback procedure with stepsize Δt was not influencing the outcome of the experiment. To this end, we resorted to pure computer simulations of three coupled cyber clones. More specifically, the dynamics of the hair bundle as measured in experiments was substituted by a cyber clone whose dynamics obeyed

$$\dot{X} = \dot{X}_{\text{DET}} + F_K(t) + F_{\text{ext}}(t) + \xi(t) \quad (\text{A.1})$$

$$\dot{X}_a = \dot{X}_{a,\text{DET}} + \xi_a(t), \quad (\text{A.2})$$

where \dot{X}_{DET} and $\dot{X}_{a,\text{DET}}$, with the obvious modifications, are given by eq. (5.3) and eq. (5.4), respectively. As the dynamic equations for X , X_1 and X_2 for $K = 0$ pN/nm were identical, we set $X_{\text{off}} = 0$. To reflect the discrepancy between the continuous nature of hair bundle dynamics on the one hand and the discrete nature of the cyber clones' update rules on the other hand, eq. (A.1) and eq. (A.2) were integrated with a time step $\Delta t_{\text{HB}} = 10^{-3}$ ms. While still rendering the evolution of X discrete, as necessarily is the case when performing simulations on a computer, Δt_{HB} was two orders of magnitude smaller than the smallest Δt used during experiments. We have only considered the case $F_{\text{ext}} = 0$ pN.

For each set of parameters used for defining cyber clones during an actual experiment, three different simulations with identical initial conditions were performed, corresponding to stepsizes $\Delta t = 10^{-3}$ ms, 10^{-1} ms, and $4 \cdot 10^{-1}$ ms that were used to update the two flanking cyber clones with position X_1 and X_2 (see fig. A.1 A). In order to be able to discern the effect of these different time steps, in contrast to possibly different realizations of the noise terms, during the three different runs

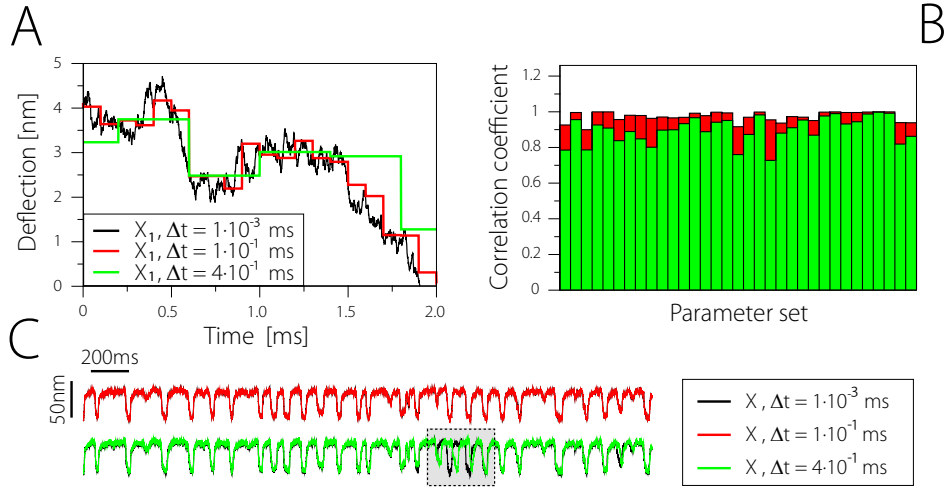


Figure A.1: Changing the discretization of cyber-clone dynamics. The simulation procedure is explained in the main text. (A) For one parameter set and three different time steps $\Delta t = 10^{-3}$ ms (black), 10^{-1} ms (red), and $4 \cdot 10^{-1}$ ms (green), a section of the trajectory of the left cyber clone, i.e. $X_1(t)$ is shown. For the two larger time steps the piecewise constant nature of the dynamics is clearly visible. Note that due to the use of frozen noise, the time evolution of the three trajectories is very similar on timescales on the order of the largest time step. (B) For all parameter sets used in experiments, simulations as in (A) were performed. We plot cross-correlation coefficients between the hair-bundle trajectory as generated with $\Delta t = 10^{-3}$ ms and a coarser integration with $\Delta t = 10^{-1}$ ms (red) and $\Delta t = 4 \cdot 10^{-1}$ ms (green). (C) For the same parameter set as in (A) we show twice (top and bottom) the trajectory of the central cyber clone $X(t)$ generated with $\Delta t = 10^{-3}$ ms (black). Also plotted is the corresponding trajectory for $\Delta t = 10^{-1}$ ms (top, red) and $\Delta t = 4 \cdot 10^{-1}$ ms (bottom, green). Note that the upper two trajectories are almost identical. The shaded area indicates a period in which differences for the largest time step appear.

so-called frozen noise was used. Six sequences of suitable length x_m , $x_{a,m}$, $x_{i,m}$, and $x_{a,i,m}$ ($i = 1, 2$) of normally distributed random numbers with zero mean and unit variance were chosen. These sequences were the same in all three simulations. Denoting $N = \Delta t / \Delta t_{\text{HB}}$, the cyber clones X_1 and X_2 for a given Δt were updated according to

$$X_i((n+1)\Delta t) = X_i(n\Delta t) + (\dot{X}_{i,\text{DET}}(n\Delta t) - F_i(n\Delta t))\Delta t + \sqrt{2k_B T \lambda \Delta t_{\text{HB}}} \sum_{m=nN}^{(n+1)N-1} x_{i,m}$$

and

$$X_{a,i}((n+1)\Delta t) = X_{a,i}(n\Delta t) + \dot{X}_{a,i,\text{DET}}(n\Delta t)\Delta t + \sqrt{2k_B T \lambda_a \Delta t_{\text{HB}}} \sum_{m=nN}^{(n+1)N-1} x_{a,i,m}.$$

Note that because of

$$\text{Var} \left(\sqrt{2k_B T \lambda \Delta t_{\text{HB}}} \sum_{m=nN}^{(n+1)N-1} x_{i,m} \right) = \text{Var}(x_{i,m} \sqrt{2k_B T \lambda \Delta t})$$

this is consistent with the update rule used in experiments. The same holds true for the update rule of $X_{a,i}$. At times intermediate between $n\Delta t$ and $(n+1)\Delta t$, i.e. $n\Delta t + k\Delta t_{\text{HB}}$ with $0 < k < N$, we set

$$X_i(n\Delta t + k\Delta t_{\text{HB}}) = X_i(n\Delta t) \quad \text{and} \quad X_{i,a}(n\Delta t + k\Delta t_{\text{HB}}) = X_{i,a}(n\Delta t).$$

The resulting trajectories $X_1(t)$ and $X_2(t)$ thus were piecewise constant functions (see fig. A.1 A). The use of frozen noise ensured that random increments due to noise terms, while for smaller time steps Δt being resolved on finer timescales, on larger timescales were identical. This was achieved by the summing procedure in the above equations. The integration steps for the central cyber clone read

$$\begin{aligned} X(n\Delta t + (k+1)\Delta t_{\text{HB}}) &= X(n\Delta t + k\Delta t_{\text{HB}}) \\ &\quad + (\dot{X}_{\text{DET}} - F_K)(n\Delta t + k\Delta t_{\text{HB}})\Delta t_{\text{HB}} \\ &\quad + x_{nN+k} \sqrt{2k_B T \lambda \Delta t_{\text{HB}}}, \\ X_a(n\Delta t + (k+1)\Delta t_{\text{HB}}) &= X_a(n\Delta t + k\Delta t_{\text{HB}}) \\ &\quad + \dot{X}_{a,\text{DET}}(n\Delta t + k\Delta t_{\text{HB}})\Delta t_{\text{HB}} \\ &\quad + x_{a,nN+k} \sqrt{2k_B T_a \lambda_a \Delta t_{\text{HB}}}. \end{aligned}$$

While the cyber clones X_1 and X_2 during each time interval $[n\Delta t, (n+1)\Delta t[$ were kept at a fixed position, the central cyber clone X was not. Accordingly, the coupling force felt by the hair bundle during this period was also changing. This is expected to be the case during experiments as well. In each iteration of the feedback, after the glass fiber's base was moved, it stayed fixed until it was moved again in the next time step. The hair bundle, however, slightly changed its position with respect to the fiber's base, leading to a change of the exerted force over the period of one time step. Note that here we neglect the finite rise time of the piezo, as well as the effect of viscous drag on the stimulus fiber.

Updating the flanking cyber clones with time steps of either $\Delta t = 10^{-3}$ ms or $\Delta t = 10^{-1}$ ms leads to no appreciable differences (see fig. A.1C). Cross-correlation coefficients between the respective trajectories of the central cyber clone for all parameter sets were close to one (see fig. A.1B). When comparing the results for $\Delta t = 10^{-3}$ ms and $\Delta t = 4 \cdot 10^1$ ms, the two trajectories of the central cyber clone typically for long stretches were almost identical (see fig. A.1C). Occasionally, the two trajectories for two or three oscillation cycles fell out of synchrony (see fig. A.1C, shaded area). This leads to slightly lower cross-correlation coefficients between the two trajectories. The overall shape and statistics of the oscillation however was unchanged. These results strongly suggest that iterating the feedback procedure at a rate of 2.5-10 kHz in the experiments was sufficient not to introduce significant artifacts related to the discretization of the update rules.

Bibliography

- [1] http://php.med.unsw.edu.au/embryology/index.php?title=File:Adult_hearing_embryonic_origins.jpg.
- [2] C. C. Abnet and D. M. Freeman. Deformations of the isolated mouse tectorial membrane produced by oscillatory forces. *Hear. Res.*, 144:29–46, 2000.
- [3] M. Abramowitz and I. A. Stegun. *Handbook of Mathematical Functions*. Dover Publications, New York, 1965.
- [4] J. A. Acebrón, L. L. Bonilla, C. J. P. Vicente, F. Ritort, and R. Spigler. The Kuramoto model: A simple paradigm for synchronization phenomena. *Rev. Mod. Phys.*, 77:137–185, 2005.
- [5] J. Ashmore. Cochlear outer hair cell motility. *Physiol. Rev.*, 88:173–210, 2008.
- [6] J. Ashmore, P. Avan, W.E. Brownell, P. Dallos, K. Dierkes, R. Fettiplace, K. Grosh, C. Hackney, A.J. Hudspeth, F. Jülicher, B. Lindner, P. Martin, J. Meaud, C. Petit, J.R. Santos-Sacchi, and B. Canlon. The remarkable cochlear amplifier. *Hear. Res.*, In Press, 2010.
- [7] J. A. Assad, N. Hacohen, and D. P. Corey. Voltage dependence of adaptation and active bundle movement in bullfrog saccular hair cells. *Proc. Natl. Acad. Sci. USA*, 86:2918–2922, 1989.
- [8] J. A. Assad, G. M. G. Shepherd, and D. P. Corey. Tip-link integrity and mechanical transduction in vertebrate hair cells. *Neuron*, 7:985–994, 1991.
- [9] J. Barral, K. Dierkes, B. Lindner, F. Jülicher, and P. Martin. Coupling a sensory hair-cell bundle to cyber clones enhances nonlinear amplification. *Proc. Natl. Acad. Sci. USA*, 107:8079–8084, 2010.
- [10] M. E. Benser, N. P. Issa, and A. J. Hudspeth. Hair-bundle stiffness dominates the elastic reactance to otolithic-membrane shear. *Hear. Res.*, 68:243–252, 1993.
- [11] M. Beurg, R. Fettiplace, J.-H. Nam, and A. J. Ricci. Localization of inner hair cell mechanotransducer channels using high-speed calcium imaging. *Nat. Neurosci.*, 12:553–558, 2009.

- [12] D. Bozovic and A. J. Hudspeth. Hair-bundle movements elicited by transepithelial electrical stimulation of hair cells in the sacculus of the bullfrog. *Proc. Natl. Acad. Sci. USA*, 100:958–963, 2003.
- [13] G. Bredberg. Cellular pattern and nerve supply of the human organ of Corti. *Acta Oto-Laryngol.*, Suppl. 236:1–135, 1968.
- [14] M. C. Brown. Morphology of labeled afferent fibers in the guinea pig cochlea. *J. Comp. Neurol.*, 260:591–604.
- [15] W. E. Brownell. Observations on a motile response in isolated outer hair cells. In D. B. Webster and L. M. Aitkin, editors, *Neural Mechanisms of Hearing*. Monash U.P., Clayton, Australia, 1983.
- [16] W. E. Brownell, C. R. Bader, D. Bertrand, and Y. De Ribaupierre. Evoked mechanical responses of isolated cochlear outer hair cells. *Science*, 227:194–196, 1985.
- [17] S. Camalet, T. Duke, F. Jülicher, and J. Prost. Auditory sensitivity provided by self-tuned critical oscillations of hair cells. *Proc. Natl. Acad. Sci. USA*, 97:3183–3188, 2000.
- [18] H.-C. Chang, X. Cao, U. K. Mishra, and R. A. York. Phase noise in coupled oscillators: theory and experiment. *IEEE*, 45:604–615, 1997.
- [19] E. L. M. Cheung and D. P. Corey. Ca^{2+} changes the force sensitivity of the hair-cell transduction channel. *Biophys. J.*, 90:124–139, 2006.
- [20] D. Clausznitzer, B. Lindner, F. Jülicher, and P. Martin. Two-state approach to stochastic hair bundle dynamics. *Phys. Rev. E*, 77:041901, 2008.
- [21] J. R. Clay and R. L. DeHaan. Fluctuations in interbeat interval in rhythmic heart-cell clusters - Role of membrane voltage noise. *Biophys. J.*, 28:377–389, 1979.
- [22] N. P. Cooper, J. O. Pickles, and G. A. Manley. Traveling waves, second filters, and physiological vulnerability: A short history of the discovery of active processes in hearing. In G. A. Manley, R. R. Fay, and A. N. Popper, editors, *Active Processes and Otoacoustic Emissions*. Springer-Verlag, 2008.
- [23] D. P. Corey and A. J. Hudspeth. Kinetics of the receptor current in bullfrog saccular hair cells. *J. Neurosci.*, 3:962–976, 1983.
- [24] A. Corti. Recherches sur l’organe de l’ouïe des mammiferes. *Z. Wiss. Zool. Abt. A.*, 3:109–169, 1851.
- [25] S. A. Counter, E. Borg, and L. Lofqvist. Acoustic trauma in extracranial magnetic brain stimulation. *Electroen. Clin. Neuro.*, 78:173–184, 1991.

- [26] A. C. Crawford, M. G. Evans, and R. Fettiplace. The actions of calcium on the mechano-electrical transducer current of turtle hair cells. *J. Physiol.*, 434:369–398, 1991.
- [27] A. C. Crawford and R. Fettiplace. The mechanical properties of ciliary bundles of turtle cochlear hair cells. *J. Physiol.*, 364:359–379, 1985.
- [28] H. Daido. Quasi-entrainment and slow relaxation in a population of oscillators with random and frustrated interactions. *Phys. Rev. Lett.*, 68:1073–1076, 1992.
- [29] H. Daido. Onset of cooperative entrainment in limit-cycle oscillators with uniform all-to-all interactions: Bifurcation of the order function. *Physica D*, 91:24–66, 1996.
- [30] P. Dallos. Cochlear physiology. *Annu. Rev. Psychol.*, 32:153–190, 1981.
- [31] P. Dallos and B. N. Evans. High-frequency motility of outer hair cells and the cochlear amplifier. *Science*, 267:2006–2009, 1995.
- [32] H. Davis. An active process in cochlear mechanics. *Hear. Res.*, 9:79–90, 1983.
- [33] W. Denk, W. W. Webb, and A. J. Hudspeth. Mechanical properties of sensory hair bundles are reflected in their Brownian motion measured with a laser differential interferometer. *Proc. Natl. Acad. Sci. USA*, 86:5371–5375, 1989.
- [34] K. Dierkes, B. Lindner, and F. Jülicher. Enhancement of sensitivity by coupling of active hair bundles. *Proc. Natl. Acad. Sci. USA*, 105:18669–18674, 2008.
- [35] T. Duke and F. Jülicher. Active traveling wave in the cochlea. *Phys. Rev. Lett.*, 90(158101), 2003.
- [36] T. Duke and F. Jülicher. Critical oscillators as active elements in hearing. In G. A. Manley, R. R. Fay, and A. N. Popper, editors, *Active Processes and Otoacoustic Emissions*. Springer-Verlag, 2008.
- [37] R. A. Eatock, D. P. Corey, and A. J. Hudspeth. Adaptation of mechano-electrical transduction in hair cells of the bullfrog’s sacculus. *J. Neurosci.*, 7:2821–2836, 1987.
- [38] D. A. Eddins and D. M. S. Green. Temporal integration and temporal resolution. In B. C. J. Moore, editor, *Hearing*. Academic, San Diego, 1995.
- [39] V. M. Eguíluz, M. Ospeck, Y. Choe, A. J. Hudspeth, and M. O. Magnasco. Essential nonlinearities in hearing. *Phys. Rev. Lett.*, 84:5232–5235, 2000.
- [40] A. K. Engel, P. Fries, and W. Singer. Dynamic predictions: Oscillations and synchrony in top-down processing. *Nat. Rev. Neurosci.*, 2:704–716, 2001.

- [41] G. B. Ermentrout. Oscillator death in populations of “all to all” coupled nonlinear oscillators. *Physica D*, 41:219–231, 1990.
- [42] R. Fettiplace and P. A. Fuchs. Mechanisms of hair cell tuning. *Annu. Rev. Physiol.*, 61:809–834, 1999.
- [43] R. Fettiplace and C. M. Hackney. The sensory and motor roles of auditory hair cells. *Nat. Rev. Neurosci.*, 7:19–29, 2006.
- [44] R. Fettiplace and A. J. Ricci. Adaptation in auditory hair cells. *Curr. Opin. Neurobiol.*, 13:446–451, 2003.
- [45] M. Florentine, H. Fastl, and S. Buus. Temporal integration in normal hearing, cochlear impairment, and impairment simulated by masking. *J. Acoust. Soc.*, 84:195–203, 1988.
- [46] J. B. J. Fourier. *Théorie analytique de la chaleur*. Firmin Didot, Paris, 1822.
- [47] D. N. Furness, C. M. Hackney, and M. G. Evans. Localisation of the mechanotransducer channels in mammalian cochlear hair cells provides clues to their gating. *J. Physiol.*, 588:765–772, 2010.
- [48] R. Galambos and H. Davis. The response of single auditory-nerve fibers to acoustic stimulation. *J. Neurophysiol.*, 6:39–58, 1943.
- [49] C. W. Gardiner. *Handbook of Stochastic Methods*. Springer-Verlag, Berlin, 2004.
- [50] N. Gavara and R. S. Chadwick. Collagen-based mechanical anisotropy of the tectorial membrane: Implications for inter-row coupling of outer hair cell bundles. *PLoS One*, 4:e4877, 2009.
- [51] S. Gerschgorin. Über die Abgrenzung der Eigenwerte einer Matrix. *Izv. Akad. Nauk. USSR Otd. Fiz. Mat. Nauk.*, 7:749–754, 1931.
- [52] P. G. Gillespie and U. Müller. Mechanotransduction by hair cells: Models, molecules, and mechanisms. *Cell*, 139:33–44, 2009.
- [53] T. Gold. Hearing II. The physical basis of the action of the cochlea. *Proc. R. Soc. B.*, 135:492–498, 1948.
- [54] T. Gold and R. J. Pumphrey. Hearing I. The cochlea as a frequency analyzer. *Proc. R. Soc. B.*, 135:462–491, 1948.
- [55] M. C. Göpfert, A. D. L. Humphris, J. T. Albert, D. Robert, and O. Hendrich. Power gain exhibited by motile mechanosensory neurons in *Drosophila* ears. *Proc. Natl. Acad. Sci. USA*, 102:325–330, 2005.

- [56] D. M. Green, C. C. Wier, and F. L. Wightman. Gold and Pumphrey revisited, again. *J. Acoust. Soc. Am.*, 57:935–938, 1975.
- [57] D. D. Greenwood. A cochlear frequency-position function for several species – 29 years later. *J. Acoust. Soc. Am.*, 87:2592–2605, 1990.
- [58] R. Gueta, D. Barlam, R. Z. Shneck, and I. Rousso. Measurement of the mechanical properties of isolated tectorial membrane using atomic force microscopy. *Proc. Natl. Acad. Sci. USA*, 103:14790–14795, 2006.
- [59] N. Hacohen, J. A. Assad, W. J. Smith, and D. P. Corey. Regulation of tension on hair-cell transduction channels: Displacement and calcium dependence. *J. Neurosci.*, 9:3988–3997, 1989.
- [60] H. Haken, H. Sauermann, C. Schmid, and H. D. Vollmer. Theory of laser noise in phase locking region. *Z. Phys.*, 206:369–393, 1967.
- [61] L. Han and A. B. Neiman. Spontaneous oscillations, signal amplification, and synchronization in a model of active hair bundle mechanics. *Phys. Rev. E*, 81:041913, 2010.
- [62] J. R. Holt, D. P. Corey, and R. A. Eatock. Mechanoelectrical transduction and adaptation in hair cells of the mouse utricle, a low-frequency vestibular organ. *J. Neurosci.*, 17:8739–8748, 1997.
- [63] J. R. Holt, S. K. H. Gillespie, D. W. Provance Jr., K. Shah, K. M. Shokat, D. P. Corey, J. A. Mercer, and P. G. Gillespie. A chemical-genetic strategy implicates myosin-1c in adaptation by hair cells. *Cell*, 108(3):371 – 381, 2002.
- [64] K. Horikawa, K. Ishimatsu, E. Yoshimoto, S. Kondo, and H. Takeda. Noise-resistant and synchronized oscillation of the segmentation clock. *Nature*, 441:719–723, 2006.
- [65] J. Howard and A. J. Hudspeth. Mechanical relaxation of the hair bundle mediates adaptation in mechanoelectrical transduction by the bullfrog’s saccular hair cell. *Proc. Natl. Acad. Sci. USA*, 84:3064–3068, 1987.
- [66] J. Howard and A. J. Hudspeth. Compliance of the hair bundle associated with gating of mechanoelectrical transduction channels in the bullfrog’s saccular hair cell. *Neuron*, 1:189–199, 1988.
- [67] A. J. Hudspeth. Mechanoelectrical transduction by hair cells in the acousticolateralis sensory system. *Ann. Rev. Neurosci.*, 6:187–215, 1983.
- [68] A. J. Hudspeth. How the ear’s works work. *Nature*, 341:397–404, 1989.

- [69] A. J. Hudspeth. Hair-bundle mechanics and a model for mechano-electrical transduction by hair cells. In D. P. Corey and S. D. Roper, editors, *Sensory Transduction*. Rockefeller University Press, 1992.
- [70] A. J. Hudspeth. Making an effort to listen: mechanical amplification in the ear. *Neuron*, 59:530–545, 2008.
- [71] A. J. Hudspeth, Y. Choe, A. D. Mehta, and P. Martin. Putting ion channels to work: Mechano-electrical transduction, adaptation, and amplification by hair cells. *Proc. Natl. Acad. Sci. USA*, 97:11765–11772, 2000.
- [72] A. J. Hudspeth and D. P. Corey. Sensitivity, polarity, and conductance change in the response of vertebrate hair cells to controlled mechanical stimuli. *Proc. Natl. Acad. Sci. USA*, (74):2407–2411, 1977.
- [73] A. J. Hudspeth and P. G. Gillespie. Pulling springs to tune transduction: Adaptation by hair cells. *Neuron*, 12:1–9, 1994.
- [74] A. J. Hudspeth and R. S. Lewis. Kinetic analysis of voltage-dependent and ion-dependent conductances in saccular hair cells of the bullfrog, *Rana catesbeiana*. *J. Physiol., Lond.*, 400:237–274, 1988.
- [75] R. A. Jacobs and A. J. Hudspeth. Ultrastructural correlates of mechano-electrical transduction in hair cells of the bullfrog’s internal ear. *Cold Spring Harb. Symp. Quant. Biol.*, 55:547–561, 1990.
- [76] J. Jalife. Mutual entrainment and electrical coupling as mechanisms for synchronous firing of rabbit sino-atrial pacemaker cells. *J. Physiol.-London*, 356:221–243, 1984.
- [77] F. Jaramillo and A. J. Hudspeth. Displacement-clamp measurement of the forces exerted by gating springs in the hair bundle. *Proc. Natl. Acad. Sci. USA*, 90:1330–1334, 1993.
- [78] J. M. Jørgensen, Å. Flock, and J. Wersäll. The Lorenzinian ampullae of *Polyodon spathula*. *Z. Zellforsch.*, 130:362–377, 1972.
- [79] F. Jülicher, K. Dierkes, B. Lindner, J. Prost, and P. Martin. Spontaneous movements and linear response of a noisy oscillator. *Eur. Phys. J. E*, 29:449–460, 2009.
- [80] B. Kachar, M. Parakkal, and J. Fex. Structural basis for mechanical transduction in the frog vestibular sensory apparatus: I. The otolithic membrane. *Hear. Res.*, 45:179–190, 1990.
- [81] B. Kachar, M. Parakkal, M. Kurc, Y. Zhao, and P. G. Gillespie. High-resolution structure of hair-cell tip links. *Proc. Natl. Acad. Sci. USA*, 97:13336–13341, 2000.

- [82] P. Kazmierczak, H. Sakaguchi, J. Tokita, E. M. Wilson-Kubalek, R. A. Milligan, U. Müller, and B. Kachar. Cadherin 23 and protocadherin 15 interact to form tip-link filaments in sensory hair cells. *Nature*, (449):87–91, 2007.
- [83] D. T. Kemp. Stimulated acoustic emissions from within the human auditory system. *J. Acoust. Soc. Am.*, 64:1386–1391, 1978.
- [84] D. T. Kemp. Evidence of mechanical nonlinearity and frequency selective wave amplification in the cochlea. *Arch. Oto.-Rhino.-Laryn.*, 224:37–45, 1979.
- [85] D. T. Kemp and A. M. Brown. Ear canal acoustic and round window electrical correlates of $2f_1 - f_2$ distortion generated in the cochlea. *Hear. Res.*, 13:39–46, 1984.
- [86] H. J. Kennedy, A. C. Crawford, and R. Fettiplace. Force generation by mammalian hair bundles supports a role in cochlear amplification. *Nature*, 433:880–883, 2005.
- [87] A. V. Kondrachuk. Computer simulation of the mechanical stimulation of the saccular membrane of bullfrog. *Hear. Res.*, 143:130–138, 2000.
- [88] C. Köppl. Birds - same thing, but different? Convergent evolution in the avian and mammalian auditory systems provides informative comparative models. *Hear. Res.*, doi:10.1016/j.heares.2010.03.095, 2010.
- [89] C. Köppl and G. A. Manley. Spontaneous otoacoustic emissions in the bobtail lizard. II: Interactions with external tones. *Hear. Res.*, 73:159–170, 1994.
- [90] M. Kössl and I. J. Russell. Basilar membrane resonance in the cochlea of the mustached bat. *Proc. Natl. Acad. Sci. USA*, 92:276–279, 1995.
- [91] M. Kössl and M. Vater. The cochlear frequency map of the mustache bat, *Pteronotus parnellii*. *J. Comp. Physiol. A*, 157:687–697, 1985.
- [92] H. Koyama, E. R. Lewis, E. L. Leverenz, and R. A. Baird. Acute seismic sensitivity in the bullfrog ear. *Brain Res.*, 250:168–172, 1982.
- [93] A. S. Kozlov, T. Risler, and A. J. Hudspeth. Coherent motion of stereocilia assures the concerted gating of hair-cell transduction channels. *Nat. Neurosci.*, 10:87–92, 2007.
- [94] C. J. Kros, W. Marcotti, S. M. van Netten, T. J. Self, R. T. Libby, S. D. M. Brown, G. P. Richardson, and K. P. Steel. Reduced climbing and increased slipping adaptation in cochlear hair cells of mice with *Myo7a* mutations. *Nat. Neurosci.*, (5):41–47, 2002.
- [95] Y. Kuramoto. *Chemical Oscillations, Waves and Turbulence*. Springer, New York, 1984.

- [96] M. LeMasurier and P. G. Gillespie. Hair-cell mechanotransduction and cochlear amplification. *Neuron*, 48:403–415, 2005.
- [97] E. R. Lewis. Tuning in the bullfrog ear. *Biophys. J.*, 53:441–447, 1988.
- [98] E. R. Lewis and C. W. Li. Hair cell types and distributions in the otolithic and auditory organs of the bullfrog. *Brain Res.*, 83:35–50, 1975.
- [99] B. Lindner, K. Dierkes, and F. Jülicher. Local exponents of nonlinear compression in periodically driven noisy oscillators. *Phys. Rev. Lett.*, 103:250601, 2009.
- [100] F. Mammano and J. F. Ashmore. Reverse transduction measured in the isolated cochlea by laser Michelson interferometry. *Nature*, 365:838–841, 1993.
- [101] G. A. Manley. Evolution of structure and function of the hearing organ of lizards. *J. Neurobiol.*, 53:202–211, 2002.
- [102] G. A. Manley. The lizard basilar papilla and its evolution. In G. A. Manley, A. N. Popper, and R. R. Fay, editors, *Evolution of the vertebrate auditory system*. Springer-Verlag, 2004.
- [103] G. A. Manley, L. Gallo, and C. Köppl. Spontaneous otoacoustic emissions in two gecko species, *Gekko gecko* and *Eublepharis macularius*. *J. Acoust. Soc. Am.*, 99:1588–1603, 1996.
- [104] G. A. Manley, D. L. Kirk, C. Köppl, and G. K. Yates. *In vivo* evidence for a cochlear amplifier in the hair-cell bundle of lizards. *Proc. Natl. Acad. Sci. USA*, 98:2826–2831, 2001.
- [105] G. A. Manley and C. Köppl. Phylogenetic development of the cochlea and its innervation. *Curr. Opin. Neurobiol.*, 8:468–474, 1998.
- [106] G. A. Manley, A. N. Popper, and R. R. Fay. *Evolution of the Vertebrate Auditory System*. Springer, New York, 2004.
- [107] D. O Maoileidigh and F. Jülicher. The interplay between active hair bundle mechanics and electromotility in the cochlea. In N. P. Cooper and D. T. Kemp, editors, *Concepts and Challenges in the Biophysics of Hearing, Proceedings of the 10th International Workshop on the Mechanics of Hearing Keele University, Staffordshire, UK, 27 - 31 July 2008*. World Scientific Publishing, 2009.
- [108] V. S. Markin and A. J. Hudspeth. Gating-spring models of mechano-electrical transduction by hair cells of the interal ear. *Annu. Rev. Biophys. Biomol. Struct.*, 24:59–83, 1995.

- [109] R. E. Marquis and A. J. Hudspeth. Effects of extracellular Ca^{2+} on hair-bundle stiffness and gating-spring integrity in hair cells. *Proc. Natl. Acad. Sci. USA*, 94:11923–11928, 1997.
- [110] P. Martin. Active hair-bundle motility of the hair cells of vestibular and auditory organs. In G. A. Manley, R. R. Fay, and A. N. Popper, editors, *Active Processes and Otoacoustic Emissions*. Springer-Verlag, 2008.
- [111] P. Martin, D. Bozovic, Y. Choe, and A. J. Hudspeth. Spontaneous oscillations by hair bundles of the bullfrog’s sacculus. *J. Neurosci.*, 23:4533–4548, 2003.
- [112] P. Martin and A. J. Hudspeth. Active hair-bundle movements can amplify a hair cell’s response to oscillatory mechanical stimuli. *Proc. Natl. Acad. Sci. USA*, 96:14306–14311, 1999.
- [113] P. Martin and A. J. Hudspeth. Compressive nonlinearity in the hair bundle’s active response to mechanical stimulation. *Proc. Natl. Acad. Sci. USA*, 98:14386–14391, 2001.
- [114] P. Martin, A. J. Hudspeth, and F. Jülicher. Comparison of a hair bundle’s spontaneous oscillations with its response to mechanical stimulation reveals the underlying active process. *Proc. Natl. Acad. Sci. USA*, 98:14380–14385, 2001.
- [115] P. Martin, A. D. Mehta, and A. J. Hudspeth. Negative hair-bundle stiffness betrays a mechanism for mechanical amplification by the hair cell. *Proc. Natl. Acad. Sci. USA*, 97:12026–12031, 2000.
- [116] P. C. Matthews and S. H. Strogatz. Phase diagram for the collective behavior of limit-cycle oscillators. *Phys. Rev. Lett.*, 65:1701–1704, 1990.
- [117] U. Müller. Cadherins and mechanotransduction by hair cells. *Curr. Opin. Cell Biol.*, 20:557–566, 2008.
- [118] B. Nadrowski, P. Martin, and F. Jülicher. Active hair-bundle motility harnesses noise to operate near an optimum of mechanosensitivity. *Proc. Natl. Acad. Sci. USA*, 101:12195–12200, 2004.
- [119] S. S. Narayan, A. N. Temchin, A. Recio, and M. A. Ruggero. Frequency tuning of basilar membrane and auditory nerve fibers in the same cochlea. *Science*, 282:1882–1884, 1998.
- [120] G. D. Nayak, H. S. K. Ratnayaka, R. J. Goodyear, and G. P. Richardson. Development of the hair bundle and mechanotransduction. *Int. J. Dev. Biol.*, 51:597–608, 2007.

- [121] A. Neiman and D. F. Russell. Stochastic biperiodic oscillations in the electroreceptors of paddlefish. *Phys. Rev. Lett.*, 86:3443–3446, 2001.
- [122] D. Nicastro, C. Schwartz, J. Pierson, R. Gaudette, M. E. Porter, and J. R. McIntosh. The molecular architecture of axonemes revealed by cryoelectron tomography. *Science*, 313:944–948, 2006.
- [123] A. L. Nuttall and D. F. Dolan. Steady-state sinusoidal velocity responses of the basilar membrane in guinea pig. *J. Acoust. Soc. Am.*, 99:1556–1565, 1996.
- [124] I. Ozden, S. Venkataramani, M. A. Long, B. W. Connors, and A. V. Nurmikko. Strong coupling of nonlinear electronic and biological oscillators: Reaching the “amplitude death” regime. *Phys. Rev. Lett.*, 93:158102, 2004.
- [125] J. O. Pickles. *An Introduction to the Physiology of Hearing - 2nd Edition*. Academic Press, London, UK, 2003.
- [126] A. Pikovsky, M. Rosenblum, and J. Kurths. *Synchronization: A Universal Concept in Nonlinear Sciences*. Cambridge University Press, Cambridge, U.K., 2001.
- [127] R. Prakash and A. J. Ricci. Hair bundles teaming up to tune the mammalian cochlea. *Proc. Natl. Acad. Sci. USA*, 105:18651–18652, 2008.
- [128] R. Probst, B. L. Lonsbury-Martin, and G. K. Martin. A review of otoacoustic emissions. *J. Acoust. Soc. Am.*, 89:2027–2067, 1991.
- [129] R. D. Rabbitt, R. Boyle, and S. M. Highstein. Mechanical amplification by hair cells in the semicircular canals. *Proc. Natl. Acad. Sci. USA*, 107:3864–3869, 2010.
- [130] D. Ramunno-Johnson, C. E. Strimbu, A. Kao, L. Fredrickson Hemsinga, and D. Bozovic. Effects of the somatic ion channels upon spontaneous mechanical oscillations in hair bundles of the inner ear. *Hear. Res.*, doi:10.1016/j.heares.2010.05.017, 2010 (in press).
- [131] P. Reimann, C. van den Broeck, and R. Kawai. Nonequilibrium noise in coupled phase oscillators. *Phys. Rev. E*, 60:6402–6406, 1999.
- [132] A. J. Ricci, A. C. Crawford, and R. Fettiplace. Active hair bundle motion linked to fast transducer adaptation in auditory hair cells. *J. Neurosci.*, 20:7131–7142, 2000.
- [133] A. J. Ricci, A. C. Crawford, and R. Fettiplace. Tonotopic variation in the conductance of the hair cell mechanotransducer channel. *Neuron*, 40:983–990, 2003.

- [134] A. J. Ricci, H. J. Kennedy, A. C. Crawford, and R. Fettiplace. The transduction channel filter in auditory hair cells. *J. Neurosci.*, 25:7831–7839, 2005.
- [135] C.-P. Richter, G. Emadi, G. Getnick, A. Quesnel, and P. Dallos. Tectorial membrane stiffness gradients. *Biophys. J.*, 93:2265–2276, 2007.
- [136] T. Risler, J. Prost, and F. Jülicher. Universal critical behavior of noisy coupled oscillators. *Phys. Rev. Lett.*, 93:175702, 2004.
- [137] W. M. Roberts, J. Howard, and A. J. Hudspeth. Hair cells: Transduction, tuning, and transmission in the inner ear. *Annu. Rev. Cell Biol.*, 4:63–92, 1988.
- [138] L. Robles and M. A. Ruggero. Mechanics of the mammalian cochlea. *Physiol. Rev.*, 81:1305–1352, 2001.
- [139] L. Robles, M. A. Ruggero, and N. C. Rich. Basilar membrane mechanics at the base of the chinchilla cochlea. I. Input-output functions, tuning curves, and response phases. *J. Acoust. Soc. Am.*, 80:1364–1374, 1986.
- [140] M. A. Ruggero and N. C. Rich. Furosemide alters organ of Corti mechanics: Evidence for feedback of outer hair cells upon the basilar membrane. *J. Neurosci.*, 11:1057–1067, 1991.
- [141] M. A. Ruggero, N. C. Rich, A. Recio, S. S. Narayan, and L. Robles. Basilar-membrane responses to tones at the base of the chinchilla cochlea. *J. Acoust. Soc. Am.*, 101:2151–2163, 1997.
- [142] A. Rusch and U. Thurm. Spontaneous and electrically induced movements of ampullary kinocilia and stereovilli. *Hear. Res.*, 48:247–264, 1990.
- [143] M. A. Rutherford and W. M. Roberts. Spikes and membrane potential oscillations in hair cells generate periodic afferent activity in the frog sacculus. *J. Neurosci.*, 29:10025–10037, 2009.
- [144] H. Sakaguchi, S. Shinomoto, and Y. Kuramoto. Local and global self-entrainments in oscillator lattices. *Prog. Theor. Phys.*, 77:1005–1010, 1987.
- [145] P. M. Sellick, R. B. Patuzzi, and B. M. Johnstone. Measurement of basilar membrane motion in the guinea pig using the Mössbauer technique. *J. Acoust. Soc. Am.*, 72:131–141, 1982.
- [146] E. A. G. Shaw. The external ear. In W. D. Keidel and W. D. Neff, editors, *Handbook of Sensory Physiology*. Springer, Berlin, 1974.
- [147] B. Shoelson, E. K. Dimitriadis, H. Cai, B. Kachar, and R. S. Chadwick. Evidence and implications of inhomogeneity in tectorial membrane elasticity. *Biophys. J.*, 87:2768–2777, 2004.

- [148] S. L. Shotwell, R. Jacobs, and A. J. Hudspeth. Directional sensitivity of individual hair cells to controlled deflection of their hair bundles. *Ann. NY Acad. Sci.*, 374:1–10, 1981.
- [149] M. S. Smotherman and P. M. Narins. The electrical properties of auditory hair cells in the frog amphibian papilla. *J. Neurosci.*, 19:5275–5292, 1999.
- [150] M. Sotomayor and K. Schulten. The allosteric role of the Ca^{2+} switch in adhesion and elasticity of C-cadherin. *Biophys. J.*, 94:4621–4633, 2008.
- [151] H. Spoendlin. Innervation densities of the cochlea. *Acta Oto.-Laryngol.*, 73:239–254, 1972.
- [152] E. A. Stauffer, J. D. Scarborough, M. Hirono, E. D. Miller, K. Shah, J. A. Mercer, J. R. Holt, and P. G. Gillespie. Fast adaptation in vestibular hair cells requires myosin-1c activity. *Neuron*, 47:541–553, 2005.
- [153] R. L. Stratonovich. *Topics in the Theory of Random Noise II*. Gordon and Breach, New York, 1967.
- [154] D. Strelhoff and Å. Flock. Stiffness of sensory-cell hair bundles in the isolated guinea pig cochlea. *Hear. Res.*, 15:19–28, 1984.
- [155] C. E. Strimbu, D. Ramunno-Johnson, L. Fredrickson, K. Arisaka, and D. Bozovic. Correlated movements of hair bundles coupled to the otolithic membrane in the bullfrog sacculus. *Hear. Res.*, 256:58–63, 2009.
- [156] S. H. Strogatz. *Nonlinear Dynamics and Chaos*. Perseus Books, Cambridge, Massachusetts, 1994.
- [157] S. H. Strogatz. From Kuramoto to Crawford: Exploring the onset of synchronization in populations of coupled oscillators. *Physica D*, 143:1–20, 2000.
- [158] S. H. Strogatz and R. E. Mirollo. Stability of incoherence in a population of coupled oscillators. *J. Stat. Phys.*, 63:613–635, 1991.
- [159] S. H. Strogatz and I. Stewart. Coupled oscillators and biological synchronization. *Sci. Am.*, 269:102–109, 1993.
- [160] I. Tasaki. Nerve impulses in individual auditory nerve fibers of guinea pig. *J. Neurophysiol.*, 17:97–122, 1954.
- [161] G. Taschenberger and G. A. Manley. Spontaneous otoacoustic emissions in the barn owl. *Hear. Res.*, 110:61–76, 1997.
- [162] L. G. Tilney, D. J. Derosier, and M. J. Mulroy. The organization of actin filaments in the stereocilia of cochlear hair cells. *J. Cell. Biol.*, 86:244–259, 1980.

- [163] L. G. Tilney and J. C. Saunders. Actin filaments, stereocilia, and hair cells of the bird cochlea. I. Length, number, width, and distribution of stereocilia of each hair cell are related to the position of the hair cell on the cochlea. *J. Cell. Biol.*, 96:807–821, 1983.
- [164] L. Úhlelová, L. Voldřich, and R. Janisch. Correlative study on sensory cell density and cochlear length in humans. *Hear. Res.*, 28:149–151, 1987.
- [165] P. van Dijk, H. P. Wit, and J. M. Segenhout. Spontaneous otoacoustic emissions in the European edible frog (*Rana Esculenta*): Spectral details and temperature-dependence. *Hear. Res.*, 42:273–282, 1989.
- [166] A. Vilfan and T. Duke. Frequency clustering in spontaneous otoacoustic emissions from a lizard’s ear. *Biophys. J.*, 95:4622–4630, 2008.
- [167] G. von Békésy. Zur Theorie des Hörens; die Schwingungsform der Basilarmembran. *Physik. Zeits.*, 29:793–810, 1928.
- [168] G. von Békésy. Über die Schwingungen der Schneckentrennwand beim Präparat und Ohrenmodell. *Akust. Zeits.*, 7:173–186, 1943.
- [169] G. von Békésy. Über die Resonanzkurve und die Abklingzeit der verschiedenen Stellen der Schneckentrennwand. *Akust. Zeits.*, 8:66–76, 1947.
- [170] G. von Békésy. Experiments in hearing. E. G. Wever, editor. McGraw-Hill, New York, 1960.
- [171] G. von Békésy. Concerning the pleasures of observing, and the mechanics of the inner ear. Nobel lectures, Physiology or Medicine 1942-1962. Elsevier, Amsterdam, 1961.
- [172] H. von Helmholtz. Die Lehre von den Tonempfindungen als physiologische Grundlage für die Theorie der Musik. Vieweg, Braunschweig, 1863.
- [173] W. B. Warr. The olivocochlear bundle: its origins and terminations in the cat. In R. F. Naunton and C. Fernandez, editors, *Evoked Electrical Activity in the Auditory Nervous System*. Academic Press, New York and London, 1978.
- [174] K. Wiesenfeld, P. Colet, and S. H. Strogatz. Synchronization transitions in a disordered Josephson series array. *Phys. Rev. Lett.*, 76:404–407, 1996.
- [175] S. Wiggins. *Introduction to Applied Nonlinear Dynamical Systems and Chaos*. Springer-Verlag, New-York, 2nd edition, 2003.
- [176] A. T. Winfree. Biological rhythms and the behavior of populations of coupled oscillators. *J. Theor. Biol.*, 16:15–42, 1967.

-
- [177] Y.-C. Wu, A. J. Ricci, and R. Fettiplace. Two components of transducer adaptation in auditory hair cells. *J. Neurophysiol.*, 82:2171–2181, 1999.
- [178] M. A. Zaks, A. B. Neiman, S. Feistel, and L. Schimansky-Geier. Noise-controlled oscillations and their bifurcations in coupled phase oscillators. *Phys. Rev. E*, 66:066206, 2003.
- [179] J. Zheng, W. Shen, D. Z. Z. He, K. B. Long, L. D. Madison, and P. Dallos. Prestin is the motor protein of cochlear outer hair cells. *Nature*, 405:149–155, 2000.
- [180] J. J. Zwislocki. Theorie der Schneckenmechanik. *Acta Oto.-Laryngol. Suppl.*, 72:1–76, 1948.
- [181] J. J. Zwislocki and L. K. Cefaratti. Tectorial membrane ii: Stiffness measurements *in vivo*. *Hear. Res.*, 42:211–228, 1989.

Versicherung

Hiermit versichere ich, dass ich die vorliegende Arbeit ohne unzulässige Hilfe Dritter und ohne Benutzung anderer als der angegebenen Hilfsmittel angefertigt habe; die aus fremden Quellen direkt oder indirekt übernommenen Gedanken sind als solche kenntlich gemacht. Die Arbeit wurde bisher weder im Inland noch im Ausland in gleicher oder ähnlicher Form einer anderen Prüfungsbehörde vorgelegt.

Die Arbeit wurde am Max-Planck-Institut für Physik komplexer Systeme in der Abteilung “Biologische Physik” angefertigt und von Prof. Dr. Frank Jülicher betreut.

Ich erkenne die Promotionsordnung der Fakultät Mathematik und Naturwissenschaften der Technischen Universität Dresden vom 20. März 2000, sowie deren Änderungen vom 16.04.2003 und 17.07.2008, an.

Kai Dierkes